Development of the Fast Light Alloy Stamping Technology (FAST) towards Automotive Applications: Experimental Studies

By

Kang Ji

Department of Mechanical Engineering

South Kensington Campus

Imperial College London

London SW7 2AZ

U.K.

A thesis submitted for the degree of Doctor of Philosophy of

Imperial College London

2017

Declaration of originality

This thesis hereby presented is based on research by the author at the Department of Mechanical Engineering of Imperial College London. I declare the work contained in this thesis is only author's own work. Not any part of the present work has been submitted for any other degree or qualification elsewhere.

Kang Ji

November 2017

Copyright declaration

Confidentiality

The research work presented in this thesis was carried out under the NDA with an industrial partner. Copy, distribution or transmission of the thesis is only permitted with authorization from the author.

Acknowledgements

I would like to express my greatest thanks to my supervisors, Dr. Liliang Wang and Prof. Jianguo Lin, for their guidance and support throughout the project, and for offering me invaluable advices constantly. Their passions and trust encouraged me to explore not only new technologies but also a new life.

I would also like to thank to many people helped me on my research during my PhD project, especially to Omer, Jun, Haoxiang, Nicholas and Xiaochuan for their great help on experiments, simulations, and writing skills in these 4 years. It is also a pleasure to thank to Qunli, Xi, Zhaoheng, Ailing and Yong for cooperating on experiments and sharing useful information. I would thank to the technicians who gave me a great help for setting up the experiment and manufacturing specimen, to Suresh, Alex, Amit, Tony and Paul. Without all their help, I would not have achieved such results.

Everyone in MOM division is warm, and always ready to help. Thanks for all your friendly cooperation and accompany all along the 4 years life in Imperial College, to Kehuan, Wei, Yi, Kailun, Long, Jiaying, Ran, Yiran, Yang, Yuhao, Yizhuo, Yee, Qian, Nan, Denis, Muneeb, Farnaz, Tasnuva, Junyi, Jinghua, Qi, Jinghua and many more.

Finally, the biggest thank you undoubtedly goes to my parents. Thanks for always supporting my decision, encouraging me to explore a new life on the other end of the earth, and offering advices when I was seeking for help.

Kang Ji
London, UK
November 2017

Abstract

In order to improve fuel efficiency and reduce carbon emissions for the automotive industry, a novel forming technology Fast light alloy stamping technology (FAST) for high and ultra-high strength aluminium alloy thin wall components (such as AA7075) was developed with experimental studies in this thesis. The process consists of: rapid heating, forming and in-die quenching, and incubation. A hot Stamping Simulator tool set to study FAST was successfully developed and manufactured to work in conjunction with the Gleeble 3800 thermo-mechanical testing machine. Based on this Hot Stamping Simulator, the effect of forming parameters on the formability of material and post-form strength have been studied for AA7075 2 mm blank. The effects of contact pressure, lubricant, and tool material on the Interfacial heat transfer coefficient (IHTC) have also been studied, and a mathematical model was developed in order to calculate the quenching time, predict post form strength and optimise the tool design to secure a high quenching rate, enabling the full post-form strength to be retained. Verification tests for the FAST process utilising AA7075 2 mm blank were conducted by forming U-shape and M-shape components. A standard testing procedure was developed for different materials and manufacturer requirements and was verified by studying 6 test cases. Finally, as a new forming process, conclusions and recommendations are made outlining additional factors to be studied to enable the FAST process to be adopted in an industrial environment.

Nomenclature

English Alphabet

f	Volume fraction
f_{121}	Equilibrium volume fraction at 121°C
f_{177}	Equilibrium volume fraction at 177°C
h	Heat transfer coefficient
h_g	Heat transfer across the solid contact of real contact area
h_c	Heat transfer across air gap
k	Mean thermal conductivity of two contact bodies
p	Contact pressure between two contact surfaces
K	Model constant
C	Model constant
A	Fractional contact area
h_f	Applied lubricant thickness
k_f	Thermal conductivity of lubricant
k_t	Thermal conductivity of tool
k_w	Thermal conductivity of workpiece
Q	Thermal energy
I	Electrical current flow
r	Electrical resistance
t	Time
V	Electrical resistivity
L	Length
a	Cross sectional area
h_l	Heat transfer caused by lubricant between two solid surfaces
K_{st}	Harmonic mean thermal conductivity of the contact solids
R	Root mean square of surface roughness of the contact solids surfaces
N_P	Pressure dependent parameter
K_s	Harmonic mean of the average values of specimen
K_t	Harmonic mean of the average values of tools
R_s	Average roughness of specimen
R_t	Average roughness of tools

K_{stl}	Harmonic mean thermal conductivity of all the materials involved in the heat transfer including tools, specimen and lubricant
N_L	Lubricant layer thickness dependent parameter

Greek Alphabet

θ	Mean of the absolute slope of the surface profile
σ	Standard deviation of the profile heights
$\bar{\lambda}$	Mean thermal conductivity of the two contact bodies
σ_U	Ultimate tensile strength of the test specimens
ρ	Electrical resistivity
α	Model constant
λ	Model constant
β	Model constant
γ	Model constant
δ	Applied lubricant layer thickness

Abbreviations

FAST	Fast light alloy stamping technology
SHT	Solution heat treatment
HFQ	Solution heat treatment, Forming and in-die Quenching
DSC	Differential Scanning Calorimetry
CCT	Continuous Cooling Transformation
TTT	Time Temperature Transformation
SSSS	Supersaturated solid solution
GP	Guinier–Preston
IHTC	Interfacial heat transfer coefficient
Temp.	Temperature
UTS	Ultimate tensile strength
FE	Finite element
r.m.s.	Root mean square
RT	Room temperature
Min	Minimum
Max	Maximum
No.	Number

Contents

List of Figures

Chapter 1: Introduction

Chapter 2: Literature Review

Chapter 3: Hot Stamping Process Simulator

Chapter 4: Interfacial Heat Transfer Coefficient

Chapter 5: Development of Fast Light Alloy Stamping Technology

Chapter 6: Standard Test Procedures

List of Tables

List of publications

Journal articles:

Ji K., El Fakir O. E., Gao H., Wang L. (2015). Determination of Heat Transfer Coefficient for Hot Stamping Process. *Materials Today: Proceedings,* 2**,** S434-S439. https://dx.doi.org/10.1016/j.matpr.2015.05.059.

Ji K., Liu X., EL Fakir O., Liu J., Zhang Q., Wang L. (2016). Determination of the Interfacial Heat Transfer Coefficient in the Hot Stamping of AA7075. *Manufacturing Rev.,* 3**,** 16. https://doi.org/10.1051/mfreview/2016017.

Zhang Q., **Ji K.**, El Fakir O., Liu X., Wang L. (2016). Determination of Processing Windows for the Hot Stamping of AA7075. *Key Engineering Materials,* 716**,** 402-412. https://doi:10.4028/www.scientific.net/KEM.716.402.

Liu X., **Ji K.**, El Fakir O. E., Fang H., Gharbi M. M., Wang L. (2017). Determination of the interfacial heat transfer coefficient for a hot aluminium stamping process. *Journal of Materials Processing Technology,* 247**,** 158-170. https://doi.org/10.1016/j.jmatprotec.2017.04.005.

Patent:

Wang L., Sun Y., **Ji K.**, Luan X., El Fakir O., Cai Z., Liu X.; A method of forming parts from sheet metal; Patent application number: 1713741.5.

Conference papers:

Liu X., **Ji K.**, El Fakir O. E., Liu J., Zhang Q., Wang L. (2015). Determination of the interfacial heat transfer coefficient in the hot stamping of AA7075. *MATEC Web of Conferences,* 21**,** 05003. https://doi.org/10.1051/matecconf/20152105003.

Luan X., Liu X., Fang H., **Ji K.**, Efkafir O., Wang L. (2016). Characterization of the interfacial heat transfer coefficient for hot stamping processes. *Journal of Physics Conference Series*. 734, 032079. https:// doi: 10.1088/1742-6596/734/3/032079.

Gao H., Denis J.P., Luan X, **Ji K**., Zhang Q., Zheng Y., Mohammad G., Wang L. (2017). Forming limit prediction AA7075 alloys under hot stamping conditions. *IDDRG2017 - 36th IDDRG conference Materials Modelling and testing for sheet metal forming*, Munich, Germany, July 2017.

Conference paper accepted for publication:

Zhang Q., Liu J., Luan X., **Ji K**., Wang L. (2018). Constitutive modelling of precipitation hardening responses of a high strength 6xxx series aluminium alloy to fast warm stamping and artificial ageing. *Thermec2018 - International Conference on Processing & Manufacturing of Advanced Materials Processing, Fabrication, Properties, Applications.* Paris, France, July 2018.

Under Preparation:

Ji K., Cai Z., Elfakir O., Wang L. (2018). Effect of ultra-fast heating on existing precipitates and age hardening behaviour of naturally aged Al-Zn-Mg-Cu alloys.

Chapter 1
Introduction

Climate change, the increasing cost of conventional energy sources, as well as a growing population pose significant threats to economic and political stability (Jacobson, 2008). A sector which is responsible for a significant portion of global fossil fuel consumption (44.7% of total fossil fuels consumed in the EU (The European Union, 2016a)) is the transportation sector. This means that targeting the transportation sector is key to substantially reduce greenhouse gas emissions and improve energy security (The European Union, 2015, The European Union, 2016c). In the UK, 23% of total greenhouse gas emissions resulted from the transportation sector (including road vehicles), transportation of fuel for vehicles and upstream vehicle production in 2012 (The United Kingdom, 2014). Similarly, in the EU, greenhouse gas emissions from the transportation sector were 19% in 2012, increasing to 20.1% in 2014 (The European Union, 2016b).

To combat this issue, governments around the world have issued legislation requiring automotive producers to improve fuel efficiency and lower CO_2 emissions(The United Kingdom, 2008, The European Union, 2014). In the EU, the legal requirement for automakers by the year 2020 is to achieve an average CO_2 emissions of 95 g/km for passenger vehicles, or 45% lower than the standard in the year 2007. Carmakers failing to meet these targets face significant penalties (The European Union, 2014, The European Union, 2015).

In order to achieve such ambitious targets, carmakers are utilising a number of technologies, which can be broadly categorised into: (i) improving fuel efficiency and emissions of current engine technologies, (ii) low emission fuel sources and engine concepts (e.g. electric propulsion), and (iii) efficient vehicle dynamics, such as vehicular weight reduction(Jacobson, 2008, LUTSEY, 2010). According to many vehicle mass reduction studies and automotive manufacturers' reports (LUTSEY, 2010, The Aluminum Association, 2015a, Jacobson, 2008), light-weighting is the most effective approach to improving fuel-efficiency, without compromising (and in fact improving) other vehicle performance parameters such as acceleration and capacity. Additionally, the improved performance from vehicle light-weighting can alternatively be directed to secondary benefits. For instance, the power requirement for acceleration and braking is reduced due to lower vehicle mass, giving potential in further mass reduction by employing smaller engines (which consume less fuel due to lower internal resistances), transmissions and braking systems(A Ungureanu et al., 2007, Mordike and Ebert, 2001). As seen from Figure 1.1, it is suggested that a 10% weight reduction results in an improvement of 6%-8% fuel efficiency and reduction of CO_2 emission in return (LUTSEY, 2010), while a reduction of approximately 12.5 g CO_2 emission per km driven of a vehicle can be achieved from every 100 kg reduction of vehicle weight (A Ungureanu et al., 2007). As a result of these benefits, almost all large automotive manufacturers, such as Nissan, Jaguar and Land Rover, Fiat, and Ford, have begun efforts into vehicle mass reduction in recent years (LUTSEY, 2010).

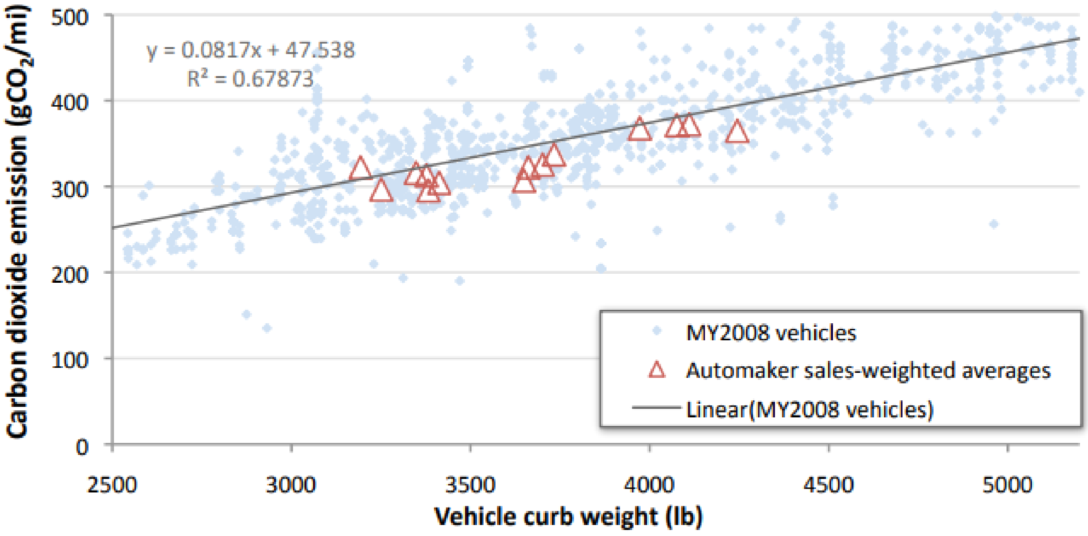

Figure 1.1 *U.S. automobile weight and CO_2 emissions(LUTSEY, 2010).*

Steels are widely used in automotive production, being implemented in most components in Body-in-White, Powertrain, Chassis and Closures. In 2007, approximately 75% of the weight of an average vehicle was from different types of steels, including low-carbon steel, medium strength steel and high strength steel (I. Taub et al., 2007). Therefore, reducing the weight of steel components provides a great potential to reduce the total mass of vehicles. Application of light-weight forming technologies and implementation of light-weight materials instead of steels are two of the most accepted methods to achieve vehicle light-weighting (LUTSEY, 2010, A Ungureanu et al., 2007, Karbasian and Tekkaya, 2010).

Light-weight forming technologies for steels aim at improving the strength of formed components, allowing the reduction of mass while providing the same stiffness(Hall and Fekete, 2017). Warm and hot stamping technologies are two promising light-weight forming technologies for thin-walled steel components applied in automotive manufacturing processes for mass production due to their high production rates, high post-form strengths and medium to high formability. In the hot stamping process, steel sheets are first heated to a high temperature, and are soaked at that temperature for a period of time to generate austenite. They are then transferred into a cold die set, and pressed and held in the dies. If the die closing force is sufficient, the sheets are formed and quenched at the same time, forming a martensitic phase which maximises the strength of the formed components. Alternatively, to reduce press machine time (or when the die pressure is insufficient for a critical quenching rate), formed components could be taken out from the dies and rapidly quenched by cooling liquid (Billur, 2017, De Moor and Speer, 2017, Karbasian and Tekkaya, 2010).

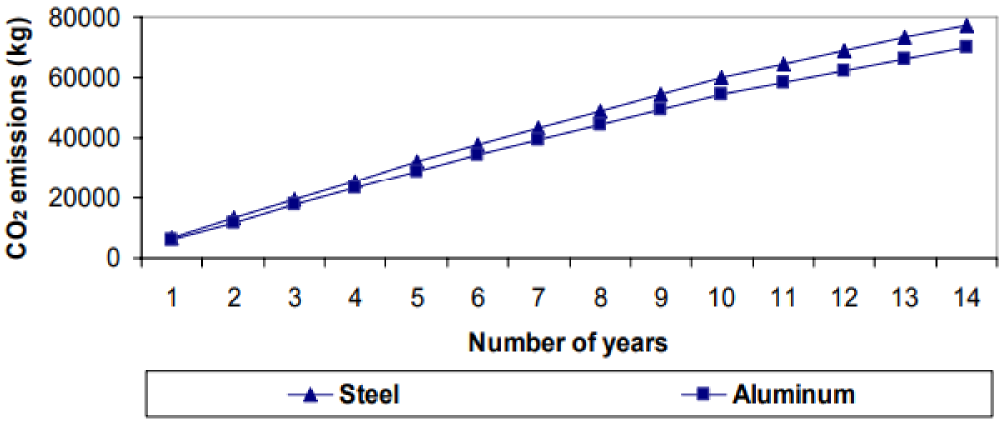

Figure 1.2 Carbon dioxide emissions over the lifetime of vehicle(A Ungureanu et al., 2007).

A significant number of academic and industrial studies have focused on light-weight materials such as carbon fibre, magnesium alloys and aluminium alloys that could provide the desired strength and stiffness to replace steels (A Ungureanu et al., 2007, Cole and Sherman, 1995). Of the existing engineering materials used in the automotive industry, aluminium alloys have been the most widely used replacement for steels due to their high strength-to-weight ratio and cost efficiency (The Aluminum Association, n.d., Lotus Engineering Inc., 2010). It has been found that careful design and use of 1 kg aluminium alloy can replace 2 kg of existing steel components providing the same stiffness, which gives an average reduction of 10 kg CO_2 emission during the vehicle lifetime (LUTSEY, 2010), and the comparison of life time CO_2 emissions for steel and aluminium body-in-white is shown in Figure 1.2 (A Ungureanu et al., 2007). There has been a continually increasing trend of aluminium alloy application in vehicles since the year 2000 with manufacturers such as Ford, Jaguar and Land Rover and BMW announcing an increase in aluminium alloy use for engines and body-in-white structures (Ward's Automotive, 2009, Lotus Engineering Inc., 2010), and there is an example for Lotus mass design trend shown in Figure 1.3.

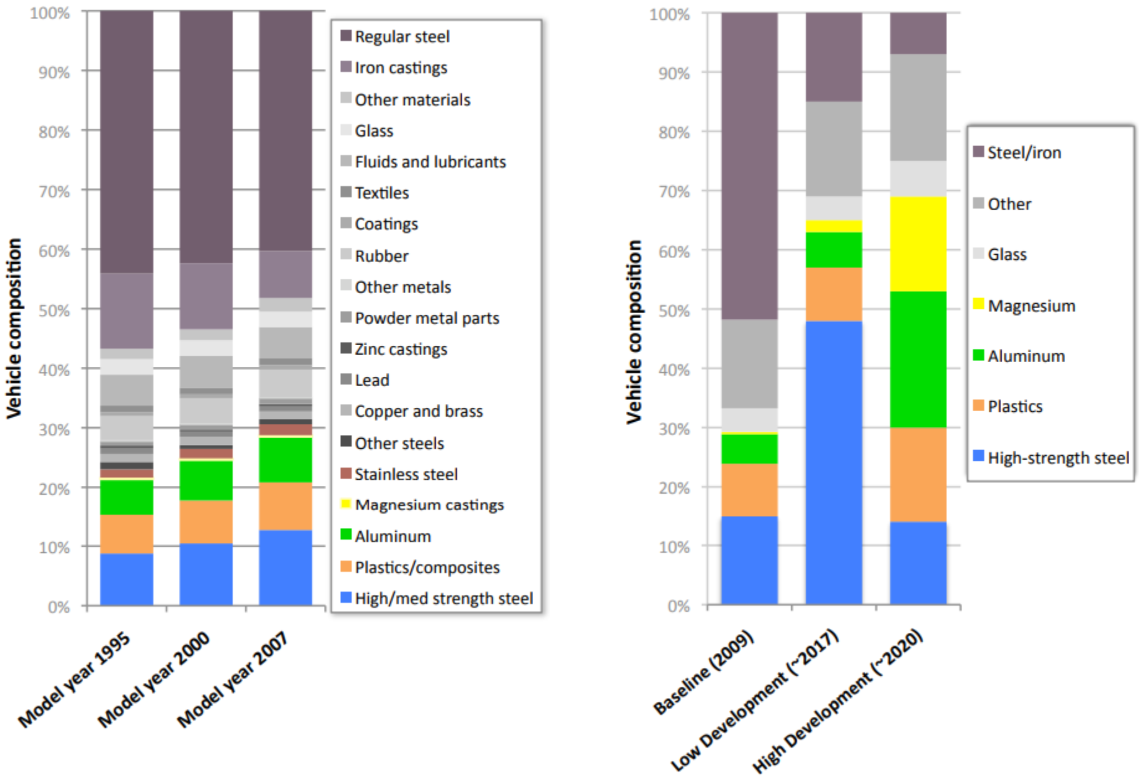

(a) (b)

Figure 1.3 Comparison of Lotus mass-reduced designs to historical vehicle composition trend: (a) Historical trend, 1995-2007 (Ward's Automotive, 2009); (b) Mass-reduced vehicle design(Lotus Engineering Inc., 2010). (LUTSEY, 2010)

There are two main types of aluminium alloys used in the automotive industry: cast alloys and wrought alloys (Starke and Staley, 1996, Cole and Sherman, 1995, The Aluminum Association, n.d.). These are produced via different processes, and are identified with different nomenclature systems. Cast aluminium alloys are mainly used in engines and gears, while wrought alloys are mainly used as sheets metal to form thin-walled components such as panels and pillars. This study focuses on forming of wrought aluminium alloys, in particular AA7075. Wrought alloys are denominated with 4 digit numbers indicating their alloy elements following The International Alloy Designation System. Classified by their alloy elements, there are 7 main series of wrought aluminium alloys, named from 1xxx series to 7xxx series. 5xxx, 6xxx, and 7xxx series alloys are the most ideal candidates for automakers to replace steels due to their light weight and high corrosion resistance. 7xxx series ultra-high strength Al-Zn-Mg alloys have the highest strength in wrought aluminium alloys, which could achieve 550 MPa yield strength or greater, and as a result are widely used in automotive and aerospace industries (The Aluminum Association, 2015b, The Aluminum Association, 2015a).

These alloys are also separated into two groups, heat treatable alloys including 2000 series, 6000 series and 7000 series aluminium alloys, and non-heat treatable alloys including all other series, such as the 4xxx series and 5xxx series aluminium alloys (The Aluminum Association, 2015a). Heat treatable alloys can be precipitation hardened, with the precipitation methods for each alloy being different. This study focuses on AA7075, an Al-Zn-Mg-Cu alloy, which is one of the ultra-high strength aluminium alloys in the 7xxx series of heat treatable alloys. The chemical composition of AA7075 according to The Aluminium Association standard is shown in Table 1.1 (The Aluminum Association, 2015b, The Aluminum Association, 2015a). The precipitation types and hardening principles of AA7075 are reviewed in Chapter 2. The AA7075-T6 2 mm blanks tested during the development of the Fast light alloy stamping technology process in this study (Chapter 5) were supplied by Kaiser Aluminium, and its chemical composition is listed in Table 1.2. The composition of the blanks supplied by a vehicle manufacturer and tested with a secondary aluminium alloy grade to verify the standardised test procedure (Chapter 6) was not disclosed. The blanks were heat treated into T4 temper prior to tests in most tests as the materials of the blanks in current FAST tests were T4 temper.

Table 1.1 *The composition range standard by The Aluminium Association (The Aluminum Association, 2015b).*

7075	**SI**	**FE**	**CU**	**MN**	**MG**	**CR**	**ZN**	**TI**	**V**	**ZR**	**OTHER**	**MAX**
MIN(wt%)	0.00	0.00	1.2	0.00	2.1	0.18	5.1	0.00	0.00	0.00	EACH	0.05
MAX(wt%)	0.40	0.50	2.0	0.30	2.9	0.28	6.1	0.20	0.05	0.05	TOT	0.15

Table 1.2 *The composition of AA7075-T6 2 mm blanks supplied by Kaiser Aluminium.*

Chemistry	**SI**	**FE**	**CU**	**MN**	**MG**	**CR**	**ZN**	**TI**	**V**	**ZR**		**OTHER**
Actual(wt%)	0.07	0.18	1.4	0.03	2.4	0.19	5.6	0.03	0.01	0.01	TOT	0.05

One of the most significant barriers to large-scale manufacture of medium and high strength aluminium alloy components is poor formability at room temperature(Ismail and Mohamed, 2016). As a result, considerable effort has been made in the development of new aluminium alloys with higher formability (Ismail and Mohamed, 2016, Lotus Engineering Inc., 2010), as well as advanced forming technologies to achieve higher formability while maintaining high strength (LUTSEY, 2010).

Of the existing forming technologies for sheet aluminium alloys, superplastic forming, warm forming, and hot stamping can be used to form complex shaped aluminium components (Cole and Sherman, 1995, Starke and Staley, 1996, Wang et al., 2011). Superplastic forming is an advanced forming technology for components requiring high accuracy, taking hours to form a single component, and thus is not suitable for mass production (Barnes, 2007). Warm forming and hot stamping are suitable for mass production due to the high speed of the processes. However, a trade off exists between warm forming and hot forming. Hot formed components tend to have higher strength and shape-complexity but lower production rate, whereas warm formed components have a comparatively higher production rate but lower strength and shape-complexity (Ismail and Mohamed, 2016).

Fast light alloy stamping technology (FAST) Process

Fast light alloy stamping technology (FAST), a new mass production forming technology to form sheet aluminium alloys, has been developed in this research. Distinct from both hot stamping and warm stamping processes, the FAST process comprises of 3 stages: (i) rapid heating to forming temperature which is normally lower than its Solution Heat Treatment (SHT) temperature, (ii) stamping and in-die quenching, and (iii) incubation.

The blank is first heated at a very high heating rate to a temperature lower than its Solution Heat Treatment (SHT) temperature, before being rapidly transferred to the press machine. The press machine with a cold toolset is subsequently closed at high speed to form the blank, and hold the formed component to quench the hot component between the cold dies. Once the component is quenched to its incubation temperature, the dies are opened and the component is transferred into a heat insulating chamber for incubation. The incubation temperature and time varies depending on different raw materials and manufacturer requirements, and might not be necessary for some materials. After completion of the process, the component is ready for storage and secondary fabrication, as well as paint bake cycles following assembly. There are numerous advantages of the FAST process over traditional hot/warm forming: (i) the potential to form complex-shaped components, (ii) comparably high production rate, (iii) high post-form strength, (iv) low natural ageing effect, (v) secondary fabrication availability and (vi) customised forming parameters. The micro-structural changes that occur in the material during this process is discussed further in Chapter 5. The FSAT process was verified in forming lab-scale components using M-shape forming tools and U-shape forming in UNI-Form novel automatic pilot hot stamping production line as discussed in Section 5.6.

In order to ensure the quenching rate is higher than its critical value, the interfacial heat transfer coefficient (IHTC) between blank and tool surfaces was studied in this research. The new forming technology parameters were studied using newly designed test equipment, named a 'hot stamping simulator', and was verified by forming trials using an automated production line. A standardised test procedure for testing a materials' suitability for FAST was designed and verified using a second batch of AA7075 2 mm blank material supplied by an automotive manufacturer.

Aims and objectives

The aims and objectives of this research project are listed as follows:

(1) A review and analysis of high strength aluminium alloys, along with the corresponding post-form heat treatments (including paint-bake cycles). Specifically, a focus on (i) precipitate nucleation and growth mechanisms at different temperature range; and (ii) precipitate nucleation and growth for AA7xxx alloys.

(2) The design and manufacture of a representative lab testing rig: the hot stamping simulator. Trials using the hot stamping simulator are to investigate the heat transfer between the blank and tool, and to simulate thermal-mechanical evolutions during the forming process.

(3) Perform heat transfer tests and develop interfacial heat transfer coefficient (IHTC) model. Conduct IHTC tests using the hot stamping simulator to study the effects of tool

material, contact pressure and lubricating condition on the IHTC value. Develop a model to predict it based on the given parameters.

(4) The development of the FAST process, with the objectives of: high production rate, high post form strength, high complexity and low cost. This mainly includes the experimental studies for effects of all forming parameters.

(5) The development of a standard material testing procedure, in order to minimise the test workload for identifying the best forming parameters whilst meeting industrial requirements.

Outline of Thesis

In this thesis, Chapter 2 presents a literature review of precipitation hardening theories and manufacturing technologies for thin-wall shaped aluminium components. Interfacial heat transfer coefficient (IHTC) tests and results were also reviewed.

Chapter 3 presents the novel test rig (hot stamping simulator) designed to simulate the complex thermo-mechanical process of hot stamping, which was utilised to conduct IHTC tests in Chapter 4.

In chapter 4, IHTC values were evaluated between AA7075 blank and tool materials under a range of contact pressure and lubrication conditions. Moreover, an IHTC model was developed to predict the IHTC evolution which was verified via forming tests.

Chapter 5 presents the test results and forming parameters leading to the development of the FAST process. Verification tests were conducted using M-shape and U-shape forming tools.

A standard test procedure to determine the optimal forming parameters for different materials and manufacturer constraints for FAST is presented in chapter 6. Six cases were studied with the forming parameters customised for each case.

Finally, conclusions of the present research are discussed in chapter 7, including the challenges encountered during the course of this research as well as advice for future studies on the FAST process.

Chapter 2

Literature review

2.1 Forming technologies for thin-wall components

2.1.1 Cold forming

Machining

Machining, as a traditional technology, has been used in many industrial applications for aluminium alloys. Components are machined from aluminium alloy blocks by removing all the unnecessary material. Machining is used to produce highly complex-shaped components, and typically does not require heat treatment to complete a component. However, the main disadvantage of machining is the low production rate and high level of waste, which can amount to as high as 95% of the original material (Santos et al., 2016).

Cold stamping

Cold stamping is typically used in conjunction with T4 and T6 aluminium alloy sheets, where stamping occurs between a set of dies at room temperature. T4 temper material exhibits higher ductility than T6 temper, although it requires artificial ageing after forming for age-hardening materials such as AA6xxx and AA7xxx series aluminium alloys (Hatch, 1984). Although exhibiting a high production rate and requiring simple production equipment, there are two main drawbacks: high spring back and poor formability with normally less than 0.2 true strain at failure (Ismail and Mohamed, 2016).

2.1.2 Warm stamping

Warm stamping uses a similar tooling to cold stamping and has been widely studied in recent years, especially in the automotive industry. Aluminium alloy blanks are typically heated to 200-300°C, and transferred to stamping machine to be placed between either warm or cold forming tools. Solution heat treatment, rapid quenching and artificial ageing processes are performed after the stamping. Warm stamping could be used to form more complex components compared to cold stamping since aluminium alloys exhibit better formability at this temperature range compared to room temperature. However, the ductility at these temperatures is normally in the range of 0.2-0.4 strain, which is not sufficient to form highly complex-shaped components. An additional drawback of warm stamping is that subsequent heat treatments take a long time and reduce the dimensional accuracy of the formed component (Ismail and Mohamed, 2016).

2.1.3 Solution heat treatment, Forming and in-die Quenching

The Solution heat treatment, Forming and in-die Quenching (HFQ®[1]) process is a recently developed advanced forming process combining both forming and quenching in one operation (Fakir et al., 2014). As shown in Figure 2.1, the blank is firstly heated to its SHT temperature and soaked at that temperature until it is fully solution heat treated. The hot blank is then transferred to the press machine to be simultaneously formed and rapidly quenched by cold dies. The blank is held in the cold dies until it is fully quenched to room temperature, after which supersaturated solid solution (SSSS) condition is retained. Artificial ageing is performed after quenching to maintain the full post-form strength (Lin et al., 2009).

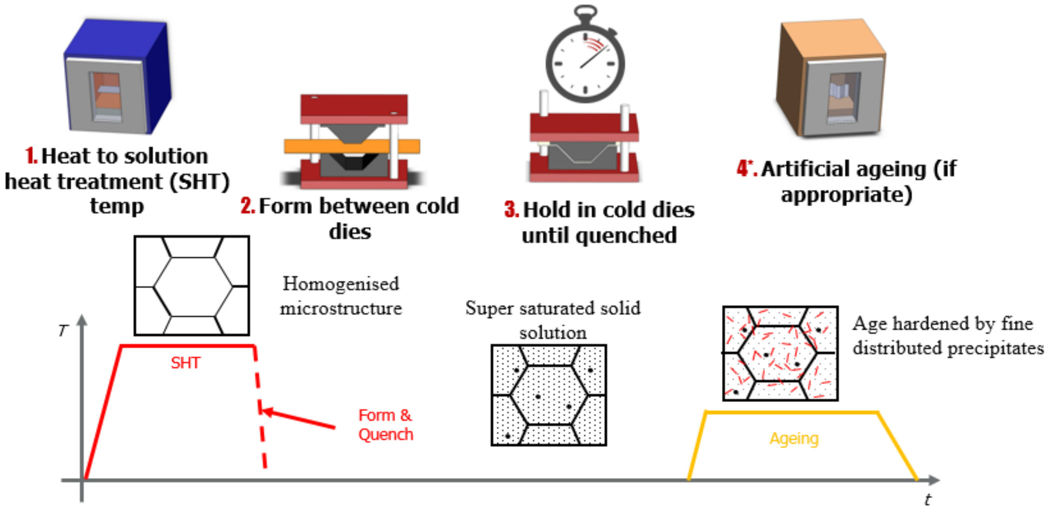

Figure 2.1 HFQ process (Imperial College London, 2017).

HFQ technology has been successfully applied in forming components from AA5xxx and AA6xxx sheets in recent years (Fakir et al., 2014, Mohamed et al., 2012, Garrett et al., 2005).

---

[1] HFQ® is a registered trademark of Impression Technologies Ltd.

However, due to the melting of low Cu rich eutectic melting phases, AA2xxx and AA7xxx materials have poor formability at SHT temperature, and thus it is not possible to form complex-shaped components using these materials via the HFQ process (Wang et al., 2011).

2.2 Introduction of AA7075 series aluminium alloys

AA7xxx series and AA2xxx series alloys are high/ultra-high strength aluminium alloys. AA7xxx series aluminium alloys are Al-Zn-Mg(-Cu) based alloys, with typical chemical compositions listed in Table 2.1. The good corrosion resistance, specific strength, fracture toughness and machinability of alloys such as AA7010, AA7050, and AA7075, make these materials ideal candidates in aeronautical and automotive applications (Heinz et al., 2000, Ward's Automotive, 2009). AA7075 is an ultra-high strength alloy, which was developed in the 1940s for manufacturing components for aviation(The Aluminum Association, 2015a). Compared to AA2xxx series high strength alloys, AA7075 has a high strength-to-density ratio with better resistance to corrosion, leading to its dominance in high strength industrial applications (Prasad et al., 2014).

Table 2.1*Chemical compositions of AA7xxx series materials(Campbell, 2006).*

Alloy	Si	Fe	Cu	Mn	Mg	Cr	Zn	Ti	Zr
AA7020	0.35	0.40	0.20	0.05–0.50	1.0–1.4	0.10–0.35	4.0–5.0	-	0.08–0.20
AA7075	0.40	0.50	1.2–2.0	0.30	2.1–2.9	0.18–0.28	5.1–6.1	0.20	-
AA7050	0.12	0.15	2.0–2.6	0.10	1.9–2.6	0.04	5.7–6.7	0.06	0.08–0.15
AA7150	0.12	0.15	1.9–2.5	0.10	2.0–2.7	0.04	5.9–6.9	0.06	0.08–0.15
AA7055	0.10	0.15	2.0–2.6	0.05	1.8–2.3	0.04	7.6–8.4	0.06	0.08–0.25
AA7085	0.06	0.08	1.3–2.0	0.04	1.2–1.8	0.04	7.0–8.0	0.06	0.08–0.15

AA7075-T6 is one of the most typical commercially available AA7075 sheet materials, having a yield strength of approximately 430 MPa and 510 MPa ultimate tensile strength. Commercial AA7075-T6 at room temperature display elongations at failure of 5-11%, which is considerably low to manufacture complex-shaped components via stamping processes (The Aluminum Association, 2015b). The production of AA7075-T6 temper sheet requires a series of steps as shown in Figure 2.2, namely: hot rolling, coiling, annealing, cold rolling, solution heat treatment, quenching and artificial ageing. Solution heat treatment temperature occurs above 450°C, with artificial ageing occurring at 120°C for 24-48 hours depending on the chemical composition. The T6 temper is achieved after quenching and artificial ageing. For a material that is naturally aged rather than artificially aged after quenching, a T4 temper is formed. As quenched and T4 temper materials exhibit lower strength compared to T6 temper, and their microstructures are un-stable at low or medium temperatures (Ma et al., 2014).

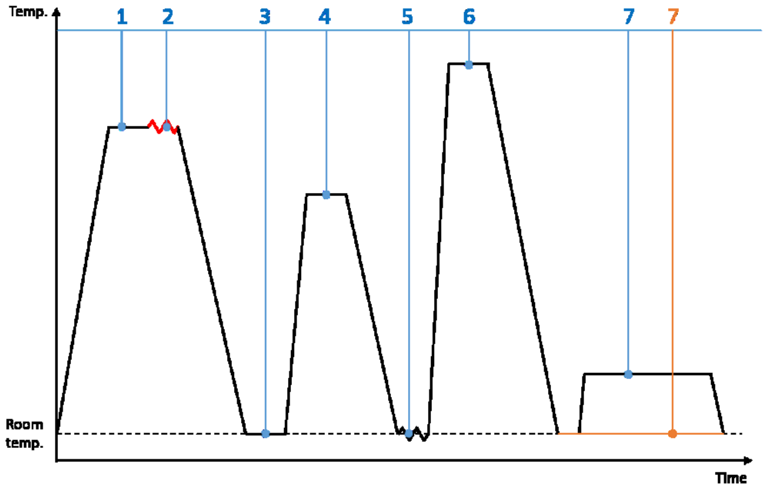

1. Pre-heating before hot rolling
2. Hot rolling
3. Coiling
4. Annealing
5. Cold rolling
6. Solution heat treatment & Quenching (**As quenched**)
7. Artificial ageing (**T6**)
7. Natural ageing (**T4**)

Figure 2.2 Temperature profile of producing processes of T6 and T4 temper materials.

Ductility

Hardening precipitates have a negative effect on material ductility, and therefore the ductility of T4 or as quenched material are greater than that of T6 temper material at room temperature (Esmaeili et al., 2003b). When the material is heated to a high temperature, the ductility also increases rapidly due to the dissolution of main hardening precipitates, leading to a positive relation between ductility and temperature for AA5xxx and AA6xxx series materials (Elfakir, 2015).

As opposed to AA5xxx and AA6xxx series materials, the ductility of AA7xxx and AA2xxx materials does not necessarily increase with increasing temperature (Wang et al., 2011). As can be seen in Figure 2.3, the elongation at failure of AA2024 initially increases as temperature is increased from 350°C to 450°C until reaching a peak value at 450°C, or close to its Solution Heat Treatment (SHT) temperature, and then declines rapidly with continuously increasing temperature. The main reason for this has been discussed in the literature. It is suggested that low melting eutectics phase (Cu and Mg enrichment) reduce ductility at elevated temperatures as the increased temperature provides more energy to melt these low-melting eutectics, leading to a lower ductility of the sample (Wang et al., 2011).

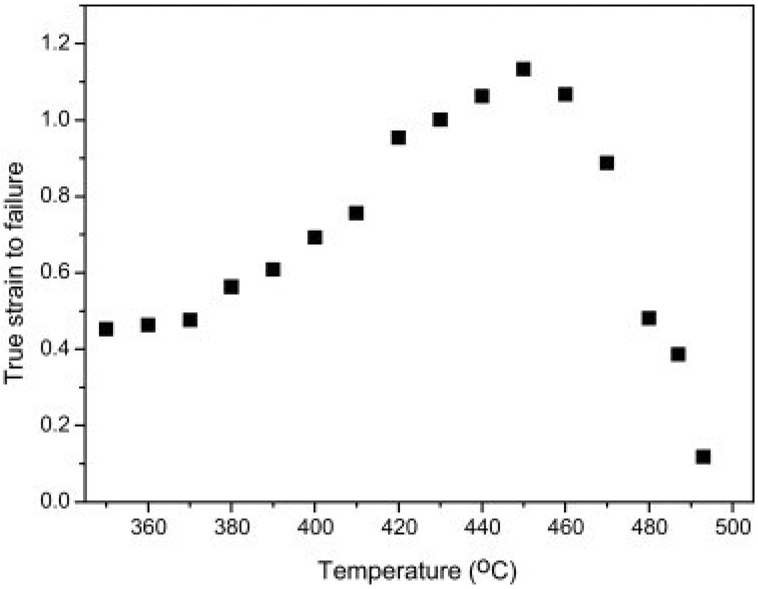

Figure 2.3 Ductility test results for AA2024 at different temperatures(Wang et al., 2011).

2.3 Precipitation hardening of AA7xxx

Precipitates are a group of solute atoms in the aluminium matrix, which prevent dislocations passing or cutting through the material. The strength of AA7075 is mainly dependent on the type, radius and volume fraction of precipitates (Shercliff and Ashby, 1990).

2.3.1 Precipitate types

There are three main types of precipitates contributing to the strength of 7xxx series aluminium alloys: GP (Guinier–Preston) zones, ɧ’(MgZn) and ɧ($MgZn_2$), among which the ɧ’ is the strongest one that improving the strength most. GP zones and ɧ’ are also low temperature phases that only nucleate and exist at low temperatures (Berg et al., 2001, Sha and Cerezo, 2004).

In addition, other types of precipitates may also form in AA7xxx alloys. Minor phases such as θ, θ’, S’ and Z phases exist in small quantities in the matrix and thus have a negligible effect on strength and ductility (Lim et al., 2003). Besides these precipitates, equilibrium phases S(Al_2CuMg) and T($Al_2Mg_3Zn_3$) are two main types that could be formed in AA7xxx alloys, although they provide significantly less contribution to strength compared to the ɧ’. ɧ, S and T are high temperature precipitates that are only formed at high temperatures. However, once formed, they are stable at low temperatures (Lim et al., 2003, Jiang et al., 2016). S phase is believed to nucleate rapidly as ɧ’ and ɧ are dissolving (Lim et al., 2003), and T phase is formed above 300°C with slow heating/cooling or soaking (Jiang et al., 2016). T phase is also found to continuously transform to S phase during high temperature soaking.

Solubility of the aluminium matrix has a positive relation with temperature, which means more solute atoms can be dissolved into the aluminium matrix at higher temperature. During soaking at or above solution heat treatment (SHT) temperature, the precipitates dissolve into the aluminium matrix and become individual solute atoms. When the dissolving process is completed, all solute atoms are finely distributed in the aluminium matrix and the material is fully solution heat treated (Labusch, 1970, Sha and Cerezo, 2004).

After solution heat treatment finishes, the material is quenched to room temperature. As temperature decreases, the solubility of the aluminium matrix reduces, and therefore the solute atoms nucleate into solids as precipitates again (Labusch, 1970, Starink and Wang, 2003). There are several precipitates which form at different temperature ranges and cooling rates. Figure 2.4 gives the Differential Scanning Calorimetry (DSC) during quenching of AA7150, and precipitation occurs at the areas where the solid line is above the dash line (Zhang et al., 2014). It is obvious that the gap between the two lines is reduced when the cooling rate increases. In another word, high cooling rate suppresses precipitation behaviour during quenching. It is found that when the cooling rate is higher than a critical value, precipitation behaviour is close or almost entirely eliminated (Berg et al., 2001). The critical value is 200°C/s for AA7075 cooled from around 490°C, and a Continuous Cooling Transformation (CCT) Diagram is plotted to show the critical quenching rate required from its SHT temperature. An example CCT diagram is shown in Figure 2.5, in which the area HT, MT and LT represent the areas with precipitation. If quenching occurs quickly, the cooling curve can avoid all areas and there will be no precipitation during quenching (Zhang et al., 2014).

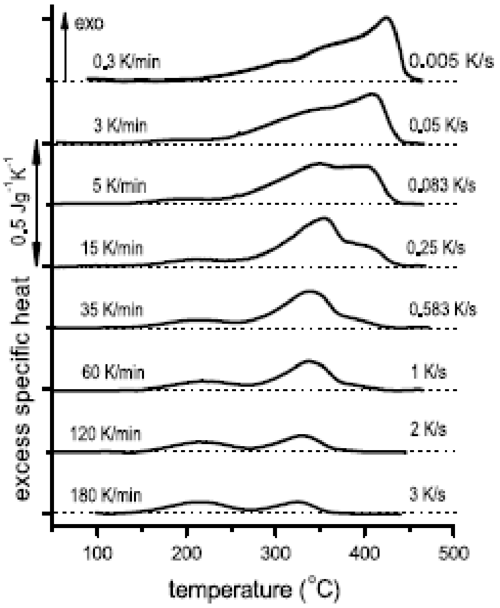

Figure 2.4 Differential Scanning Calorimetry (DSC) during continuous cooling at different cooling rates for AA7150(Zhang et al., 2014) .

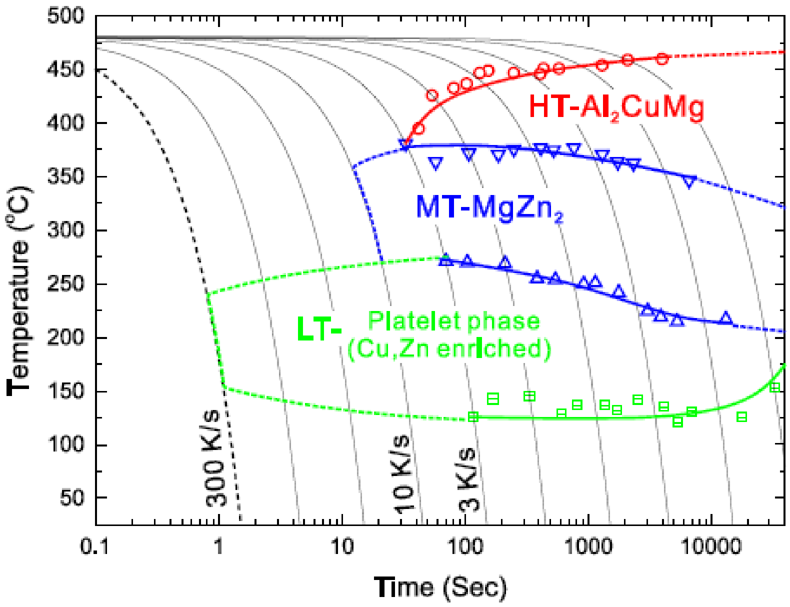

Figure 2.5 Continuous Cooling Transformation (CCT) diagram of AA7150 (Zhang et al., 2014).

Figure 2.6 gives an example of a Time-Temperature-Transformation (TTT) Diagram, and the solid curves are representative of different precipitate types. As opposed to CCT diagrams, the TTT diagram gives the temperature path not only from SHT temperature but from any temperature, starting from SSSS condition (Saunders, 2004). If the temperature evolution curve crosses any of the solid curves, nucleation of the corresponding precipitate will occur.

According to the TTT diagram, if heating is faster than a critical heating rate for SSSS condition material, and the temperature evolution curve does not cross any of the precipitation areas, there would be no precipitates formed during heating. It could also be deduced from Figure 2.7, the DSC results for heating with different heating rates show that the precipitation behaviour is depressed with higher heating rate (Osten et al., 2015). However, due to the heating rate limit of existing equipment, there is no proof showing a heating process exhibiting no precipitation.

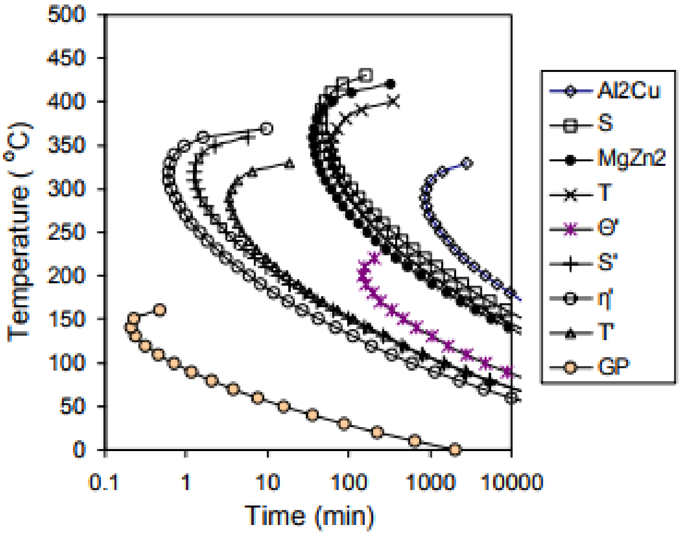

Figure 2.6 Calculated Time-Temperature-Transformation (TTT) diagram of AA7075 (Saunders, 2004).

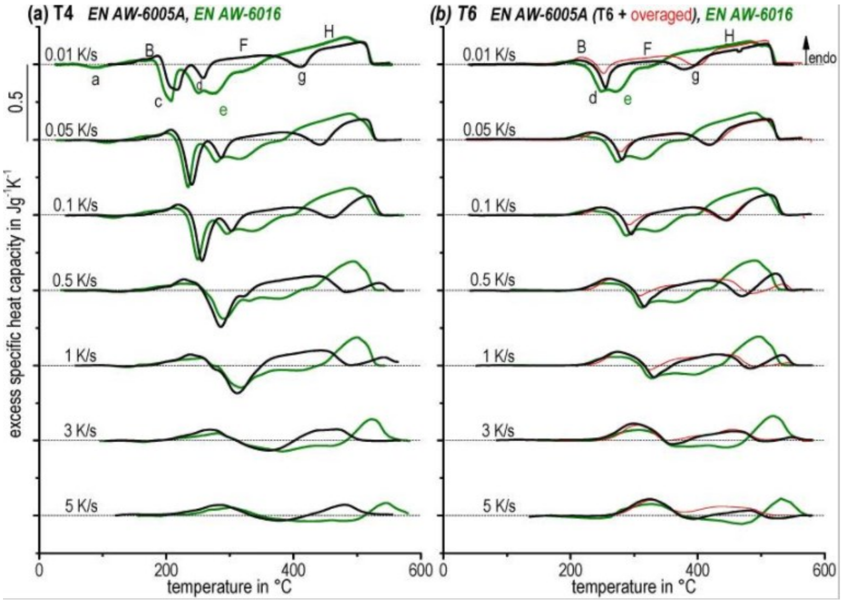

Figure 2.7 Differential Scanning Calorimetry (DSC) continuous heating curves for EN AW-6181 with (a) T4 and (b) T6 initial conditions at different heating rates (Osten et al., 2015).

With a high quenching rate, almost no precipitates nucleate and all solute atoms are finely distributed within the aluminium matrix. The condition of material is called as quenched condition and its microstructure is SuperSaturated Solid Solution (SSSS), which is a very unstable condition because the solute concentration is higher than the solubility of the matrix at room temperature (Sha and Cerezo, 2004). If artificial ageing is conducted immediately after quenching, the material generates its T6 temper when peak aged. If the material is left for room temperature storage after quenching, it becomes T4 material after natural ageing to peak strength.

It is widely accepted that the precipitation sequence during artificial ageing from SSSS is (Berg et al., 2001):

SSSS----GP zones---- ɧ’(MgZn)---- ɧ($MgZn_2$)

There are two types of GP zone (Berg et al., 2001): spherical GPI zones and plate-like GPII zones. GPI zones are nucleated with solute-rich clusters and fully coherent zones, and they are formed at a wide range of temperatures from low temperature to approximate 140-150°C (Sha and Cerezo, 2004). GPII zones are formed from vacancy-rich clusters (VRC) only at temperatures above 70°C, and they are more thermally stable than GPI zones. However, both types of GP zones are unstable even at low temperatures (Liu et al., 2015b). Both types of GP zones transfer into metastable phase ɧ’ with longer ageing time at around 100°C or higher, and become the equilibrium precipitate ɧ. However, at temperatures above 190-200°C, the GP zones will dissolve again instead of converting to ɧ’. ɧ is formed from ɧ’, which is the equilibrium phase which is stable at low temperature but does not have the strength of ɧ’. The precipitation sequence is thus refined as (Li et al., 1999, Berg et al., 2001):

SSSS----GPI zones---- ɧ’---- ɧ

SSSS----VRC----GPII zones---- ɧ’---- ɧ

It is suggested that GP zones do not transfer to ɧ’ at low temperature ageing. Natural ageing occurs at room temperature (Berg et al., 2001), which is normally lower than 50°C, and therefore there should be GPI zones only and no GPII zones, ɧ’ or ɧ in the T4 temper materials. It is found that natural ageing has a negative effect on the artificial ageing efficiency and peak aged strength if artificial ageing is taken after natural ageing (Magalhães et al., 2014, Liu et al., 2015b). It is therefore suggested that the material should be sent to artificial ageing immediately after quenching to avoid natural ageing if the highest strength is required after artificial ageing.

T6 temper is generated after 24-48 hours artificial ageing at approximately 120°C. It is commonly accepted that the peak hardness and strength is associated with finely distributed ɧ' phase, and may contains a small amount of GP zones and ɧ (Li et al., 1999).

2.3.2 Size and volume fraction of precipitates

As discussed at the beginning of this section, size and volume fraction of precipitates are important factors for strength and hardness as well as the type. Figure 2.8 reveals the factors contributing to strength in 6xxx aluminium alloys and the evolutions of the precipitates during artificial ageing, when only one type of precipitate is taken into consideration. Since ɧ' is the main phase having the maximum hardening effect, these factors are also important when considering peak ageing of AA7xxx materials from SSSS (Shercliff and Ashby, 1990).

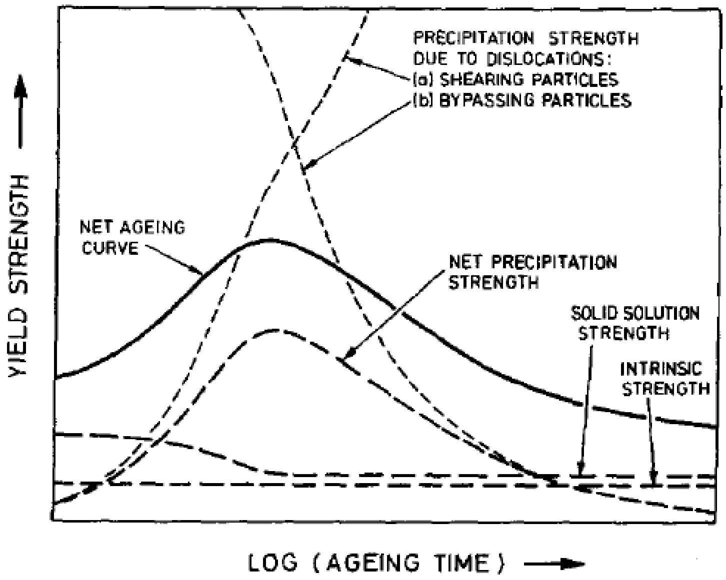

Figure 2.8 *A schematic diagram of the relative contributions to the full ageing curve of the intrinsic strength, solid solution strength, and precipitation hardening due to shearable and non-shearable particles; note that the effective mechanism of precipitation hardening is the one requiring the least shear stress, with a smooth transition between the two (Shercliff and Ashby, 1990).*

The solid line 'Net Ageing Curve' in the figure shows the changes of the strength with ageing time, which is combined by three elements: intrinsic strength, solid solute strength and net precipitation strength. Intrinsic strength indicates the strength of pure aluminium matrix, which stays stable regardless of temperature variation (Shercliff and Ashby, 1990, Starink and Wang, 2003). Solid solute strength means the contribution to obstruct the dislocations made by solute atoms in aluminium matrix, whose change is not obvious. It decreases at the beginning of the ageing process, and becomes stable after a few hours of ageing, when most solute atoms exceeding the solubility at that temperature are precipitated until the material achieves its equilibrium condition. Net precipitation strength reveals the strength contributed by precipitates, and it is affected by two main factors: size and volume fraction, which appears as the strength against shearing and bypassing.

It is widely accepted that the equilibrium volume fraction of precipitates is highly dependent on ageing temperature (Shercliff and Ashby, 1990, Ardell, 1972, Papazian, 1981). Within the temperature range for precipitation, a higher ageing temperature leads to a lower equilibrium volume fraction. With the same level of average precipitates size, a higher volume fraction results in a higher strength, and therefore, a lower ageing temperature could give a higher peak precipitation strength. It is found that volume fraction increases rapidly at the initial stage of ageing and achieves its equilibrium quickly before becoming stable, with coarsening subsequently occurring (Shercliff and Ashby, 1990).

Precipitation coarsening occurs with ageing, where the average radius of precipitates increases with a longer ageing time, until all solute atoms available to nucleate are formed into this type of precipitate. A higher temperature would accelerate the coarsening process because there is more energy for coarsening behaviour. When the radius of the precipitates is small, the precipitates are unable to prevent dislocations from cutting them through. With an increasing average size, the precipitates are harder to be cut through, although it becomes easier for dislocations to bypass them. As a result, the strength against shearing increases with longer ageing time and that against bypassing decreases. Since the volume fraction is constant after a short ageing time, the change of precipitation strength is mainly affected by coarsening. The precipitation strength evolution during ageing combines the effects of increasing strength to shearing and decreasing strength to bypassing, and it decreases after the peak, where the material is peak aged (Shercliff and Ashby, 1990, Ardell, 1972, Esmaeili et al., 2003a, Li et al., 1999).

2.3.3 Double ageing

Double ageing, also named two stage ageing, is an efficient artificial ageing method to reduce the ageing time (Emani et al., 2009, Stiller et al., 1999, Kashyap et al., 2000, Wang et al., 2008). The process of double ageing is shown in Figure 2.9. The material is artificial aged at a low temperature after quenching, followed by a high temperature ageing process. The low temperature ageing is also called first stage ageing, and it normally ranges from 90°C to 150°C for AA7xxx series materials, while the high temperature ageing called second stage ageing, ranges from 140°C to 200°C (Hatch, 1984). The temperature and time are highly dependent on chemical compositions of materials. The highest possible strength after double stage ageing is very close to that of T6 temper, and it is found that there are more ђ' and less GP zones in the peak double aged material compared to the single stage aged T6 temper material, which results in greater microstructure stability after ageing.

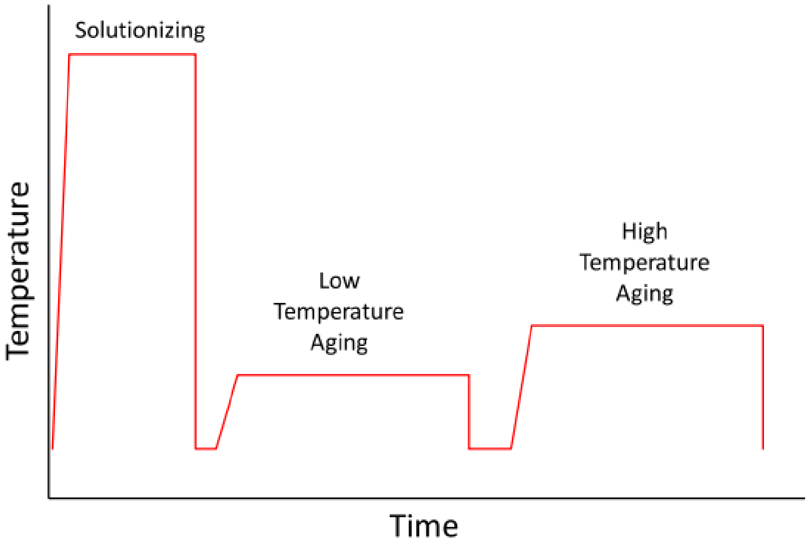

Figure 2.9 Temperature profile of double ageing process (Emani et al., 2009).

An example of double ageing hardening results for AA7075 is given in Figure 2.10. The temperatures for two ageing stages are 121°C and 177°C. It is seen that with 55min first ageing and 65min second ageing, the hardness reaches the same level with the single ageing peak value at 121°C. It takes only 2 hours for double stage ageing to achieve the same hardness as single aged 48 hours, which saves 96% of ageing time (Emani et al., 2009).

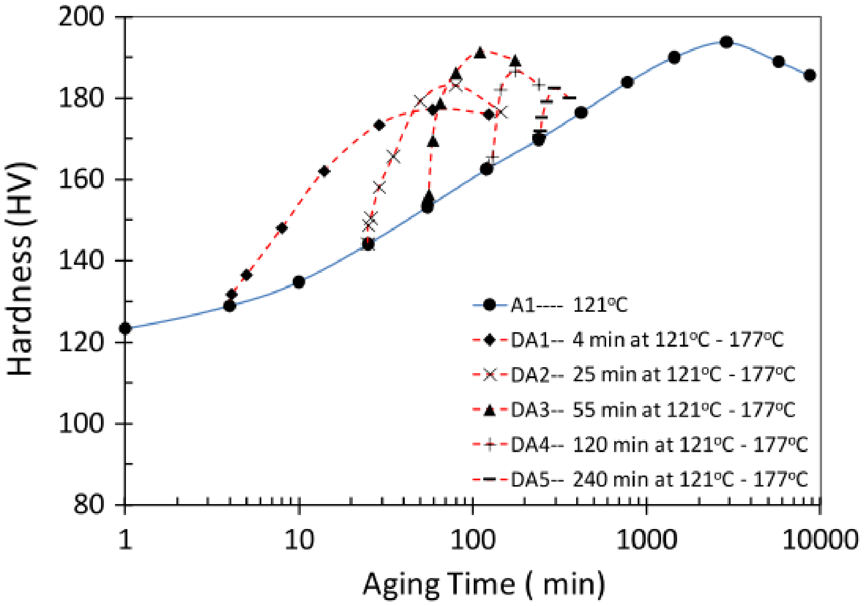

Figure 2.10 *Effect of time of first aging on double aging of AA7075 Alloy (Emani et al., 2009).*

During the first stage ageing, GP zones are formed (Sha and Cerezo, 2004). As discussed above, equilibrium volume fraction decreases with increasing ageing temperature, and in this case the equilibrium value at 121°C is higher than that at 177°C (Ardell, 1972). Defining f as volume fraction of the material of ɧ’, f_{121} as the equilibrium volume fraction at 121°C, and f_{177} as that at 177°C, thus f_{121} is greater than f_{177}. As seen in Figure 2.11(a), during a short first ageing such as 4 min and 25 min, the volume fraction f increases during the ageing but is still lower than f_{121}. Therefore when it is transferred to the high temperature 177°C with a lower equilibrium volume fraction f_{177}, f continues increasing and approaches f_{177}, which is lower than f_{121}. The lower volume fraction results in a lower peak aged strength. As shown in Figure 2.11(b), if the first ageing time is long, f achieves the same value as f_{121}, and when it is transferred to a high temperature ageing, f continues to be equal to f_{121} which is greater than f_{177}. Hence a high peak hardness can be achieved similar to single stage ageing at the lower temperature of 121°C. Since the high temperature at the second ageing stage provides more energy for nucleation, the coarsening and transformation is accelerated, thus significantly reducing production time (Berg et al., 2001, Ardell, 1972, Stiller et al., 1999). However, if the ageing time of the first stage further increases, some of the GP zones begin to transform to ɧ’, which will further transform to ɧ phases at high temperature ageing. Since the strength of ɧ is lower than ɧ’, the formation of ɧ reduces the peak aged hardness, and results in a lower peak hardness. Hence double ageing with a very long first ageing stage results in reduced peak hardness (Starink and Wang, 2003, Emani et al., 2009).

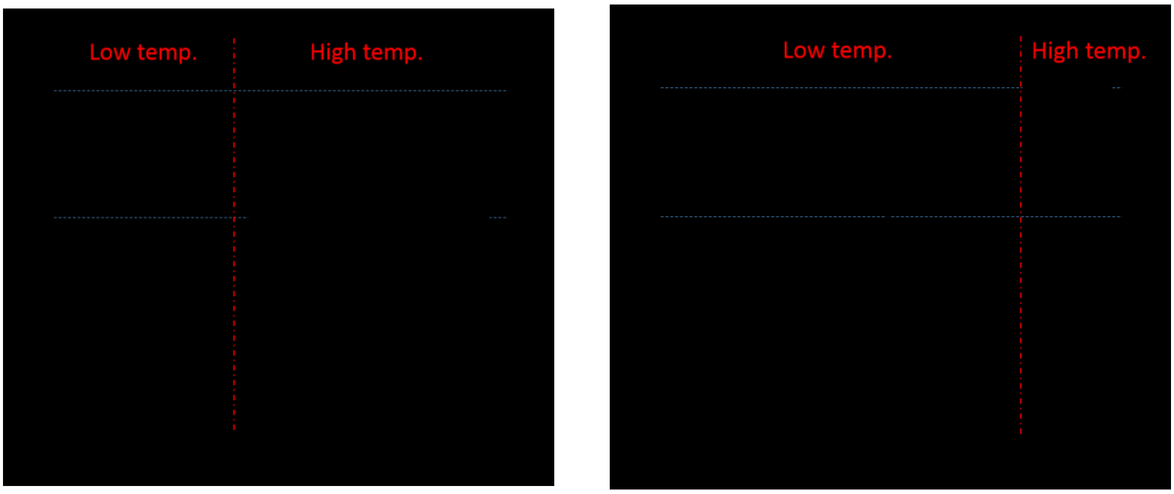

(a) (b)

Figure 2.11 *Volume fraction evolution during double ageing with (a) short first stage low temperature ageing; (b) long first stage low temperature ageing.*

2.4 Interfacial heat transfer coefficient

As reviewed above, cooling rate is critical for maintaining the SSSS condition during quenching in order to retain the full post form strength. The determination of interfacial heat transfer coefficient (IHTC), which is used to calculate the heat exchange between the blank material and tools, is an important variable to calculate and predict the quenching rate. Significant efforts have been made in the literature to measure or calculate the IHTC values. In this project, test equipment have been designed and models developed to determine the IHTC behaviour.

2.4.1 Equipment for the characterisation of IHTC

The clamping method is widely used in IHTC tests, where the test blank is heated, transferred to a set of punch and die, and finally the press activated to clamp the blank and record the temperature evolutions. The temperature evolution results are used to calculate the IHTC value between tool and blank. There are two methods to calculate the IHTC value: (i) from the temperature evolution of the blank/workpiece and (ii) the temperature evolution of tools. These methods are discussed below.

Method one: recording workpiece temperature

Bai et al. (2012) experiments were conducted on test equipment shown in Figure 2.12. A Ti-6Al-4V cylindrical workpiece was heated to 920℃ in a furnace while the H13 tools were heated to 150℃ by a band heater. After heating, the workpiece was transferred into the tool set and was pressed at different pressures. Temperature evolution of the blank was recorded by 3 pairs of K-type thermocouples connected to a N19205 module data logger, with the measured curve compared to the computed curves derived from a numerical model to identify the corresponding IHTC values. Hu et al. (1998) applied a similar method to identify IHTC values for Ti-6Al-4V. Bosetti et al. (2010) designed a toolset for hot stamping of boron steel Usibor 1500P2. The blank was heated to 950℃ and rapidly transferred to a press machine, and was compressed under different pressures ranging from 5 MPa to 30 MPa. Ni/Cr-Ni-thermocouples were used to record the temperature evolutions of the interface between the blank and the dies.

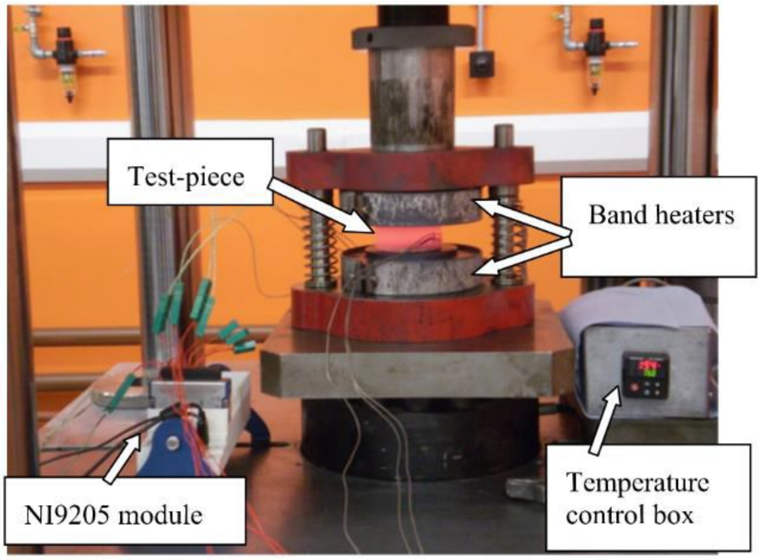

Figure 2.12 Equipment for the characterisation of IHTC for Ti-6Al-4V(Bai et al., 2012).

IHTC values for aluminium alloys, such as 2024-T4, 2024-O, 1100-O and 6061-O, were determined by Jain (1990) using a similar method. A workpiece was heated to different temperatures ranging from 200℃ to 400℃ and was transferred to a water-cooled tool set. The temperature evolution of workpiece was recorded via thermocouples and the IHTC values were determined via calculation based on the results.

Method two: recording tool temperature

Temperature evolutions of tools, rather than workpiece, have been measured by some researchers to calculate the IHTC values for workpiece materials. In Hu et al. (2013)'s tests, a high strength steel B1500HS workpiece was heated to 900°C and then transferred in between the two dies, and was pressed at different contact pressures . The temperature of tools made of H11 tool steel were monitored and recorded by a MX100 instrument as shown in Figure 2.13, with the data used to calculate the IHTC between tools and workpiece. An FE model was developed in ABAQUS and was used to simulate the process, with the temperature curves of tools from both experimental and simulation results compared to determine the IHTC value at different pressures. A similar equipment and FE simulation was employed by Chang et al. (2016) as well to determine the IHTC values for 2 mm thick 22MnB5 steel blank. Chang and Bramley (2002) used a similar test method without FE simulation, comparing instead the least-square numerical analysis to determine IHTC values.

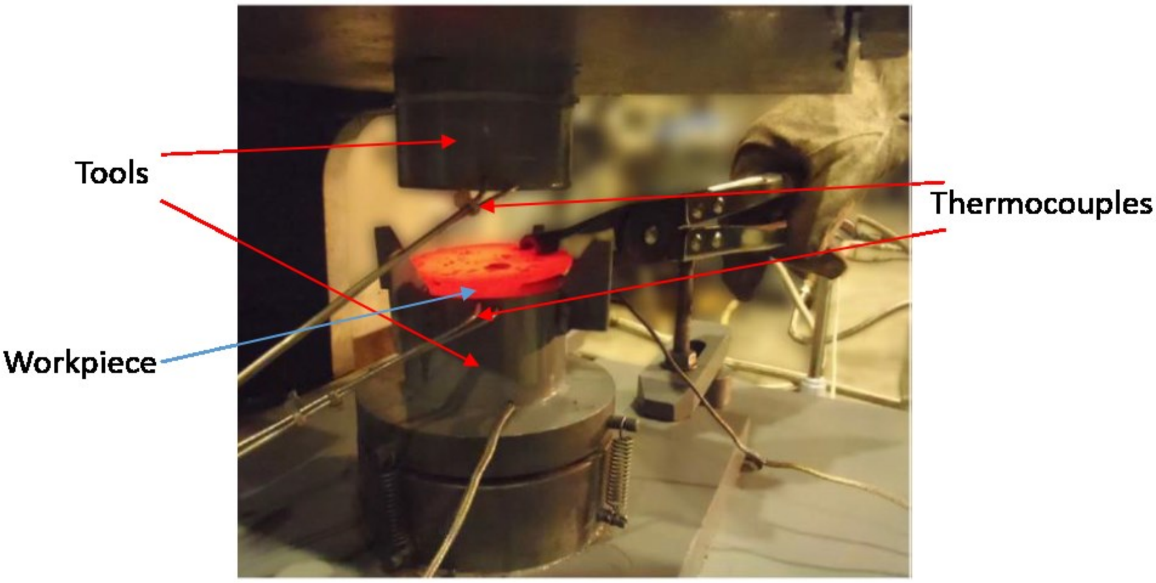

Figure 2.13 Equipment for the characterisation of IHTC for B1500HS(Hu et al., 2013).

A Hot stamping simulator has been designed and presented in Chapter 3 of this thesis, and one of its two main functions is to conduct IHTC tests for hot stamping processes. The design has incorporated elements of testing methods and designs presented in the literature.

2.4.2 Effect of contact pressure on IHTC

It is widely accepted that contact pressure is one of the main factors influencing the IHTC value. A typical exponential increasing trend of IHTC with pressure was found by Bai et al. (2012) with IHTC increasing significantly from 0.55 to 5.8 kW/m^{2}K when the contact pressure increased from 0 to 100 MPa. This subsequently increased slightly before reaching its peak plateau of 6 kW/m^{2}K at approximately 200 MPa. Similar trends were found in other studies (Yukawa et al., 2014). As shown in Figure 2.14, the IHTC value grew exponentially with contact pressure from 0 to 20 kW/m^{2}K, and converged after 300 MPa.

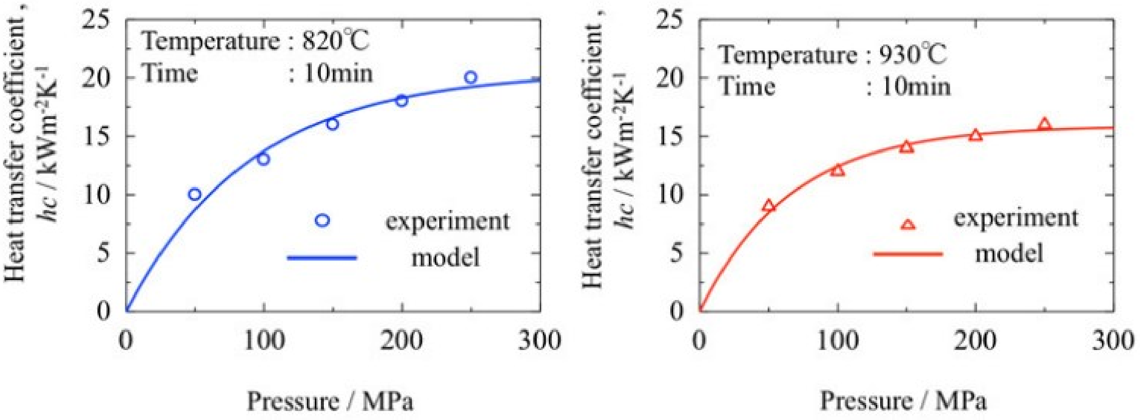

__Figure 2.14__ Heat transfer coefficient as a function of contact pressure at 820℃ and 930℃(Yukawa et al., 2014).

The linear increasing trend was also reported by Hu et al. (2013), Lee et al. (2012) and Hung et al. (2014). It was found that IHTC between B1500HS workpiece and H11 tools increased linearly from 4 kW/m^{2}K to 6.3 kW/m^{2}K while the pressure increased from 8 MPa to 42 MPa in Hu et al. (2013)'s studies. A similar trend was found in Lee et al. (2012)'s experiments, while IHTC value raised at a rate of 0.75 kW/m2K per 1 MPa increasing contact pressure (Figure *2.15*).

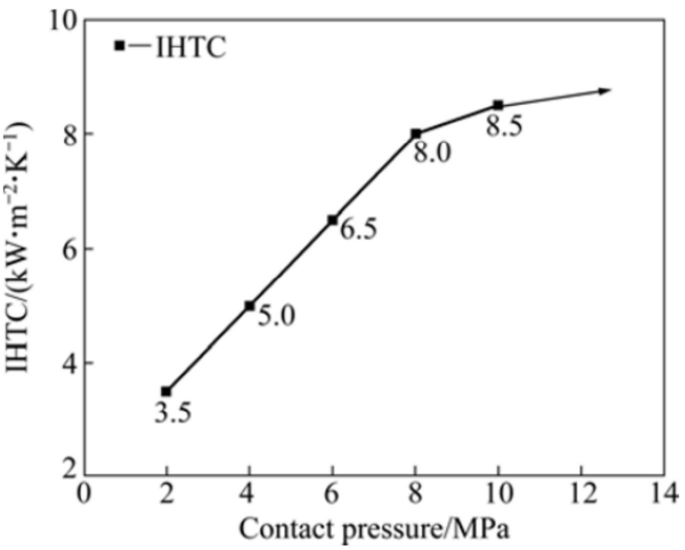

Figure 2.15 *Heat transfer coefficient as a function of contact pressure for Al5083(Lee et al., 2012).*

The relationship between the real and apparent contact area is believed to lead to this increasing trend. There are many asperities on surfaces as shown in Figure 2.16(b), and when two surfaces contact each other under a pressure, some of the asperities are deformed as Figure 2.16(c). The real contact area is the effective area where asperities on one of the contacting surfaces are pressed tightly to the other surface. The Real contact area in Figure 2.16(c) is smaller than the apparent contact area in Figure 2.16(a). Heat transfer between the two contact surfaces occurs mainly through two ways: (i) across the real contact areas, and (ii) across the air between the two surfaces. The heat transfer across air is slow compared to direct contact between metals. With a higher pressure, the elastic and plastic deformations of asperities increase, and thus the real contact area increases leading to an increasing trend of IHTC (Liu et al., 2017). However, when the ratio of the real to the apparent contact area reaches a large value, further increasing pressure will not cause further deformation on the asperities, and thus the IHTC value reaches a plateau (Shlykov et al., 1977).

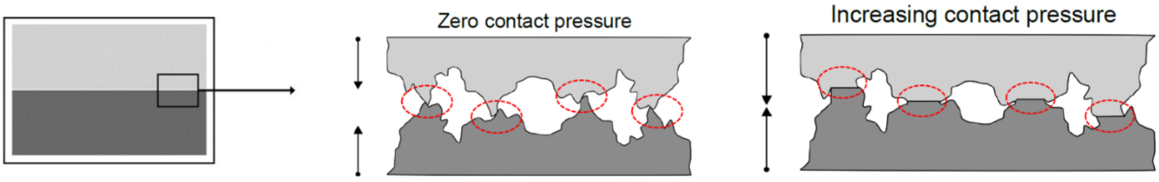

(a) (b) (c)

***Figure 2.16** (a) Apparent contact area; (b) Asperities on surfaces; (c) Real contact area (Hölscher et al., 2008, Liu, 2015).*

2.4.3 Effect of lubricant on IHTC

Lubricant applied on the contact surfaces participates in the heat exchange between two solids. This has led to significant research being conducted in the literature to study the effect of lubricants on IHTC value.

A positive effect of grease based Graphite lubricant on IHTC was found by Foster et al. (2008). IHTC between mild steel dies and AA6082 blank at 0-load contact increased from 0.8 kW/m^{2}K under dry condition to 3 kW/m^{2}K under the lubricated condition. Jain (1990) presented similar results with MoS_2 lubricant, and R. Burte et al. (1990) found that IHTC value doubled with use of graphite in water suspension lubricant compared to the dry condition at the same pressures. However, a reverse trend was found in the study of IHTC with the application of glass as lubricant. As seen from Figure 2.17, IHTC value with glass lubricants was approximately half of that under dry condition at 40 MPa pressure (Bai et al., 2012).

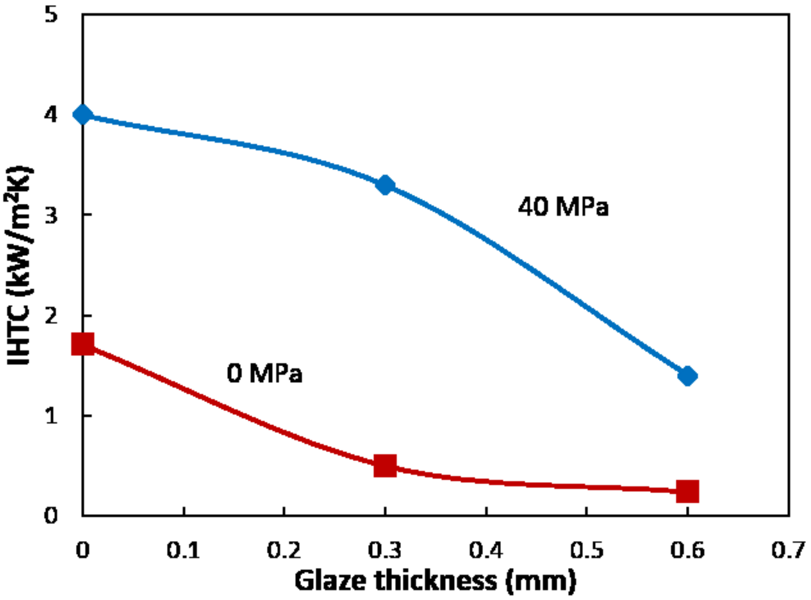

Figure 2.17 Effect of glass thickness on IHTC with 0.8 µm roughness (Bai et al., 2012).

As discussed above, there are two means of heat transfer between contacting surfaces, one is across real contact areas, and the other is through the air between the contacting surfaces. Once lubricant is applied on the surface, some of the gaps around the asperities are filled by the lubricant instead of air, as shown in Figure 2.18. Thus the heat must be transferred through the lubricant (Wilson et al., 2004). If the lubricant, such as Graphite based lubricants have a higher thermal conductivity than air, the heat flow through the lubricant is greater, thus increasing the overall heat transfer and IHTC value. If a lubricant such as glass is used with a lower thermal conductivity than air, the IHTC is therefore reduced.

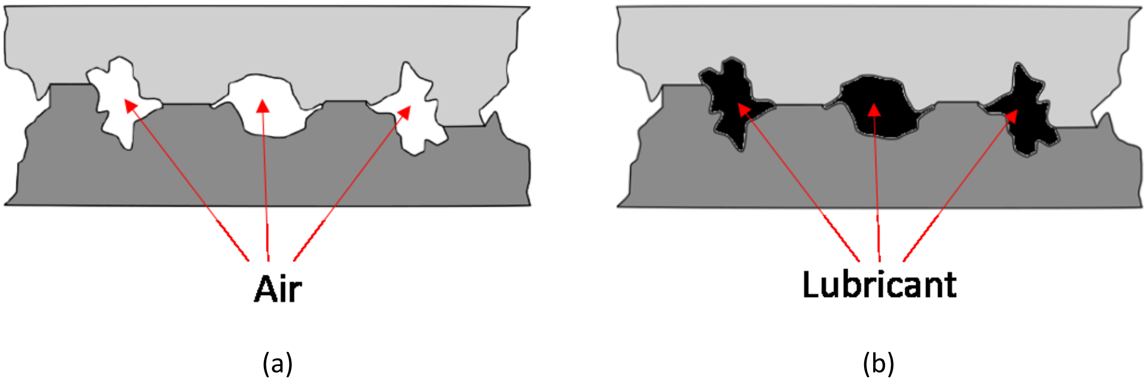

Figure 2.18 The asperities between the contact interfaces of two solids, filled up by (a) air or (b) lubricant (Liu, 2015).

2.4.4 Theoretical models for the characterisation of IHTC

As discussed above, the IHTC value between two contacting solids is highly dependent on material, contact pressure and lubricant. Centinkale and Fishenden's equation (Liu et al., 2017) is widely used to estimate the general heat transfer coefficient h:

$$h = h_g + h_c \tag{2.1}$$

where h_g is heat transfer across the solid contact of real contact area and h_c is that across air gap.

Withers and Cooper (2009) expressed a theoretical power function model for IHTC (Eq. 2.2) as equation based on the thermal conduct theory from Cooper et al. (1969):

$$h = 1.45k\frac{tan\,\theta}{\sigma}(\frac{p}{H})^{0.985} \tag{2.2}$$

where k is the mean thermal conductivity of two contact bodies, θ is the mean of the absolute slope of the surface profile, σ is the standard deviation of the profile heights, p is contact pressure between two contact surfaces and H is hardness of the workpiece.

A power relationship between the IHTC and contact pressure was also developed as an empirical model by Shlykov et al. (1977):

$$h = 8000\bar{\lambda}(\frac{P}{C\sigma_U}K)^{0.86} \tag{2.3}$$

where $\bar{\lambda}$ is the mean thermal conductivity of the two contact bodies, P is contact pressure between them, σ_U is the ultimate tensile strength of the test specimens, and K and C are model coefficients.

An equation was developed by Wilson et al. (2004) to predict the IHTC values under different lubricated conditions:

$$h = \frac{1-A}{h_f} \frac{2k_f k_t k_w}{2k_t k_w - k_w k_f - k_f k_t} \tag{2.4}$$

where A is the fractional contact area which is the ratio between real contact area and apparent contact area, h_f is the applied lubricant thickness, and k_f, k_t and k_w are the thermal conductivities of the lubricant, tool and workpiece respectively.

In Chapter 4, IHTC experiments have been designed and tested based on the information reviewed in Section 2.4.3, and an IHTC model to predict the IHTC value as functions of contact pressure, lubrication condition and tool/blank materials was developed based on the reviewed equations above and experimental results from Chapter 4.

2.5 UNI-form

UNI-form is a pilot automatic production line for FAST designed by researchers in the Mechanics of Materials research group in the Mechanical Engineering Department at Imperial College London, based on a 100-ton Phoenix press machine shown in Figure 2.19 (a). The upper and middle platform of UNI-form is shown in Figure 2.19 (c), and the test blank is shown in Figure 2.19(b). UNI-form has the capability to form the components automatically, replicating the cycles from heating to incubation, and uses a conductive heater, punch, die, blank holders, and an incubation chamber. As seen from the figure, a dual-conveyer belt is attached to each end of the platform, having the capability to move both forwards and in reverse to transfer blanks from one process to another. A controller is connected to both conveyor belts and the press machine.

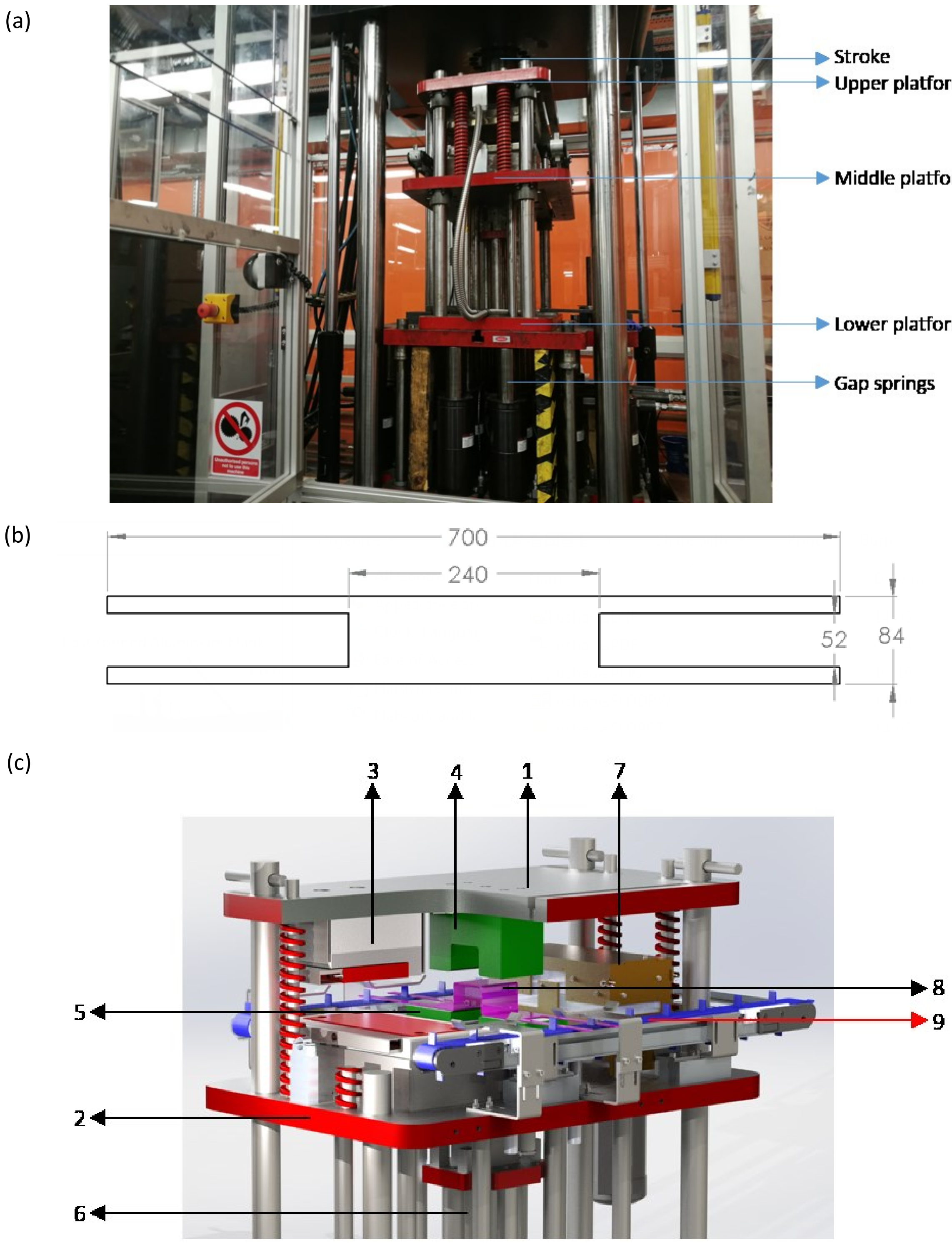

1.Upper platform 2.Middle platform 3.Heater 4.Die 5.Blankholder

6.Punch 7.Incubation chamber 8.Blank (formed) 9.Conveyor Belt

Figure 2.19 (a) Phoenix press machine; (b) Blank dimensions (mm); (c) UNI-form system (Luan et al., 2017).

As shown in the Figure 2.19(a), UNI-form has 3 platforms and the lower platform rests on 28 x 10 kN Gas springs applying a maximum 280 kN supporting force, which are all connected to two gas tanks maintaining equal pressure across all the gas springs. A valve system enables constant gas spring force during compression by re-circulating the gas nitrogen to tanks. The punch rests on and is supported by the lower platform. Lower half of the heater, lower blankholders and incubation chamber are fixed on the middle platform, whilst the upper half of heater and die are fixed to the upper platform. The UNI-form weighs approximate 500 kg without the gas springs located on the bottom.

The upper platform is supported by 4 springs from the middle platform to sustain its mass, and is driven by the stroke of the press machine. The upper half of the conductive heater and the upper die are all attached to the upper platform and move together with it. When the stroke moves downwards, the upper platform moves downwards with the upper heater and die together, and the four springs are pressed. Die and lower blankholders are first contacted, and two small gas springs seated on the middle platform support the lower blankholders by applying blank holding force. There is a hole on the plate between the two blank holders, which allows the punch through the plate and is driven by the lower platform. Thus the punch does not move with the middle platform. As the stroke is lowered, the die, blank and punch are fully contacted and pressed, and it pushes the lower platform down with the punch. The gas springs are then pressed and engaged to apply the full compression force.

The UNI-form pilot production line has the advantages of high heating rate and full-automatic operation. The conduction heater as part No. 3 in Figure 2.19(c) could supply extremely high heating rate up to 300°C/s under high contact pressure. The test machine is controlled by a programmable controller, while the blank is transferred between heating, stamping and incubation by conveyor belts as part No. 9 in Figure 2.19(c), therefore the heating rate and time, transfer, stamping force and time, incubation temperature and time are all flexible and controllable with UNI-form. The accuracy of heating time, transfer time, stamping & quenching time and incubation time are precisely controlled within 0.1 s, higher level than most industrial production line.

2.6 Conclusion

In the present chapter, forming technologies, mechanical properties and microstructures of AA7xxx sheet metal have been reviewed. Based on these existing knowledge, a novel forming technology, Fast light Alloy Stamping Technology (FAST), has been developed. The deep understanding of the microstructure evolutions enables FAST to form complex-shaped high/ultra-high strength components from aluminium sheet alloys at a very high production rate. It also guides the design of experiments in Chapters 5 and 6 to determine the critical forming parameters and to optimise them. Interfacial heat transfer coefficient (IHTC) test methods, theories and models were reviewed as well. A new IHTC test method was developed in Chapter 4 using the hot stamping simulator designed in Chapter 3, giving high accuracy and complex programmable control. Based on the test results and theories reviewed in this chapter, a new IHTC numerical model was developed fitting very well with the experimental results. The IHTC model was used to predict the local quenching rates of blank and critical quenching time of components in FAST tests. The optimised forming parameters of FAST for the current 2 materials were applied and programmed in UNI-form pilot production line, in order to verify the FAST process and the parameters.

Chapter 3

Hot Stamping Process Simulator

3.1 Introduction

FAST is a novel mass production technology for the forming of panel components from aluminium alloy blanks. Due to its requirements of high heating rate, high quenching rate and high forming speed, there was no existing test equipment available that can simulate and monitor the entirety of the stamping process and more specifically, the temperature evolution of the components, and the applied force. Thus, a new production simulator system was developed in order to investigate the FAST process, and is presented in this chapter.

3.2 Production Simulator Overview

As reviewed in Chapter 2, quenching rate is critical to obtain the desired microstructure and thus to achieve a high post-form strength (Milkereit et al., 2009, Milkereit et al., 2014). The IHTC between the specimen and tools is an important parameter to characterise the quenching rate of the specimen during forming and quenching stages, and for calculation of quenching time as well. Significant research efforts have been made to determine the IHTC during forming (Bai et al., 2012, Ji et al., 2016). However, due to limitations in reading frequency and force control, to date, test equipment for the investigation of high speed thin blank forming with high complexity and accuracy has not been available.

As a result, a hot stamping simulator was developed to work in conjunction with the Gleeble 3800 thermo-mechanical testing machine, due to its high speed and accurate load and displacement capabilities. The simulator, in conjunction with the Gleeble 3800 simulates the temperature and force evolution of the aluminium alloy specimen, and enables determination of the IHTC values between specimen and tools during hot stamping processes. The hot stamping simulator must meet the following requirements:

1. Size constraint: The Gleeble chamber inner dimensions are 520 mm x 290 mm x 390mm, and the maximum distance between the two extension arms is 240mm.

Thus, the space to locate the simulator and space for punch movement are limited by these dimensions.

2. Moving speed & stamping force: In this stamping process, the moving speed of the punch can be up to 500 mm/s, with a compressive pressure exceeding 20 MPa.
3. High heating & quenching rate: As reviewed in Chapter 2, higher quenching rate results in lower precipitate formation during quenching, and thus in the FAST process, the heating and quenching rates could be as high as 150-200°C/s. Thus, the hot stamping simulator must endure rapid thermal changes.
4. Electrical insulation: The workpiece is heated by electric current, therefore the cables need to be insulated in order to prevent a short circuit.
5. Reversibly moveable: After the forming and quenching stages, the workpiece may need to be re-heated again, which requires the workpiece to be moved away from the punch and die.
6. Convenience of changing punch/die and workpiece: It is necessary to change the workpiece after each test, therefore ease of assembly is a design priority. Moreover, to achieve the objectives of this project, such as the study tool material on IHTC values, the punch/die needs to be changeable and their positions need to be easily calibrated.
7. Convenience on applying lubricant on die/punch: It is necessary to study the effect of lubricant on IHTC value, therefore it must be easy to apply and remove lubricant on punch and die contact surfaces.

As described above, the hot stamping simulator was designed to be integrated into the Gleeble 3800 thermal-mechanical simulator. The Gleeble 3800 machine is shown in Figure 3.1(a), and is controlled by a computer using the software QuickSim 2 to program the test parameters. Figure 3.1(b) and (c) show the Gleeble chamber where the hot stamping simulator will be located.

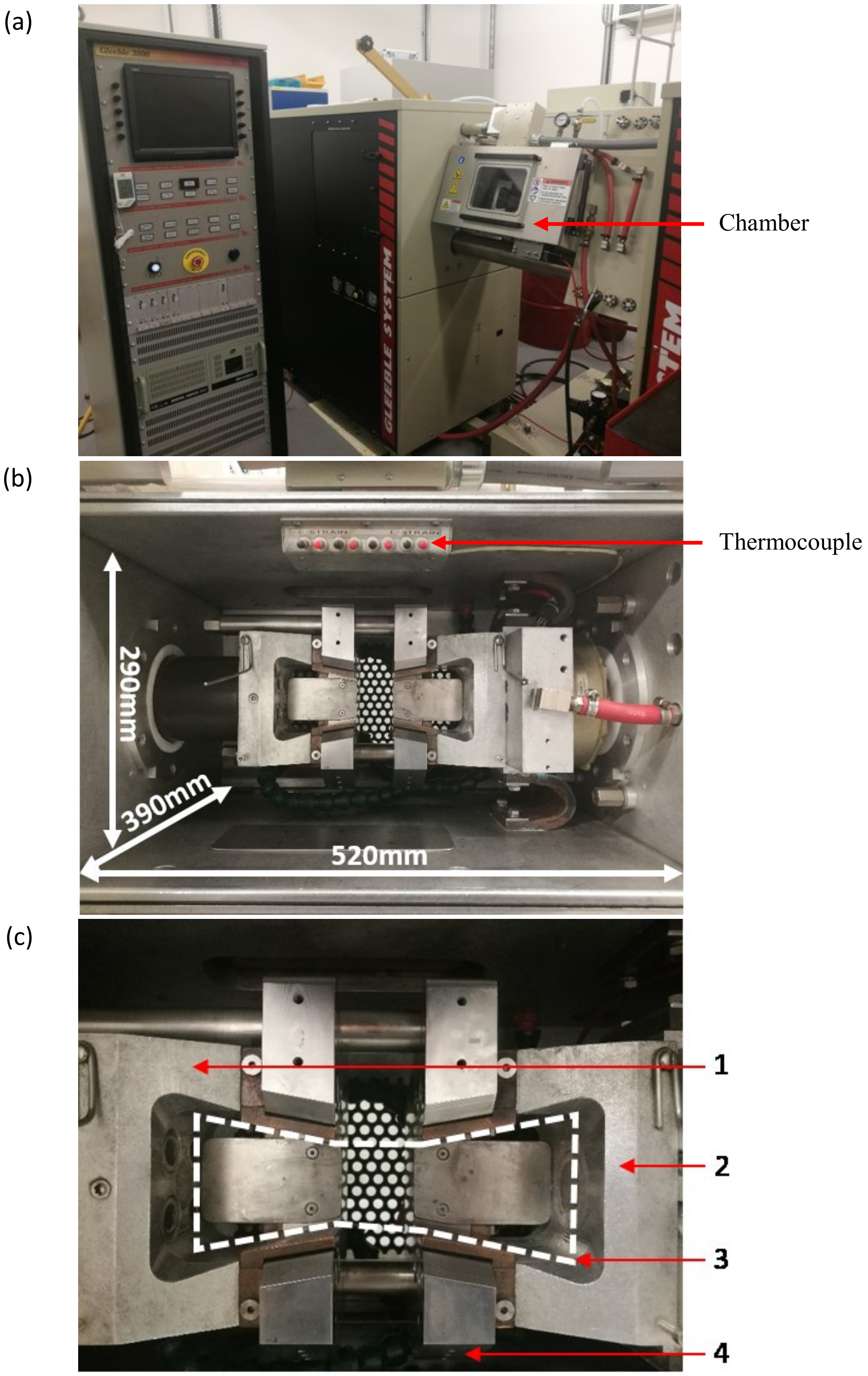

Figure 3.1 (a) Gleeble thermal-mechanical simulator; (b) Space inside Gleeble chamber; (c) Main parts in Gleeble chamber.

As shown in Figure 3.1(c), the Gleeble 3800 test chamber consists of the left arm (No. 1) and right arm (No. 2) respectively, the left arm moves horizontally towards or away from the right arm applying a compression/tension force respectively against a stationary right arm. Electrical current flows between the two arms through the test piece to heat via electrical resistance heating. There are 3 screw holes at the location of point 4, in which the hot stamping simulator is secured. The hot stamping simulator occupies the region shown as No. 3. Thermocouple wires are attached to the Gleeble 3800 as shown in Figure 3.1(b), which provide feedback control and data logging.

The Gleeble 3800 was chosen for this study for 5 main reasons (Dynamic Systems Inc., 2015). Firstly, the Gleeble provides a fast heating rate up 10,000˚C/s using electrical resistance heating, and a high cooling rate with air or water quench system which could be 1,000˚C/s maximum for AA7075 2 mm blanks. Secondly, the test procedures are programmed and controlled by a connected computer using software QuickSim 2, giving the possibility of programming very complex processes with any reasonable change of arm moving speed, load, and temperature, to simulate the real production process accurately. Thirdly, a high compressive force up to 20 tons is available in the Gleeble, which can provide a high pressure on small test pieces to simulate the die closing force in hot stamping process. Fourthly, the Gleeble collects data from thermocouples, transducers, load cells and a laser extensometer for both thermal and mechanical control, improving the control accuracy during the tests. Lastly, the feedback signal delay is small, and acquisition occurs at a high rate, so the control system can adjust electrical current and force rapidly for accurate process control. However, the heating process in Gleeble requires good contact between workpiece and two anvils (dies), it is not possible to heat the workpiece away from dies, thus the new test rig Hot Stamping Simulator was designed to heat the workpiece independently.

3.3 Design

The hot stamping simulator underwent a major revision during testing, and therefore there are 2 main versions which are described in this section. The second (improved) version of the hot stamping simulator was developed after significant experience with the first version, to address deficiencies in stability and ease of use. All the IHTC test results presented in this thesis were generated using the second version of hot stamping simulator.

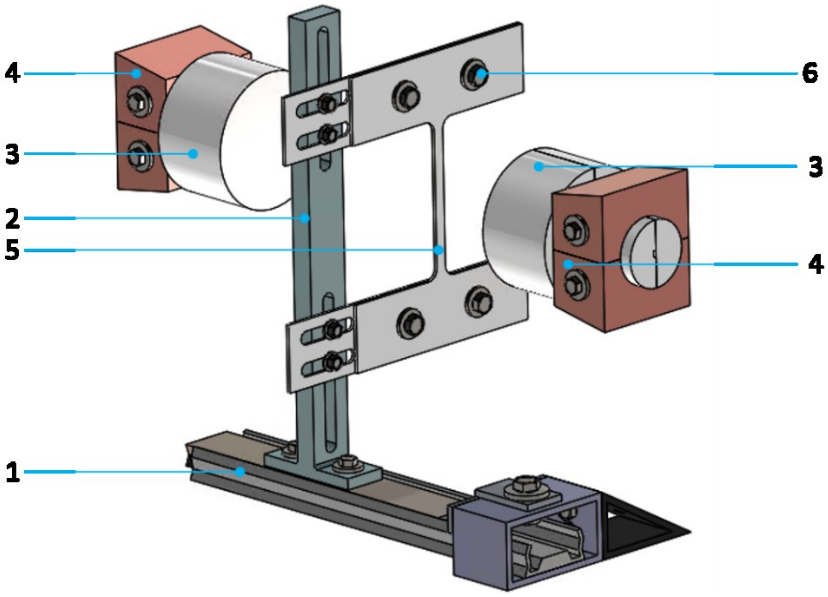

1. Slider
2. Workpiece support
3. Left and right dies
4. Left and right grips
5. Workpiece
6. Screw holes to fasten copper cables

Figure 3.2 Original version of hot stamping simulator[2].

The original version of hot stamping simulator is shown in Figure 3.2, which has 4 main components: a slider (1), a workpiece support (2), left and right dies (3), and left and right grips (4). The slider (1) is divided into the inner part and outer part, where the inner part can move uniaxially along the outer part. This slider supports and fixes the simulator, and is fixed to the screw holes at point 4 of the Gleeble chamber (Figure 3.1(c)). The workpiece support (2) consists of 3 components: central rod, upper workpiece holder and lower workpiece holder. The central rod is fixed onto and moving together with the inner part of slider. The two workpiece holders are attached to the central rod using isolating screws and washers to prevent the electric current from flowing through the central rod. There are two holes on each workpiece holder, which are used to position the workpiece and copper cables to conduct electrical current to it. The left and right dies (3) simulate the punch and die in the hot stamping process respectively, applying die closing speed and die closing force, and these two parts can be replaced using alternate dies made from different materials. The grips (4) are fixed in the Gleeble chamber and hold the dies by applying the die closing force. In addition, the grips connect to the workpiece holders via copper cables fastened to the screw

---

[2] The original design is reproduced from published paper “Ji K., El Fakir O. E., Gao H., Wang L. (2015). Determination of Heat Transfer Coefficient for Hot Stamping Process. Materials Today: Proceedings, 2, S434-S439.”

holes at point 6 in Figure 3.2 to transfer the electrical current from the grips to the workpiece holders. The part 5 shown in Figure 3.2 is the aluminium blank workpiece and is compressed by the two dies.

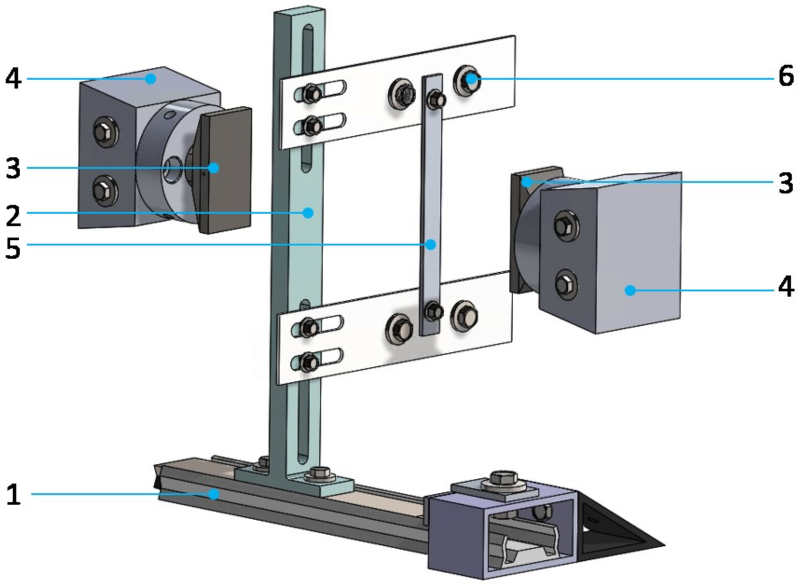

1. Slider
2. Workpiece support
3. Left and right dies
4. Left and right grips
5. Workpiece
6. Screw holes to fasten copper cables

Figure 3.3 *The improved version of hot stamping simulator*[3].

The improved hot stamping simulator design is shown in Figure 3.3. The designs of slider, support and cables remain same as the original version, while the workpiece, grips and die/punch are improved. The detailed design of original hot stamping simulator and improvements for the new version are described in the following sections.

3.3.1 Workpiece

The workpiece simulating an aluminium alloy blank is pressed by the die and punch, and held in place by two workpiece holders. There were 4 design requirements for the workpiece. Firstly, the functional area of the workpiece, which is pressed by dies, needs to be heated uniformly. Secondly, the workpiece is held and positioned by workpiece holders, thus the design must accommodate a holding area. Thirdly, the workpiece is heated via electrical resistance heating, thus the contact between the power delivery cables and the workpiece

---

[3] The improved design is reproduced from published paper “Ji K., Liu X., EL Fakir O., Liu J., Zhang Q., Wang L. (2016). Determination of the Interfacial Heat Transfer Coefficient in the Hot Stamping of AA7075. Manufacturing Rev., 3, 16.”

needs to be of low electrical resistance. Finally, the temperature at the centre point of the functional area should be monitored with k type thermocouples.

For the purpose of heating the workpiece functional area uniformly, the most applicable heating method controlled by the Gleeble 3800 testing machine is Ohmic heating. Unlike heating through heat transfer in gas furnaces, it follows Joule's law, which enables the heating to be precisely controlled:

$$Q = I^2rt = V^2t/r \tag{3.1}$$

where Q is thermal energy (J), I is current flow (A), r is electrical resistance (Ω), t is time (s) and V is voltage (V). Accordingly, if the current flow is the same at each area of workpiece, the thermal energy changes with the electrical resistance, which is calculated as follows:

$$r = \rho L/a \tag{3.2}$$

where ρ is electrical resistivity (Ω·m), L is length and a is cross sectional area. When the length equals 1, the formula is reduced to Equation (3.3), indicating the electrical resistance per unit length.

$$r = \rho/a \tag{3.3}$$

Combining Equations (3.1) and (3.3), the thermal energy per unit length generated through current is described as:

$$Q = I^2\, \rho t/a \tag{3.4}$$

In Equation (3.4), current flow and electrical resistivity remain the same at each area of the workpiece, and the electrical resistivity is a temperature dependent material constant, thus the only variable factor is the cross-sectional area. Therefore, the functional area of the workpiece is designed as a rectangular-shape to keep the same width throughout the workpiece.

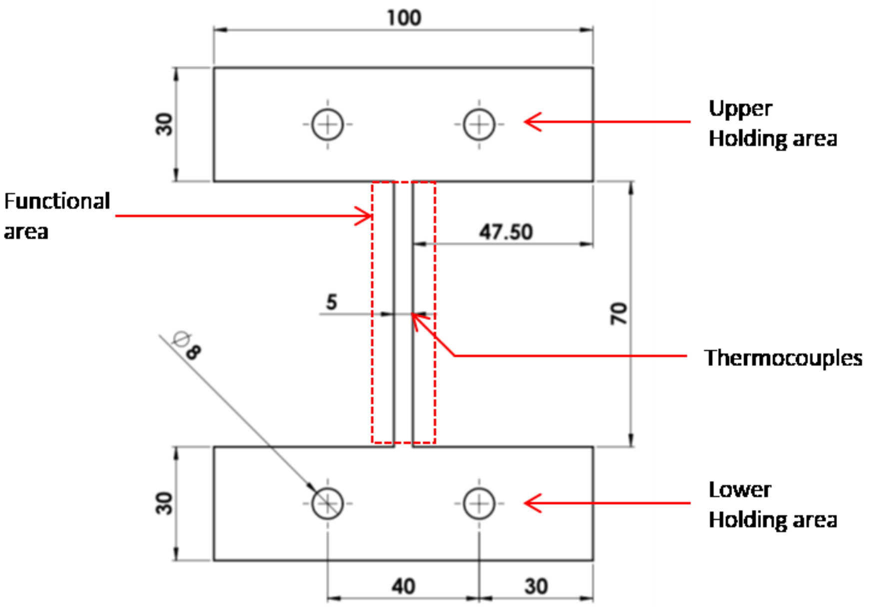

Figure 3.4 Original version of workpiece (mm).

The 'I' shape workpiece was designed as shown in Figure 3.4 and consists of 3 areas: functional (central) area, upper and lower holding areas. The functional area is the area of the workpiece which is tested, and it is heated via electrical current before being pressed by two dies. At the centre point of the functional area, as shown in the figure, there is a 1.3 mm hole drilled from the side horizontally into the workpiece, where a pair of K type thermocouples are connected to the thermocouple ports in Figure 3.1(b). The width of the functional area is designed to be 5mm, which reduces the electrical current required for heating and the compressive force needed for stamping to be within the capabilities of the testing machine. The holding areas are designed to be much wider to ensure uniform surface current at the functional area, and to reduce the resistance of that area, minimising heat generated through electrical current. There are two holes in each holding area, through which the workpiece is fixed to the workpiece holders using M8 screws for positioning. Cables connected to grips with ring terminals are tightly fixed to the screw holes to transfer the electrical current.

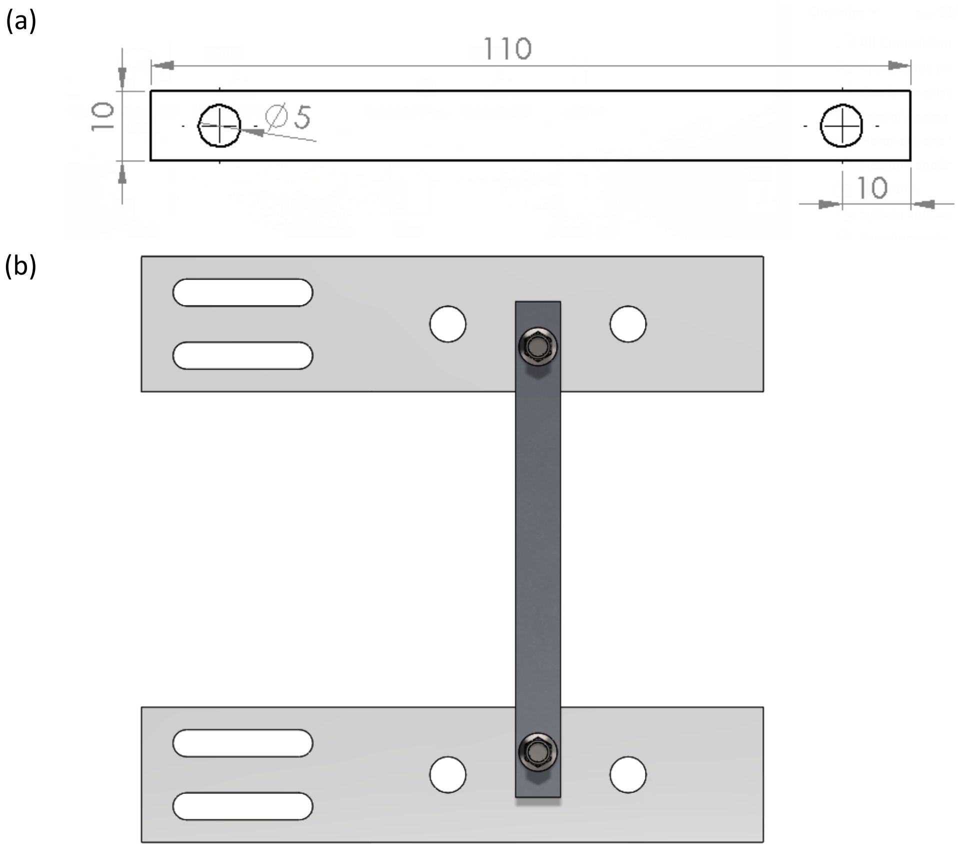

Figure 3.5 Improved version of: (a) workpiece; (b) workpiece with workpiece holders.

In the second revision, the workpiece was simplified in order to reduce manufacturing material waste as well as difficulty of production. The improved version of the workpiece was simplified into strip shape with a screw hole at each end of the strip as shown in Figure 3.5(a). A screw hole was therefore added to the middle of the two holes on each workpiece holder in order to fix and position the workpiece using screws. As shown in Figure 3.5(b), the electric current flows through the copper cables attached to two holes on the workpiece holders retained from the original design, and then flows through the workpiece. Experimental tests with the original version revealed that the workpiece was highly likely to fracture under high pressure compressions due to its low strength at elevated temperature, and therefore the width was extended from the original 5 mm. However, with a larger workpiece width, it requires higher electric current flow to achieve the same heating rate requiring thicker heating cables. The thickest heating cables could be fitted in the Gleeble chamber with reasonable stiffness could support 10 mm maximum workpiece to achieve 200°C/s heating rate, therefore the workpiece is extended to 10 mm width.

3.3.2 Workpiece support

The workpiece support simultaneously supports and positions the workpiece, and transfers the electrical current to the workpiece for heating. The workpiece support is divided into 3 components: a central rod, upper and lower workpiece holders.

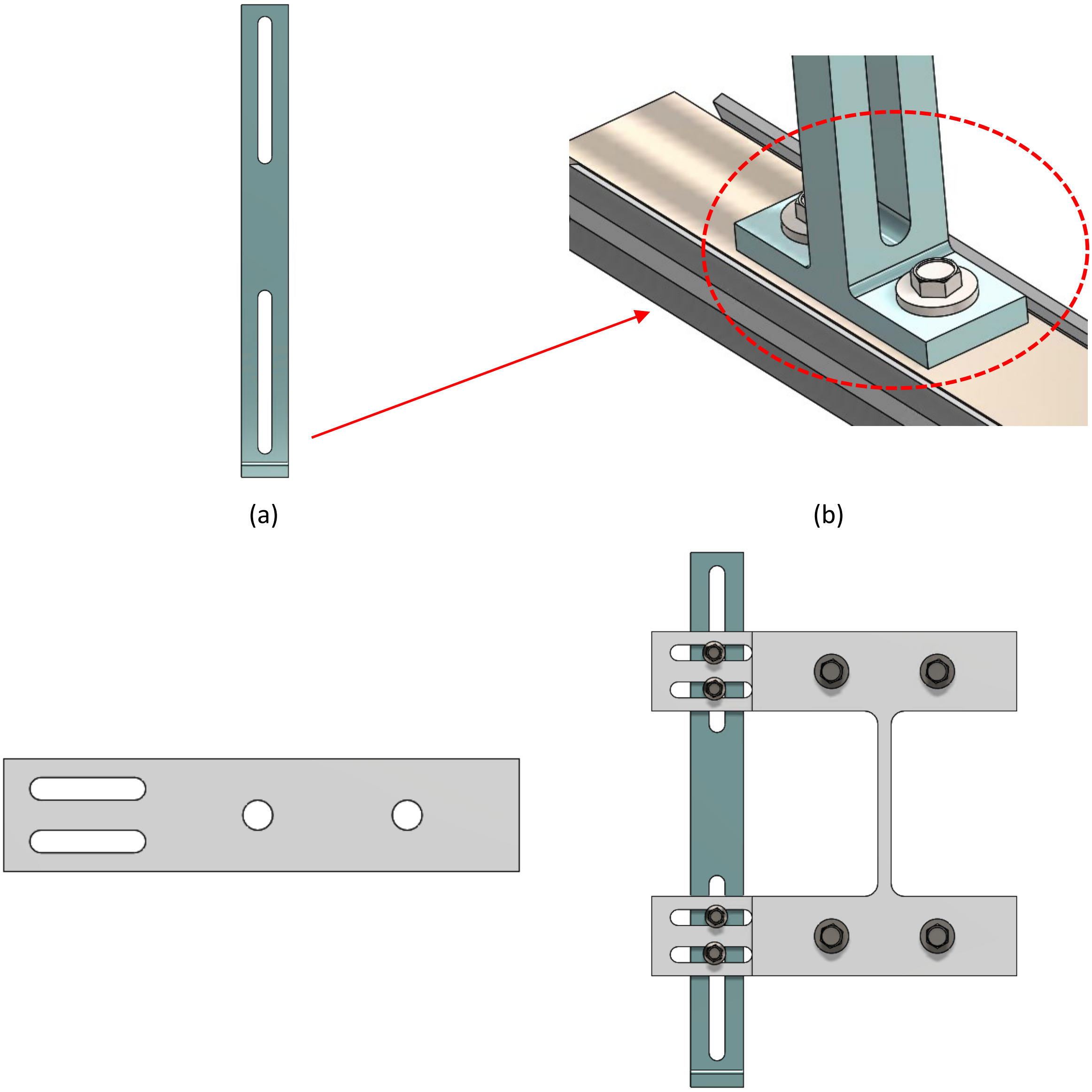

(a) (b)

(c) (d)

Figure 3.6 Original version of workpiece support: (a) central rod (b) T shape bottom (c) workpiece holders (d) assembled.

The central rod is made of aluminium alloy (AA7075), as shown in Figure 3.6(a). The base is a ‘T’ shape as shown in Figure 3.6(b), and is fixed to the drawer member of the slider through two holes and can thus move together with the drawer member uniaxially along the cabinet member of the slider. There are two slots through the rod to attach the workpiece holders with M5 plastic/ceramic screws and washers, which electrically isolate the workpiece holders. The workpiece holders can be moved vertically along the central rod by adjusting the position of the screws through the two slots. This allows adjustment of the position of the workpiece. The workpiece support was unchanged in the improved hot stamping simulator.

The workpiece holders shown in Figure 3.6(c) are made of mild steel. The two slots at one end of the holder are for M5 screws used to fix it to the central rod, where plastic M5 screws are used to fix them with plastic washers in between the holders and central rod to electrically insulate the rod. The reason for slots instead of screw holes is to allow adjustment of the functional area of workpiece against the centre of the dies to balance the compressive force. The two large holes are M8 holes to hold the workpiece and ring terminals of copper cables. M8 screws go through the components in order of ring terminal, workpiece, workpiece holder, and tightened by nuts to make sure that there is good electrical contact. Figure 3.6(d) shows the assembled workpiece support with the workpiece.

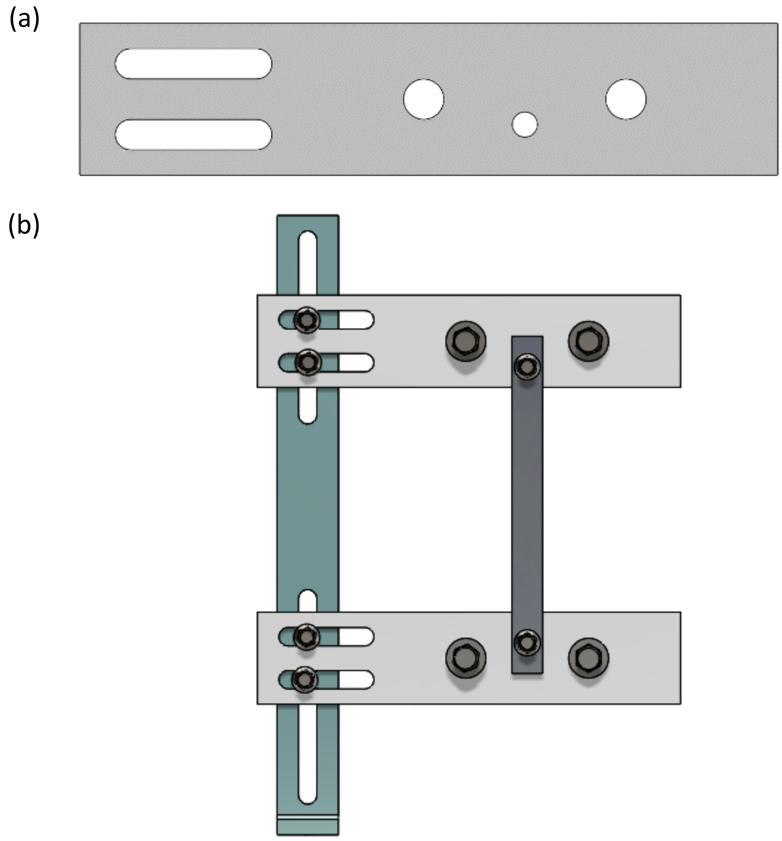

Figure 3.7 *Improved verision of workpiece support: (a) workpiece holders; (b) assembled with workpiece.*

As shown in Figure 3.7(a), the shape and all screw holes in the original design of workpiece holders remained the same in the new design. However, since the shape of workpiece was changed, a new hole was added to the middle of the holders to attach the workpiece between the two holes used to fix the copper cables. The cables remain attached to the two original holes and the electric current flows through the simulator in the order of: grips, cables, workpiece holder, workpiece, workpiece holder and cables on the other side. The assembled improved version of the workpiece support and workpiece is shown in Figure 3.7(b).

3.3.3 Slider

The slider is designed to hold the workpiece support, workpiece holders and the workpiece, and position them to ensure that the dies press onto the workpiece accurately. As shown in Figure 3.8(a), the slider was combined by the sliding parts and connecting parts. The sliding parts were used to hold the workpiece support and provided the ability of uniaxial movement, while the connecting parts were used to fix and position the slider and all other components on to the Gleeble chamber.

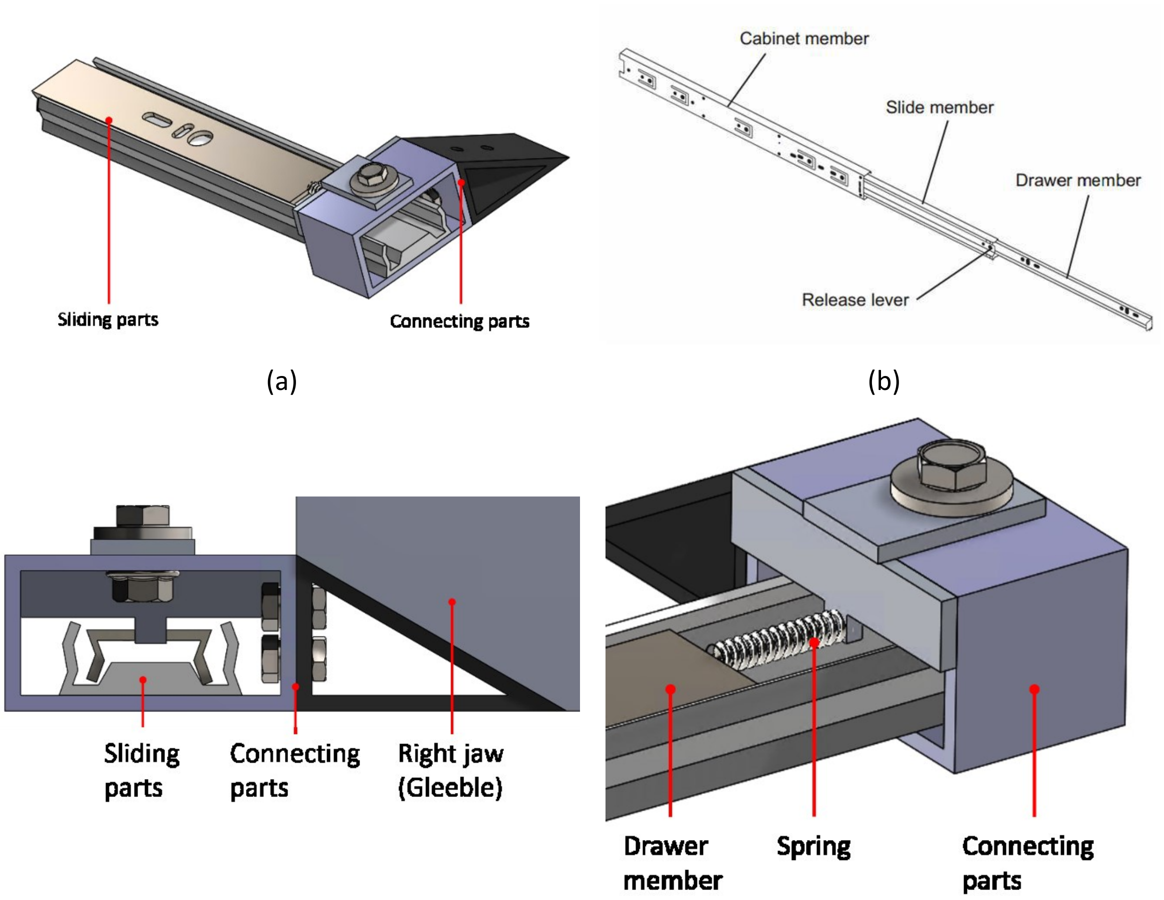

(a) (b) (c) (d)

Figure 3.8 *Slider: (a) full; (b) sliding parts; (c) connecting parts connected to Gleeble; (d) spring between drawer member and connecting parts.*

To reduce cost and manufacturing time, the sliding part was repurposed from a commercial drawer slider rail, as shown in Figure 3.8(b), and consisted of 3 primary members: drawer member, slide member and cabinet member. The 135 mm drawer member and slide member can move uniaxially along a 200 mm length. The full extension length of the slider is 600mm, which was larger than the free space for punch movement providing ample sliding space for workpiece movement.

The fixed end of the cabinet member was fixed to the right arm in the Gleeble chamber using a slider holder as shown in Figure 3.8(c). Holes were drilled through the drawer member to fix and position the central rod of the workpiece support using screws, thus providing further support and positioning of the workpiece. Between the slider holder and the drawer member of the slider, there is a 20 mm length spring and a spring stopper to position the drawer member (Figure 3.8(d)), and its function is to ensure that the punch: (i) does not press on the workpiece or (ii) pushes the slide member and keeps the workpiece away from the two dies when completing the forming and quenching stages. This ensures that the workpiece is isolated both thermally and electrically from the dies during heating or air cooling processes.

The improved version of the slider did not change significantly from the original version, with the main change being the slider holder. The slider holder was also modified in the revised version to allow more accessibility for manipulation of the hot stamping simulator.

3.3.4 Punch and die (Anvils)

Left and right anvils were designed to simulate the punch and the die in a hot stamping process. The left anvil shown in Figure 3.9(a) was fixed to the left arm and moves together with it, simulating the moving punch. It is machined from a single piece of tool steel and consists of two cylinders, of diameter of 60 mm and 30mm. The front area contacts and presses the workpiece, and the back cylinder is held by grips to fix it to the arm. The right anvil is fixed to the right arm in Gleeble chamber, which is non-moveable, simulating the non-moveable die. It is outwardly the same as the left die, however it is divided in half to accommodate a 5 mm by 1 mm slot near its front surface for the welding of thermocouples to monitor the die temperature evolution, as shown in Figure 3.9(b). There are up to 3 pairs of thermocouples welded on the slot, and the right anvils with thermocouples are shown in Figure 3.9(c). Dies can be easily replaced by other die sets made of different materials, simulating different punch and die materials.

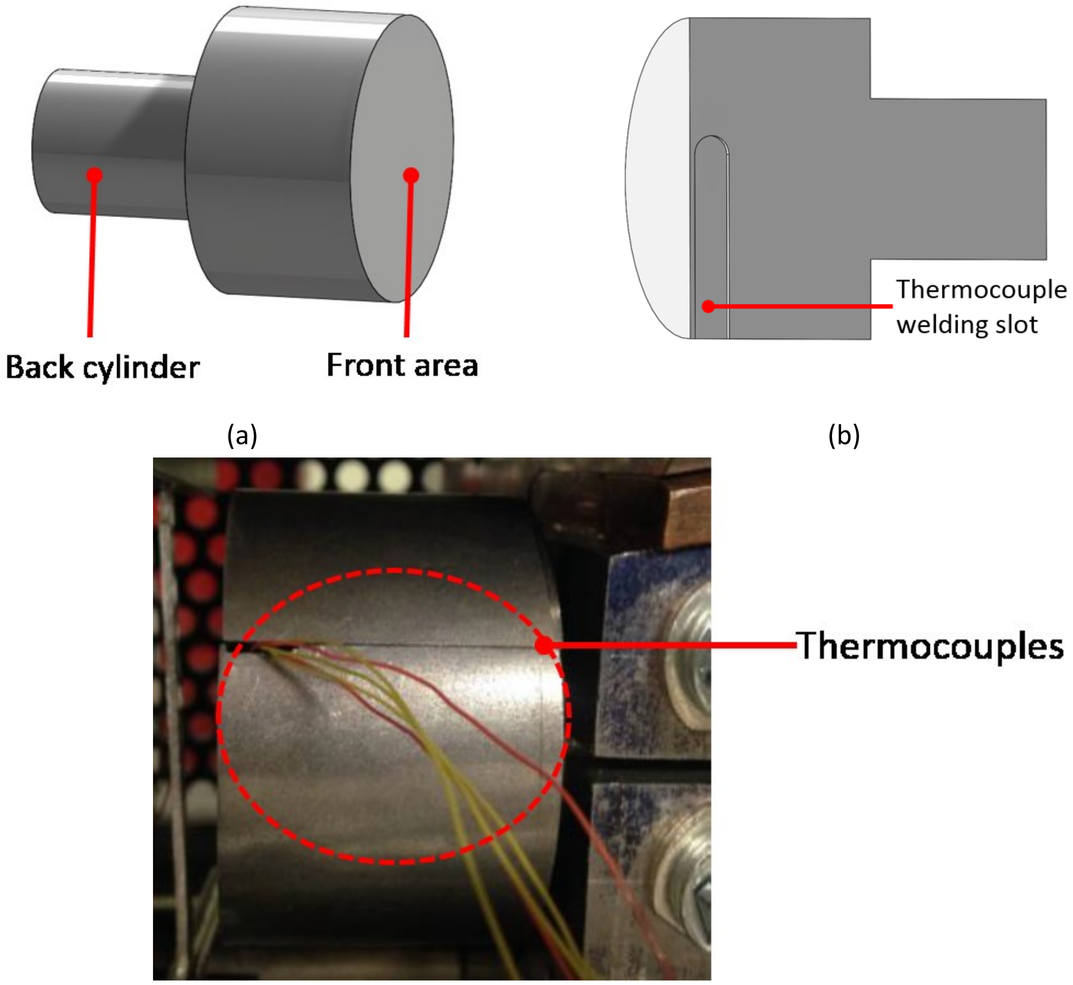

(a) (b)

(c)

Figure 3.9 Punch and die (original version).

Three main drawbacks were observed from test experience using the original version of die and punch. On one hand, in the original version, the thermocouples were welded onto the slot of the right anvil, but the position accuracy of the welding point was low. On the other hand, as the die was divided into two halves, there was difficulty in alignment of the contact surfaces for even contact with the specimen. To solve these problems, the improved punch and die were changed to rectangular shape, as shown in Figure 3.10. The punch and die in the improved version were both designed as whole parts instead of two divided parts. The contact area between the workpiece and punch/die are 50 x 10 = 500 mm^2. To ensure parallel contact with the workpiece, 3 of 25 x 50 mm^2 flats were thus cut on the edge of the cylinder holder part which were at 120°, and were fixed by screws to ensure the parallelism between die long edge and workpiece long edge. A larger contact area would lead to a larger stamping force to achieve the same contact pressure, and the maximum stable stamping force with high stamping speed was 10 kN according to test experience, therefore the dimensions of the improved dies were decided. This ensured consistent contact area between tests, and even application of load onto the workpiece. Instead of cutting the die into two parts, a 1.3 mm diameter hole was drilled from side surface into the die parallel to the contact surface for thermocouples, ending at the centre point. The centre point of the hole was 2 mm away from the contact surface. Thermocouples were secured inside the hole by an interference fit.

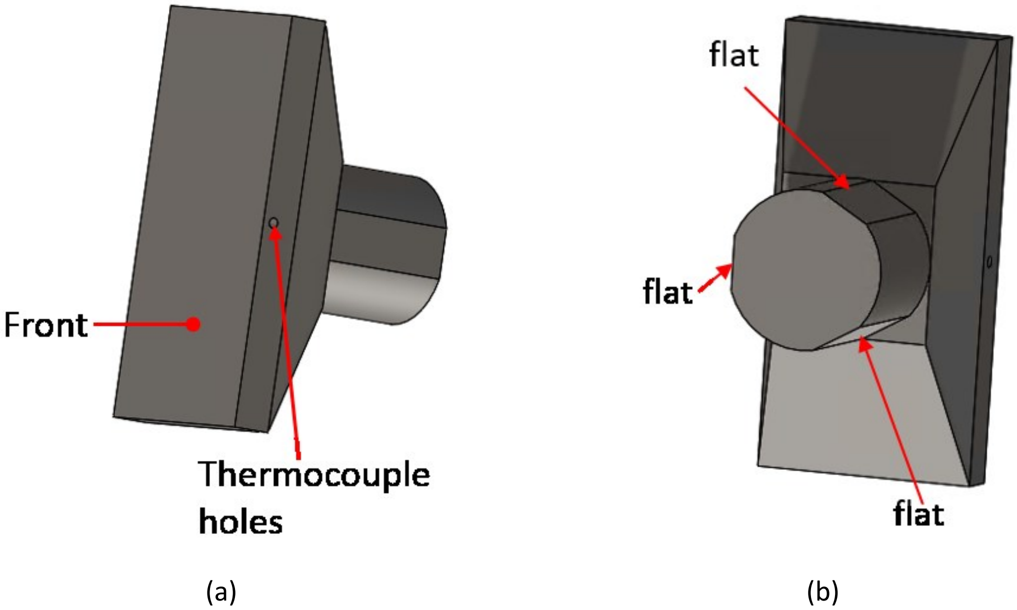

Figure 3.10 Punch and die (improved version): (a) front; (b) back.

3.3.5 Grips

Grips were designed to hold the dies and fix them to the arms in the Gleeble chamber, and transfer electrical current to heat the workpiece. The grips were identical for both sides, and were divided into halves. One of the two halves is shown in Figure 3.11(a), in which the curved surface A shares the same diameter as the smaller cylinder of the punch/die to hold them. The assembled grips and punch/die are shown in Figure 3.11(b), showing how the grips hold the dies. The M8 screw hole into surface B is used to fix the ring terminal of a copper cable connected to workpiece holder and holding area of workpiece. The slope of surface C has the same slope of the inside surface of the arm, for good contact. Surface D is the back surface pushed by the fixing tools shown in Figure 3.11(c). When the tools push the grips outwards, the contact between surface C and the inner surface of the arm is tight, to apply enough holding force to dies and give good surface contact for electrical current.

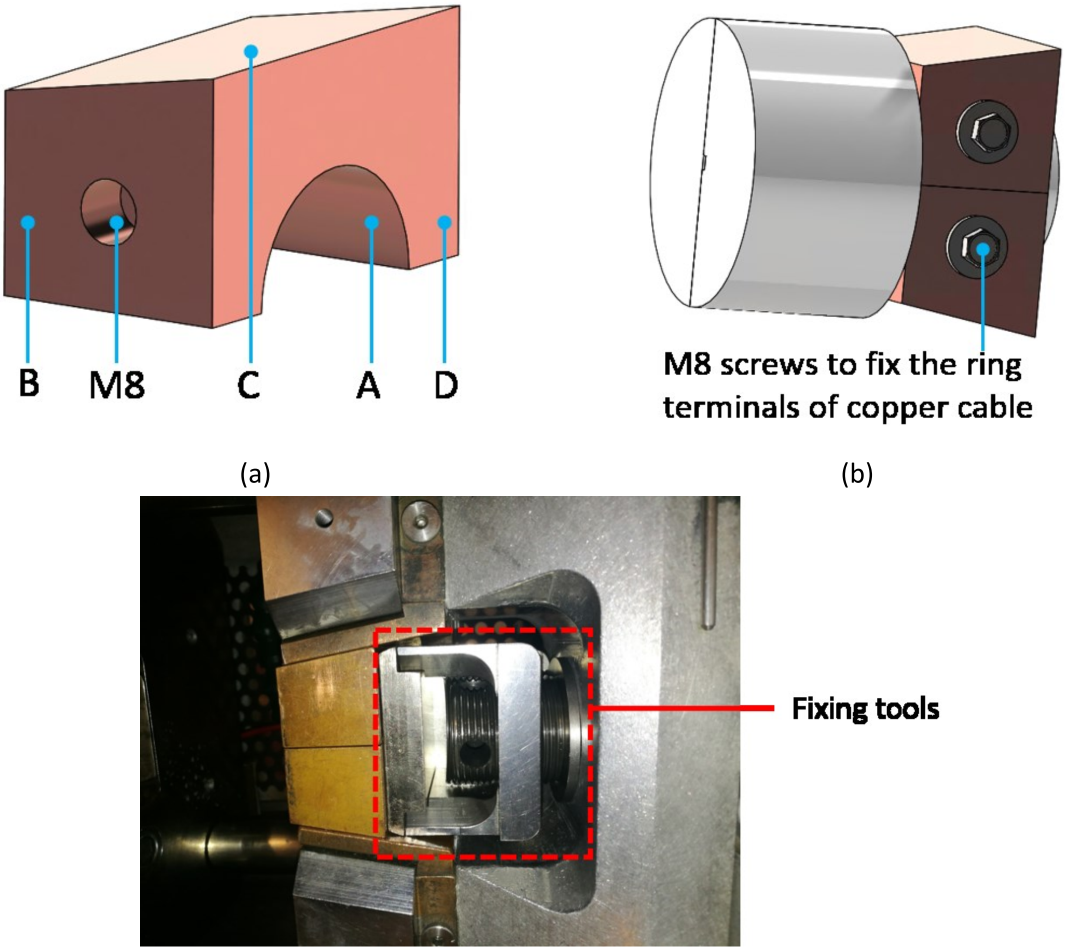

(a) (b)

(c)

Figure 3.11 Grips (original version): (a) half grip; (b) grips holding die and connecting to cables; (c) fixing tools.

New grips were designed as shown in Figure 3.12, and are divided into two parts: bottom and ring. The bottom is a single piece with 2 sets of screw holes, one of which is M8 on surface B’ for the ring terminals of copper cables, and the other set is to fix the ring part. The surface A’ of the bottom parallel to surface D’ is designed to support the die/punch, and the surface C’ fits the inner surfaces of the Gleeble jaws. The screw holes on surface A’ are used to fix the ring part as shown in Figure 3.12(b). The assembled ring and bottom is shown in Figure 3.12(c), while the one with die/punch is shown in Figure 3.12(d).

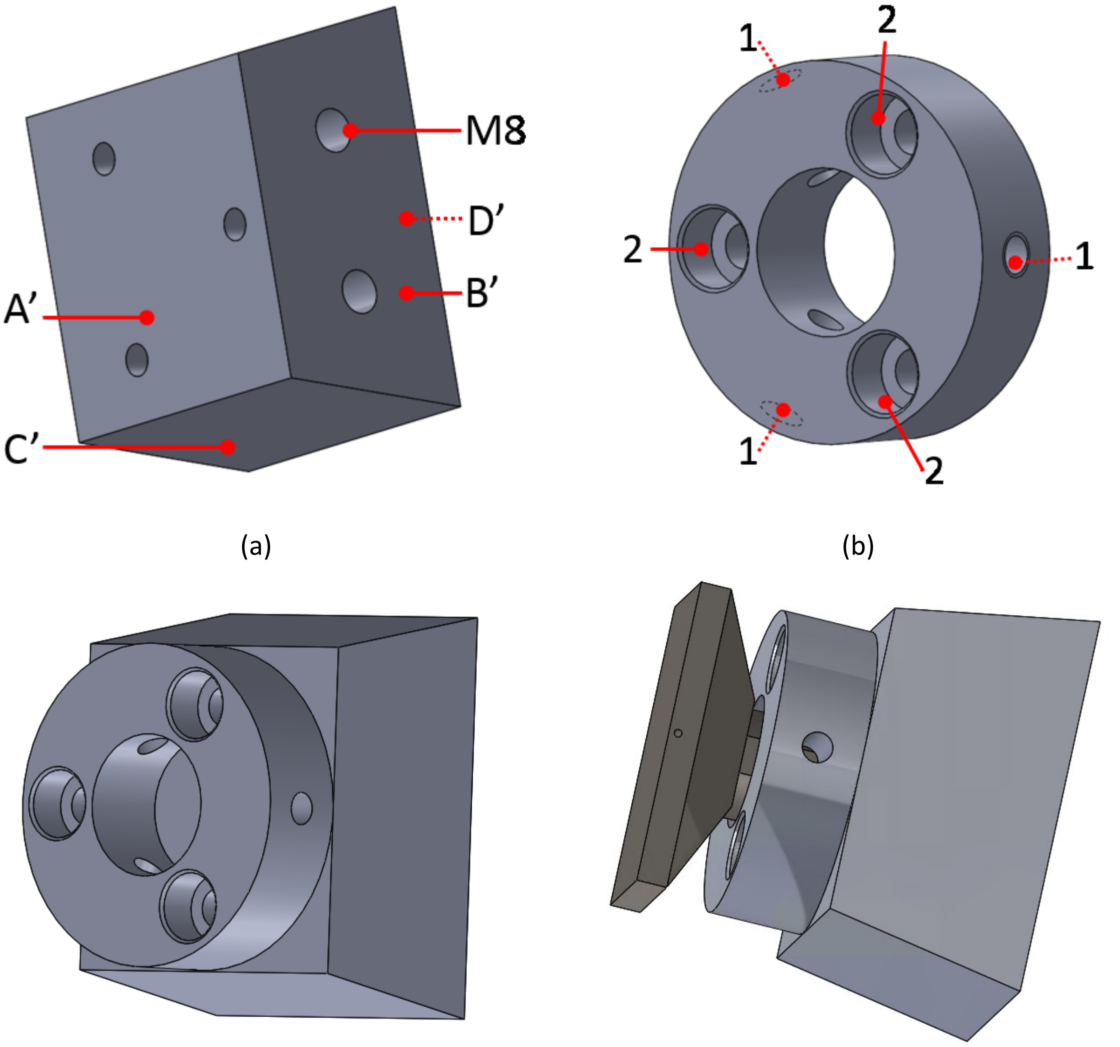

(a) (b)

(c) (d)

Figure 3.12 Grips (improved version): (a) bottom; (b) ring; (c) assembled grip; (d) assembled grip with die.

3.4 Assembly

Shown as point 4 Figure 3.1(c), there is a surface with 3 M5 screws holes near the bottom of the right arm in Gleeble chamber, which is 30 degrees to its bottom surface and 60 degrees to its front surface. The slider holder mentioned above is fixed to this surface via screws.

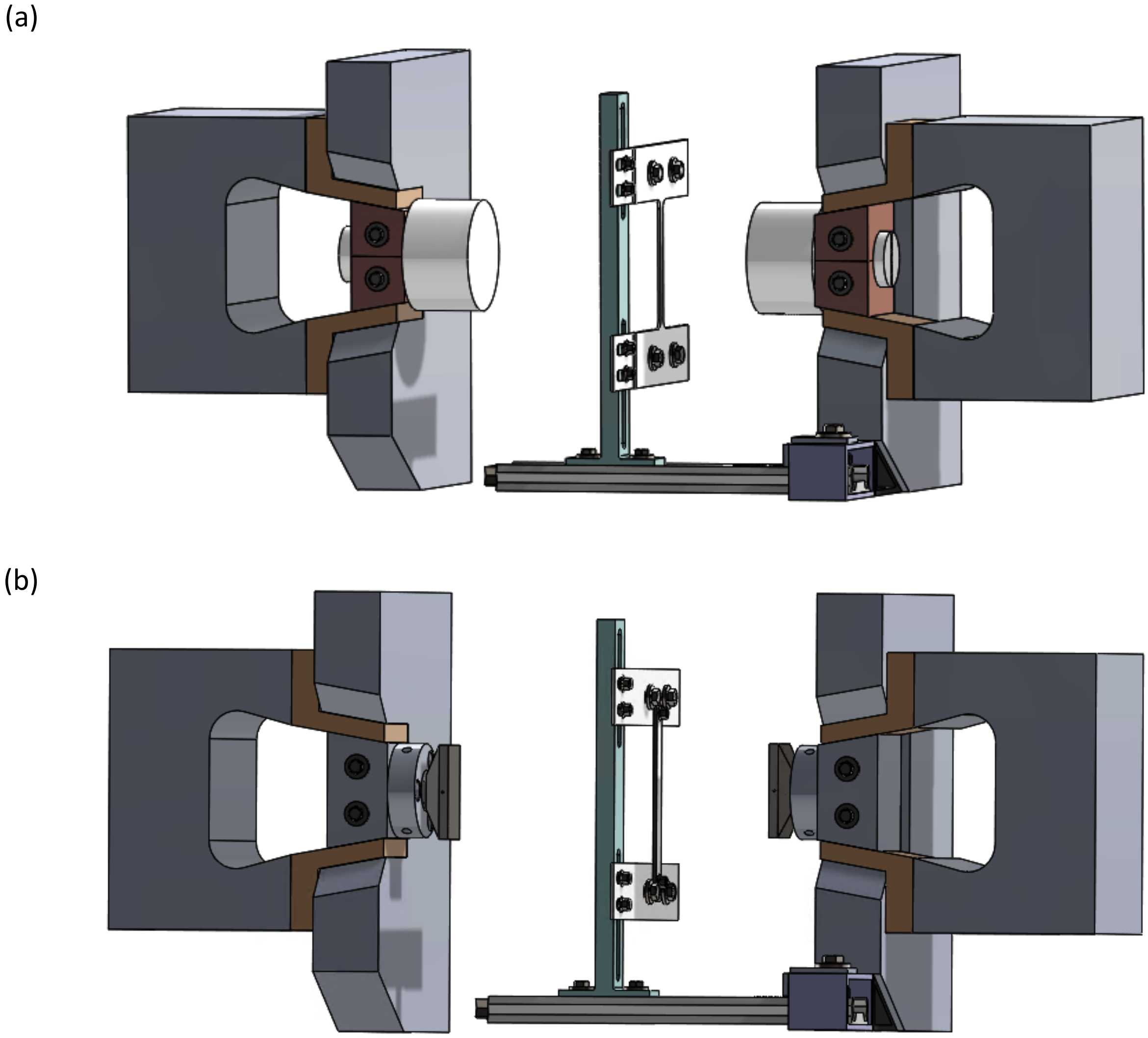

Figure 3.13 Assembled hot stamping simulator (a) original version (b) improved version.

The central rod is fixed to the drawer member of the slider as shown in Figure 3.6(b), perpendicular to the slider and the bottom plane of the Gleeble chamber, and parallel to the front surface of the arms. The workpiece holders are attached to the central rod using plastic M5 screws through the slots in central rod, and there are two plastic washers between workpiece holder and central rod with each screw to electrically isolate the central rod. Distance of the workpiece holders from the top of central rod are adjusted according to the position of workpiece, to guarantee that the central point of the workpiece is in same line with the central points of the two dies. The workpiece is secured to workpiece holders by M8 screws and nuts, together with copper cables through their ring terminals for electric current. In the improved version, the workpiece was changed to a rectangular shape, and the screws through the ring terminals and workpiece holders do not penetrate the workpiece.

The die and the punch are held by two half grips, and when the grips are pushed outwards from the arms, both contacts between die-grip and between grip-arm are compressed and tightened, to avoid poor connection in circuit. Electric current flows through the whole simulator in the order of: right arm, right grips, cables connected to upper holder, upper workpiece holder, workpiece, lower workpiece holder and cables connected to it, left grips and finally the left arm. In the improved version of the hot stamping simulator, the two grip halves are a single part as the bottom and the ring terminals are fixed to it.

Thermocouples are inserted to a two-channel ceramic tube and plugged into the 1.3 mm hole to the centre of functional area of the workpiece, and the other end of thermocouples is plugged into the thermocouple readers in Gleeble chamber, monitoring the temperature evolution of the workpiece. Thermocouples are pre-welded to the slots of right dies 2 mm away from the contacting surface with workpiece, linked to the thermocouple readers as well, monitoring the temperature of central point 2 mm under the contact surface. The method of plugging thermocouples into workpiece remain the same in the improved version, however the method of monitoring the temperature evolutions of punch and die was changed. As shown in Figure 3.10, there is a 1.3 mm diameter hole on the side surface of die/punch, thus the same method for workpiece was applied for die/punch, i.e. thermocouples inserted into a two-way ceramic tube before being plugged into the hole on punch/die.

The original and improved assembled simulators are shown in Figure 3.13(a) and (b) respectively. Temperature evolutions of workpiece and right die are monitored and recorded via thermocouples. During the stamping process, the workpiece is pushed by the moveable left die towards the non-moveable right die, and compressed between these two dies. The heating rate, stamping temperature, die closing speed, die closing force and die closing time are all pre-programmed and adjustable in the software QuickSim 2, and the order and circle number of processes are adjustable using the software.

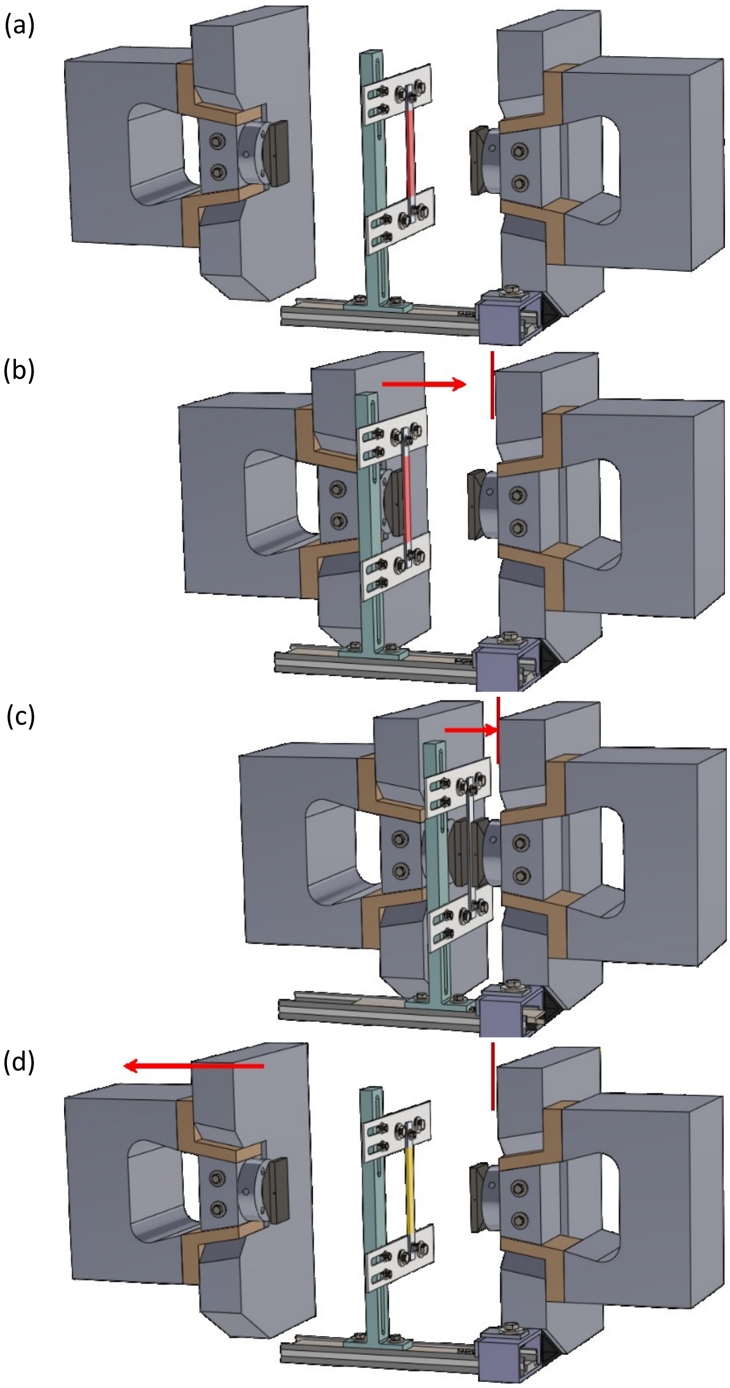

Figure 3.14 Operations to simulate FAST process: (a) heating; (b) punch pushing workpiece towards die; (c) stamping and quenching under constant pressure; (d) punch moving back, spring pushing workpiece back, incubating (artificial ageing).

The operations to simulate FAST process using Hot stamping simulator is shown in Figure 3.14. The workpiece is heated to forming temperature first, before it is pushed towards to the die by punch (left die). A pre-defined contact pressure is applied to the workpiece after the dies being fully closed for stamping and quenching. Afterwards, the left die moves back to its initial position while the workpiece is pushed back from the right die with drawer member of the slider (Figure 3.8(d)) by the spring at the right end of slider. The workpiece is reheated for artificial ageing if applicable.

3.5 Conclusion

A hot stamping simulator was successfully developed and manufactured to work in conjunction with the Gleeble 3800 thermo-mechanical testing machine. The original version was designed and made, and underwent a major revision during testing, resulting in the second version with better stability and ease of use. The simulator has 4 main components: a slider, a workpiece support, left and right dies, and left and right grips. The Hot stamping simulator enables high heating rate up to 200°C/s, high stamping speed up to 1000 mm/s, high die closing pressure exceeding 20 MPa, reversibly moveable, high control accuracy, convenience of changing punch/die and workpiece, ease of applying and cleaning lubricant, and high complexity of temperature, stroke moving and force evolution. The hot stamping simulator is not only suitable for FAST tests in Chapters 5 and 6, but also available for simulating other types of stamping processes. In addition, the hot stamping simulator is also used in the IHTC tests in Chapter 4, providing high flexibility of temperature, contact pressure settings and easy access to change die and apply lubricant.

Chapter 4

Interfacial heat transfer coefficient

4.1 Introduction

This chapter is related to publications[4]. As reviewed in Chapter 2, the post form strength of components formed from high strength and ultra-high strength aluminium alloys are highly sensitive to quenching rate during the hot stamping process (Milkereit et al., 2009). Thus, in order to retain the highest possible mechanical strength after forming and post-form processes, the critical quenching rate must be achieved in order to prevent the formation of coarse or weak precipitates. As a result, the interfacial heat transfer coefficient (IHTC) is extremely important for producing high strength components with FAST process, as well as to optimise forming parameters to maximise productivity. Furthermore, an accurate value of the IHTC can also benefit tool designers enabling more accurate prediction of quenching, hence avoiding insufficient quenching in areas such as sharp corners.

In the present research, the IHTC value was obtained by correlating the simulated data generated from the FE commercial simulation software PAM-STAMP to experimental temperature evolutions. The Hot Stamping Simulator was utilised to measure temperature evolutions of both specimens and die/punch under different forming conditions to identify IHTC values under different die closing pressures and lubrication conditions. As a result, an IHTC model was developed as a function of contact pressure, tool material and lubricant for AA7075 specimens, which was verified by hot stamping hemispherical dome tests and tests to form an automotive B-pillar component.

---

[4] Chapter 4 is reproduced from paper works "Ji, K., Liu, X., EL Fakir, O., Liu, J., Zhang, Q., Wang, L. (2016). Determination of the Interfacial Heat Transfer Coefficient in the Hot Stamping of AA7075. Manufacturing Rev., 3, 16." and "Liu, X., Ji, K., El Fakir, O. E., Fang, H., Gharbi, M. M., Wang, L. (2017). Determination of the interfacial heat transfer coefficient for a hot aluminium stamping process. Journal of Materials Processing Technology, 247, 158-170."

4.2 Test procedure

4.2.1 Experiments

As described in Chapter 3, the Hot Stamping Simulator was clamped and supported by two jaws in the Gleeble chamber, where the left jaw was movable horizontally and the right jaw was fixed. An AA7075 specimen cut from 2 mm thick blank into 110 x 10 mm (Figure 3.5(a)) shape with an average roughness of 340nm was assembled and tightly screw fixed onto blankholders and positioned between the die and punch. The roughness values were determined by arithmetical mean deviation (Ra) using a Veeco Wyko NT9100 tester. Thermocouples connected to Gleeble data logger were embedded to the centre point of the specimen, and at a distance of 3 mm away from the centre of die/punch contact surface, for one pair each. The temperature evolutions of specimen and die/punch were monitored by the data logger and exported to the computer connected to Gleeble.

Prior to each test, the punch in the left jaw was manually positioned so that the punch, specimen, and die were in full contact (i.e. a very small compression force value 0.1-0.2 kN was applied to the specimen). At this starting position, the stroke reading was recorded and considered to be zero stroke position. The punch was then moved backwards by 20mm, giving enough space for the specimen to be heated, thermally isolated from both punch and die. The position of the specimen was determined by the position of the insulating block supporting the blankholders, and it was checked ensuring that the specimen did not contact either the punch or the die to prevent it from short circuiting during the electrical resistance heating stage.

To simulate the temperature evolution of hot stamping processes under the unlubricated (dry) condition, the specimen was heated to its SHT temperature of 490°C at a constant heating rate of 10°C/s, followed by 10s soaking at that temperature to generate an even temperature distribution and to avoid any overshoot. When the soaking ended, the punch driven by left jaw was moved towards the die at a speed of 400 mm/s, while the die and punch remained unheated at room temperature. Immediately after the specimen contacted both punch and die, it was compressed under a constant pre-programmed contact pressure for a period of 20 seconds ensuring that the specimen was quenched to room temperature before the punch moved back to its initial position. Different pressures were applied for each test, in order to study the effect of contact pressure, or so-called die closing force, on the IHTC value. Stroke control was selected as mechanics control mode during the movement of the punch/left jaw in the programme, to ensure that the punch speed was accurate, and then the control mode was switched to Force control for compression to deliver a precisely applied force.

The test procedure for lubricated conditions was similar to those for dry conditions. Prior to each test, a precise weight of lubricant (Omega-35) was measured using a highly sensitive scale, and evenly applied onto the contact surfaces of both the punch and the die using a brush. The weights of lubricant in each test were different to study the effect of lubricant layer thickness on heat transfer. A soft brush was used to apply lubricants onto the tool surfaces. The brush was weighed before and after application, to determine the weight applied onto the tools. The lubricants were evenly applied to the contacting surfaces between the workpiece and tool pieces. The amount of lubricant applied to the punch and the die were carefully controlled within 10% tolerance in each test. The lubricant was removed and the tool pieces thoroughly cleaned using wipes with chemical etchant after each test, ensuring there was no residual lubricant affecting the subsequent test.

Different amounts of lubricant have been applied to study the effect of lubricant layer thickness on the IHTC value. The average thicknesses of lubricant applied each time was calculated using the weight, area and density. Tests under both lubricated and dry conditions with different tool materials were also conducted to study the effect of die material on the IHTC value.

Prior to the IHTC tests, two sets of calibration tests were performed to ensure the temperature and force accuracy of the tests. A specimen temperature distribution test was performed first to determine the accuracy of heating and the homogeneity of temperature in the contact area. 3 pairs of thermocouples were embedded into the specimen: one pair on each side of the centre point, one pair at the edge of the contacting area, and one pair at the end of specimen. The results showed that the difference between the centre and the edge of the contacting area was less than 10°C. However, due to the heat transfer between the cold blankholders and hot specimen, the temperature at the end of the specimen, was 310°C whereas the centre achieved 490°C. This is due to heat transfer at the end of the specimen where it contacts the blankholders. A large number of tests were conducted to calibrate the program settings for accurate force control. Initial tests demonstrated overshooting in the force applied due to the speed of the feedback loop control system. In order to prevent the punch from overshooting, the target stroke distances were reduced by 0 to 1.5mm, depending on the target force. The target stroke distances were carefully calibrated via a large number of tests which measured compression forces. Applying the calibrated programme, the target compression force with negligible overshooting or undershooting for each required pressure was achieved within 0.3s from the beginning of compression. As a result of all calibration tests and adjustments, even temperature distribution was confirmed within compressing area and compression force control were optimised for different conditions.

4.2.2 Pam-Stamp

In order to simulate the thermo-mechanical process between tools and specimen, an FE model was built in PAM-STAMP. The assembly of the simulation is shown in Figure 4.1. The components in the simulation were imported from the SolidWorks solid model to ensure that the simulation represents the exact geometry of the hot stamping simulator. The material properties of the die/punch materials listed in Table 4.1 were generated from an online material property database Matweb, while the properties of specimen material AA7075 were functions of temperature.

Table 4.1 Material properties of the specimen and tools.

Property	**AA7075**
Young's modulus (GPa)	$-39.082T+82532$
Density (g/m^3)	$-6.7537e\text{-}08T^{3}-0.00015T+2.8608$
Thermal conductivity (kW/mK)	$-5.145e\text{-}08T^{2}+1.368e\text{-}04T+0.085224$
Specific heat capacity (J/kgK)	$8.721e\text{-}10T^{3}-1.4625e\text{-}06T^{2}+0.0012T+0.6083$
Poisson's ratio (-)	$3.893e\text{-}08T^{2}+0.000013505T+0.325165$
Thermal expansion (-)	$0.0216T+16.499$

Property	**Tool 1 (H13)**	**Tool 2 (P20)**	**Tool 3 (Mild steel)**
Young's modulus (GPa)	210	101.4	205
Density (g/m^3)	7.8	7.15	7.85
Thermal conductivity (kW/mK)	0.0244	0.044	0.0315
Specific heat capacity (J/kgK)	460	465	473
Poisson's ratio (-)	0.3	0.29	0.285

The boundary conditions in mechanics of FE models were setup for specimen, blankholders, punch and die. The specimen, fixed by screws to blankholders, were set free in all degrees of freedom (DoF). The die was fixed in all six DoF, while five DoF of the punch, blankholders and screws were also restricted, except in the z-direction (the direction of punch motion). The mesh consisted of two DoF explicit 2 mm sized quadrangle thermal shell elements for the specimen as well as for the majority areas of tools. Triangle thermal shell elements were applied for other areas close to circular edges or curve surfaces. The total number of elements in the specimen was 240, 1561 in the die/punch, 634 in each blankholder, and 216 in each screw. The computational time for each simulation was approximately $0.03t_1$.

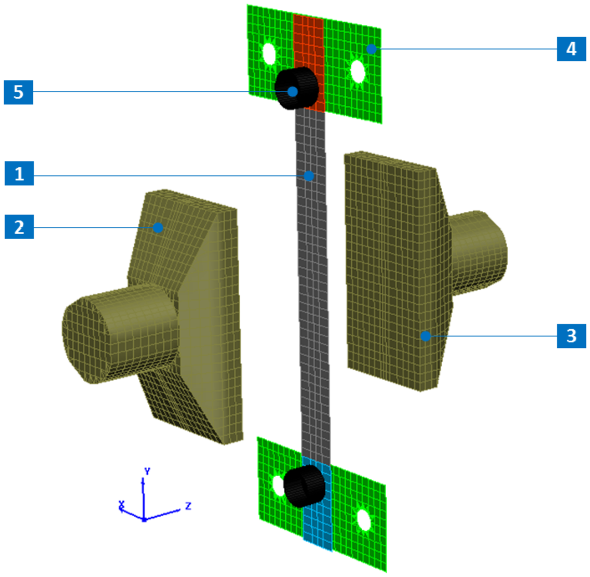

1. Specimen
2. Punch
3. Die
4. Blankholder
5. Screws

Figure 4.1 The FE model of the IHTC test in PAM-STAMP.

A pre-defined process type 'HotForming double action validation' was selected for this simulation, which indicated four stages of the forming process: (i) gravity, (ii) holding, (iii) stamping, and (iv) quenching. During the gravity and holding stages, the specimen was clamped, located, and held by the blankholders and screws, followed by the stamping and quenching stages, where the punch moves and pushes the blank towards the die at a speed of 400 mm/s, and compresses it for 4s. Corresponding to the temperature distribution test results, the initial temperature for the compression region of specimen was set uniform as

490°C, whilst that for the region contacting the blankholders was set to 310°C, and the temperature for tools was 25°C.

According to previous researches (Ji et al., 2016, Bai et al., 2012), as reviewed in Chapter 2, IHTC is highly dependent on contact pressure. Different from forming simulations models, in this FE model, IHTC values were assigned as constants not related to contact pressures so the change of contact pressure does not affect temperature evolutions in the simulation. This was due to the experimental assumption that the contact pressure was constant during the experiments, and the IHTC value also remains constant. Curves plotted from temperature evolutions at the identical locations of both tools and blanks were compared to the curves from experiments. By fitting the simulation temperature evolution to the experimental temperature evolution for both tools and blanks, the IHTC value can be determined. This was done as a function of pressure under both dry and lubricated conditions.

An example of the comparison of experimental and simulation results is shown in Figure 4.2. The points show the temperature evolution of punch and blank obtained from the experiment at 3 MPa contact pressure under dry conditions using tool 2, and the dashed lines showed the results obtained from FE simulation with assigned IHTC value of 9.2 kW/m^{2}K, (the IHTC which best fitted results with the experiment). The compressive force was not constant in the first 0.3s in the experiments due to the delay caused by feedback control system error, as discussed above, thus the first 0.3s of the experimental temperature evolution results were truncated, and the starting temperature for stamping was assumed to be the temperature at the beginning of the remaining curve. The figure demonstrates a typical conductive cool off, where the heat transfer is proportional to the temperature difference. There is a very good agreement between results obtained from the experiment and FE simulation, indicating that the IHTC value at the contact pressure of 3 MPa under the dry condition was 9.2 kW/m^{2}K, between tool 2 and AA7075 blank.

Tests with different contact pressures could give different IHTC values, and with all these results compared together, the effect of contact pressure on IHTC value could be generated. In addition, tests with different lubricant layer thickness would reveal the effect of lubricant amount on IHTC value.

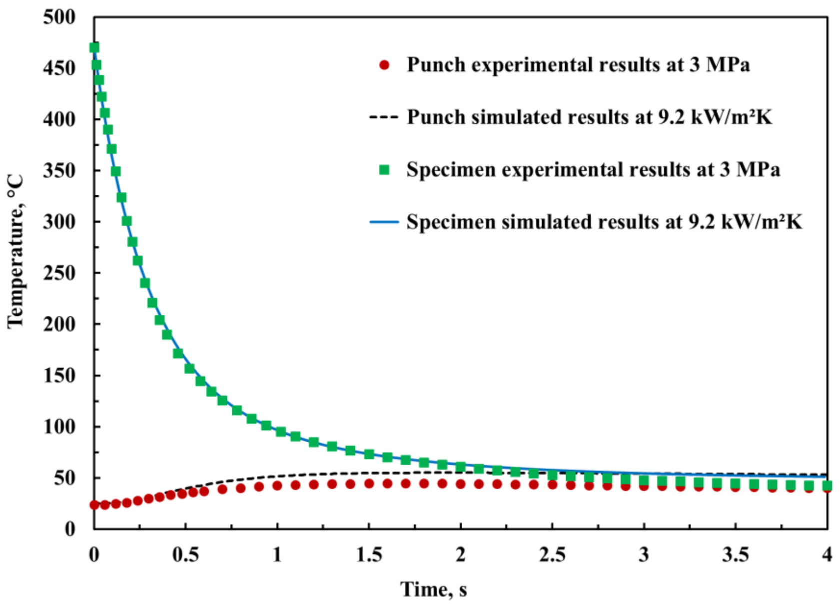

Figure 4.2 Comparison between experimental and simulated temperature evolutions at a contact pressure of 3 MPa under dry conditions, using Tool 2.

4.3 Results

4.3.1 Effect of die closing pressure

Figure 4.3(a) gives the experimental results under dry conditions between an AA7075 blank and tool 1, showing the effect of contact pressure on IHTC values. The IHTC value increases rapidly in the beginning, until the contact pressure reaches 7 MPa, where it achieves approximately 8.2 kW/m^{2}K. A moderate growth of IHTC value occurs while the contact pressure continually increases from 7 MPa to 10 MPa, followed by a plateau at a value of approximately 8.6 kW/m^{2}K for pressure higher than 13 MPa. The IHTC values between blank and tool 1 are higher than those between tools and high strength steels under the same condition, thus it requires shorter time to quench aluminium blanks compared to that of high strength steels from the same temperature.

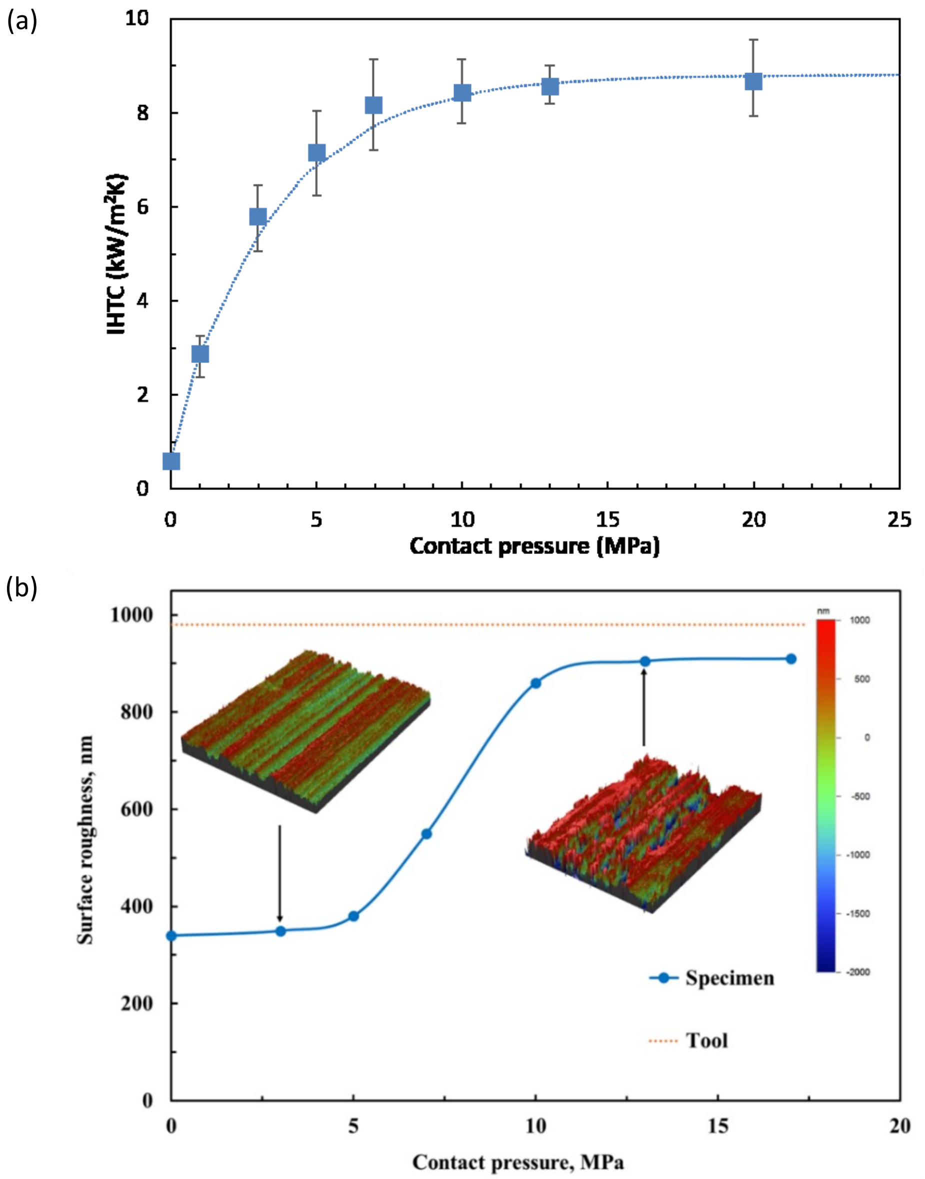

Figure 4.3 (a) The effect of contact pressure on IHTC values under dry condition; (b) The surface roughness evolution of specimen with contact pressure after IHTC tests with surface scan images; using tool 1.

The differences between IHTC values under different contact pressures were believed to be caused by the evolutions of real contact area between two contact surfaces under different pressures. As reviewed in Chapter 2, the real contact area between two contacting surfaces is much smaller than their apparent contact area, due to the materials only contacting at their asperities(Buchner et al., 2009). As the contact pressure increases, the asperities on the specimen and tool surfaces have larger deformations, thus giving larger real contact area, which leads to a higher IHTC value. However, the yield strength of AA7075 (30-300 MPa) is much lower than those of tool steels (600-1000 MPa) at warm or high temperatures. The deformation of the asperities on specimen surfaces is much larger compared to the tool surfaces, thus the increase of IHTC value is mainly caused by specimen deformation.

The surface roughness of tool surfaces and specimen surfaces were tested before and after each IHTC test at different contact pressures to characterise the effect of contact pressure on real contact area. The surface roughness on Tool 1 was 980 nm remaining constant throughout all experiments, while those for AA7075 specimens varied with different contact pressures. As discussed above, at the elevated temperature tested in the experiments, the strength of tool steel was much higher compared to the strength of aluminium alloy specimen at the same temperature range. Therefore, the asperities on the surfaces of specimens were deformed by those on the surfaces of tools during the stamping and quenching processes (i.e. the aluminium sample is deformed into cavities of the tool), leading to a growing trend of specimen surfaces roughness with higher contact pressures. The more deformation occurred on the specimen surface, the higher the true area of contact between the two surfaces.

As shown in Figure 4.3(b), there was no significant change of the specimens' surface roughness after application of contact pressures under 5 MPa, while the IHTC value grew rapidly with increasing pressure between 5 and 10 MPa. During these tests, the asperities on the specimens' surfaces were deformed by those on the tool surfaces, due to the tool material having a comparably higher yield stress. With applied pressures under 5 MPa, the deformation was mostly elastic deformations, which recovered on pressure release. Therefore, the surface condition did not significantly change after compression. As the contact pressure is increased, plastic deformation of the asperities on specimen surface occurred after yielding, and the plastic deformation remained following pressure release whilst the elastic deformation recovered. As a result, under pressures of 5 MPa to 10 MPa, the surface roughness of specimens after pressing increased significantly from 380 nm to 860 nm, approaching the value of tool surface. As a consequence, the IHTC value grew dramatically with increasing contact pressures. For pressures greater than 10 MPa, the two contact surfaces were deformed until they marched nearly perfectly, approximate 910 nm, towards the value of tool 1, thus the real contact area approached its peak value. Therefore, increasing pressure above a critical value only gives a slight increase of real contact area, leading to a plateau of the IHTC value.

4.3.2 Effect of lubricant

The grease-based graphite lubricant Omega-35 was applied onto the contact surfaces of tool 2 for the experiments studying the effect of lubricant on IHTC value. The procedure followed is presented in Section 4.2. Similar to that under dry conditions, as shown in Figure 4.4, the IHTC increases with increasing contact pressure. The green line shows the IHTC evolutions with 0.015 mm thick lubricant applied to the contact surfaces. The IHTC value at 0 MPa increased to 3 kW/m^{2}K with the application of lubricant, compared to 0.7 kW/m^{2}K under the dry condition. The value of IHTC increases rapidly with pressure up to 19 kW/m^{2}K at 7 MPa, converging to a maximum of 22 kW/m^{2}K, which was approximately 46% higher than the plateau value under dry condition.

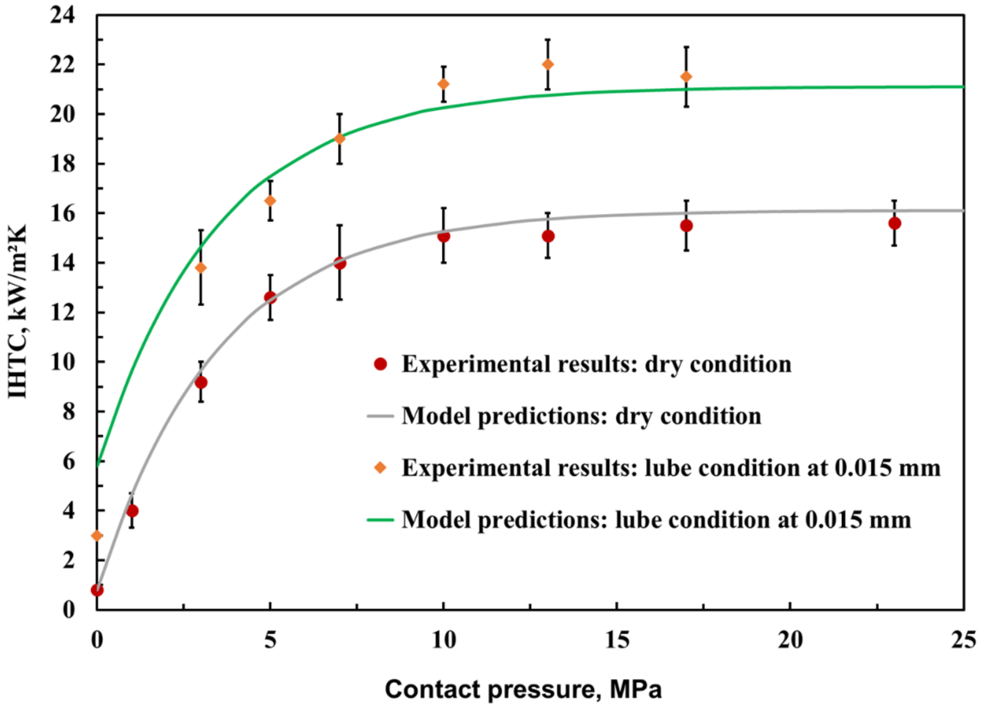

Figure 4.4 The IHTC evolutions with contact pressure using Tool 2 under dry and lubricated conditions.

The effect of lubricant layer thickness on IHTC value was also determined under the same contact pressure and the results are shown in Figure 4.5. Under a contact pressure of 5 MPa, there is an increase of IHTC value from 12.6 to 16.5 kW/m^{2}K with increasing of the lubricant layer thickness to 0.015mm. With more lubricant applied, the IHTC value remained the same as that of 0.015mm. There was a similar trend under a 10 MPa contact pressure, i.e. the IHTC value increased from 12.6 to 16.5 kW/m^{2}K followed by a plateau as the lubricant layer thickness increased above 0.015mm.

Under dry conditions, heat flows from the hot blank to the cold tools via two mechanisms: (i) thermal conduction through the asperities on the surfaces, i.e. the real contact area, and (ii) conduction & convection through the air in the non-contact areas. The heat flow via air is considered to be negligible to that of surface conduction due to the low thermal conductivity of air, and low heat transfer through free convection. Under lubricated conditions, the gaps between asperities on the contacting surfaces were filled by the lubricant, thus the air in the second heat flow route for dry condition was replaced by lubricants, whose thermal conductivity was 0.024 kW/mK, nearly 1000 times that of air, 0.0271 W/mK. As a result, the heat flow via lubricant was much greater compared to that of air, leading to a faster overall heat transfer between the two surfaces, and therefore the IHTC value increased with more applied lubricant. However, when the amount of lubricant applied on the surfaces was further increased, all the space between asperities were filled and the excessive lubricant was squeezed out during compression. There is a maximum amount of lubricant that effectively fills the vacancies between asperities, promoting greater heat transfer. In conclusion, the grease-based graphite lubricant Omega-35 had a positive effect on the IHTC value between aluminium alloy blank and steel tools.

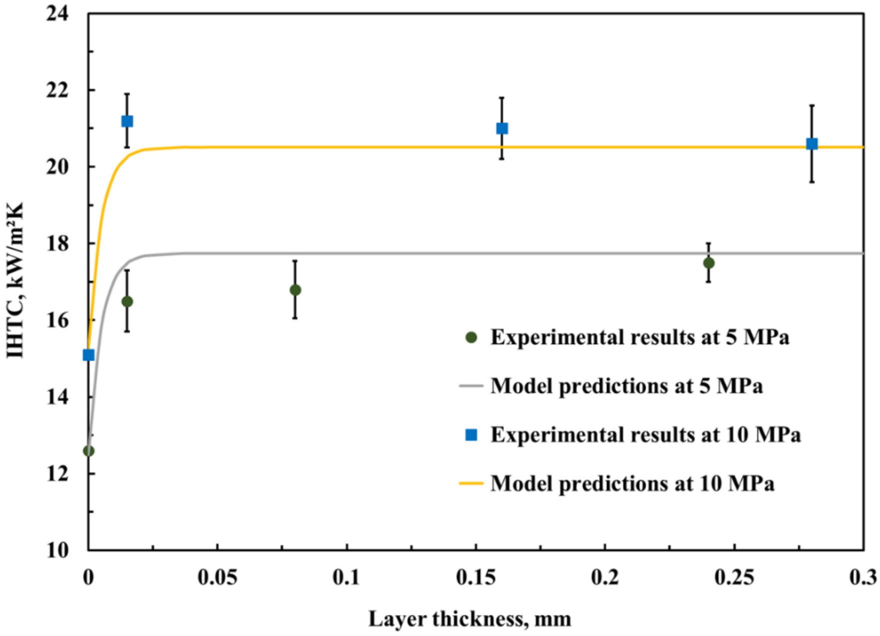

Figure 4.5 The IHTC evolutions with applied lubricant layer thickness using Tool 2, at contact pressures of 5 and 10 MPa.

A different result was generated from Zhang et al. (2010) research using glass-based lubricant, which had a negative influence on the IHTC value. This was because of low thermal conductivity (0.00125 kW/mK) of glass lubricant, which was much lower than that of graphite lubricant. It can be deduced that the IHTC value is higher when a lubricant with higher thermal conductivity is applied, resulting in a more rapid heat transfer between solid contact surfaces and thus a shorter quenching time in hot stamping processes. This effect can be beneficial in the FAST process, where a specific quenching rate is required. With a higher IHTC, to achieve the same quenching rate, the die closing pressure requirement is reduced and the tool life is therefore extended.

4.3.3 Effect of tool material

Figure 4.6 gives the comparison of IHTC values between AA7075 and different tool materials as a function of contact pressure. The black line is the same as Figure 4.3(a) with tool material 1, and the dashed line is that of tool material 2. The results for tool material 2 showed a similar overall evolution trend with tool material 1, where the IHTC value increased significantly from 0.8 to 14 kW/m^{2}K as the contact pressure increased from 0 to 7 MPa, followed by a plateau of 15.1 kW/m^{2}K when the pressure was greater than 13 MPa. Specifically, tool 2 had an approximately 76% higher IHTC peak value compared to tool 1.

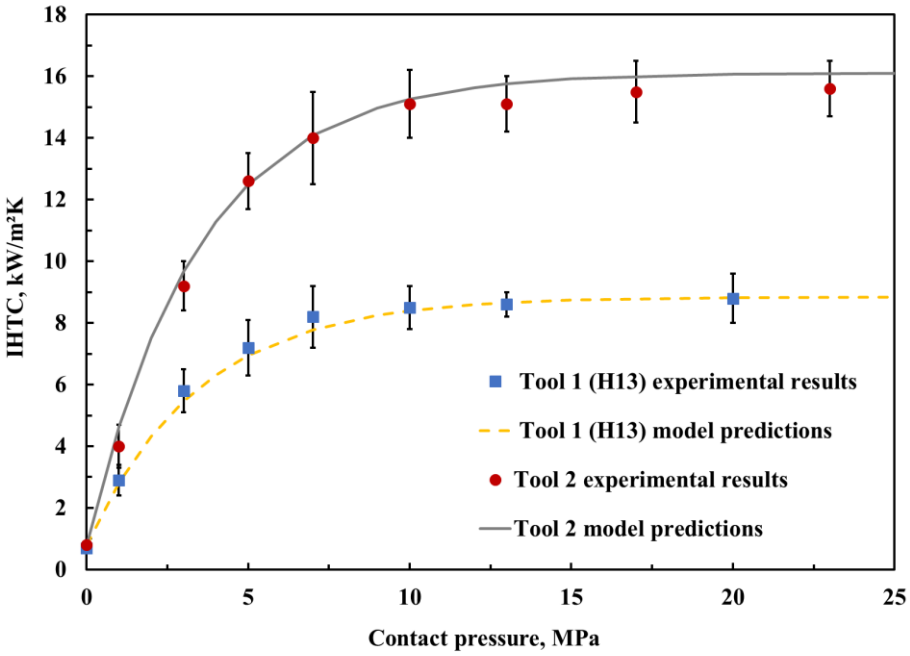

Figure 4.6 The IHTC evolutions with contact pressure using Tool 1 and 2 under dry conditions.

The difference in IHTC between the two materials can be explained by the material properties presented in Table 4.1. As shown in the table, the thermal conductivity of tool 2 was larger than that of tool 1 for the whole temperature range of the experiments, and the average value of tool 2 was 0.044 kW/mK, approximately 80% higher than 0.0244 kW/mK, the average value of tool 1. This results in higher heat flow rates between tool 2 and specimens than that of tool 1 under the same conditions, indicating higher IHTC values and thus greater cooling rates. This was verified by the results using tool 3 made of mild steel, whose thermal conductivity lied between tool 1 and tool 2, and the peak IHTC value of 12.3 kW/m^{2}K occurred in between the values with tool 1 and 2(Ji et al., 2016). The difference of specific heat capacity between the two tool materials is only 1.08%, thus its influence on IHTC values is negligible.

Compared with previous research carried out by Bai et al. (2012), the IHTC values between AA7075 and tool steels (both 1 and 2) were much higher than those between two steel surfaces including Ti-6Al-4V, 22MnB5 steel and carbon steel, leading to a higher quenching rate and shorter quenching time. Moreover, the lowest contact pressure to achieve the peak IHTC value for AA7075 was much lower than those of titanium alloys and high strength steels, because the strength of aluminium alloys at elevated temperature is lower than the other studied materials. This is beneficial for the commercial application of the FAST process, as it results in a lower requirement for contact pressure, thus extending the life of tools for stamping of aluminium alloys compared to that of high strength steels or titanium alloys.

4.4 Model development

An IHTC model as a function of contact pressure, tool material and lubricant thickness was developed based on the results obtained from IHTC experiments and FE simulations. According to the results generated, and Çetinkale and Fishenden (1951)'s equations, a widely-used model to estimate the overall heat transfer coefficient, the overall IHTC h between the aluminium alloy specimen and tools, including punch, die, blankholders and etc. are derived from the null-pressure IHTC h_c, solid-contact IHTC h_g and lubricant-contact IHTC h_l.

$$h = h_c + h_g + h_l \tag{4.1}$$

where the null-pressure h_c is the heat transfer via the air in the gap between the specimen and tools without pressure, h_g is the heat transfer under pressure between two solid surfaces, and h_l is the additional heat transfer caused by lubricant between two solid surfaces.

The null-pressure h_c is usually a small value due to the low heat conductivity of air, and it was negligible at the initial part of the heat transfer compared to that of solid contacts in experimental observations, thus the overall heat IHTC was mainly contributed from the solid-contact IHTC h_g and the lubricant-contact IHTC h_l. Therefore, the null-pressure IHTC h_c was assumed as a constant value of approximately 0.8 kW/m^{2}K, the value obtained by the experiment at zero contact pressure under dry conditions.

The solid-contact IHTC h_g was modelled combining the physical mechanism of heat transfer and the theory from Cooper et al. (1969)'s research:

$$h_g = \alpha \frac{K_{st} N_P}{R} \tag{4.2}$$

where α is a constant as model parameter, K_{st} represents the harmonic mean thermal conductivity of specimen and die, R represents the root mean square of surface roughness of the contact solids surfaces and N_P is a pressure dependent parameter. According to Cooper et al. (1969)'s research, higher thermal conductivity of both specimen and tools would be beneficial to heat transfer between them, thus has a positive influence on the solid-contact IHTC h_g. In other words, the solid-contact IHTC h_g is correlated positively with the harmonic mean thermal conductivity K_{st} . A simplified model is used to calculate the thermal conductivity K_{st}, which was considered as the harmonic mean of the average values of the specimen k_s and tools k_t within the temperature range of the experiments:

$$K_{st} = \frac{2}{k_s^{-1} + k_t^{-1}} \tag{4.3}$$

Meanwhile, the real contact area reduced with higher surface roughness, and a small real contact area has negative influence on heat transfer(Buchner et al., 2009). A reasonable deduction was therefore inferred that the root mean square (r.m.s.) of the surface roughness R negatively affected on the solid-contact IHTC h_c, where the r.m.s. surface roughness R was determined by the average roughness of specimen R_s and that of tools R_t:

$$R = \sqrt{R_s^2 + R_t^2} \tag{4.4}$$

Concluded from the experiments and the equation (4.2), the heat transfer increased with the increasing real contact area due to higher contact pressure. Thus the solid-contact IHTC h_g is positively correlated to the pressure dependent parameter N_P described by the following exponential-law equation:

$$N_P = 1 - \exp(-\lambda \frac{P}{\sigma_U}) \tag{4.5}$$

where λ is an equation parameter, P represents the contact pressure between die/punch and specimen, σ_U is the ultimate tensile strength of the raw material of specimen AA7075 at its SHT temperature 490°C. According to previous research (Cooper et al., 1969, Shlykov et al., 1977, Buchner et al., 2009, Mikić, 1974), as the specimen is significantly softer than the tools, the ratio of the contact pressure to the specimen's ultimate strength equals to the ratio of real contact area to apparent contact area between two solids' contact surfaces.

With lubricant applied, the lubricant contributes to heat transfer from the specimen to tools, the lubricant-contact IHTC h_l therefore also contribute to the overall IHTC h, where h_l is modelled by:

$$h_l = \beta \frac{K_{stl} N_L}{R} \tag{4.6}$$

where β is a model parameter, K_{stl} is the harmonic mean thermal conductivity of all the materials involved in the heat transfer including tools, specimen and lubricant, N_L is a lubricant layer thickness dependent parameter, and R is the root mean square of the roughness of both two contact surfaces. The harmonic mean thermal conductivity K_{stl} was calculated by:

$$K_{stl} = \frac{3}{k_s^{-1} + k_t^{-1} + k_l^{-1}} \tag{4.7}$$

where k_s, k_t and k_l are the average thermal conductivities of the specimen, tools and lubricant respectively.

The lubricant layer thickness dependent parameter N_L is calculated by the following exponential-law equation:

$$N_L = 1 - \exp(-\gamma\delta) \tag{4.8}$$

where γ is a model parameter and δ is the applied lubricant layer thickness.

Table 4.2 shows the material constants and parameter values of the IHTC model. The parameters were calibrated using the experimental data under both dry and lubricated conditions and two different tool materials, i.e. tool 1 and tool 2.

Table 4.2 *Material constants and model parameters of IHTC model.*

k_s (kW/mK)	**k_t (Tool 1, H13)**	**k_t (Tool 2)**	**k_t (Tool 3)**	**k_l (Lubricant)**
0.14	0.0244	0.044	0.0315	0.024
R_s (m)	**R_t (Tool 1, H13)**	**R_t (Tool 2)**	**R_t (Tool 3)**	**h_c (kW/m^{2}K)**
3.4e-7	9.8e-7	8.1e-7	9.6e-7	0.8
σ_U (MPa)	**α (-)**	**λ (-)**	**β (-)**	**γ (m^{-1})**
21	2.01e-4	6.05	1.1e-4	2e5

Verification tests, under both the dry condition and the lubricated condition, with 0.015 mm thick Omega-35, have been carried out for the predicted results calculated using the IHTC model with tool 3. Material parameters for tool 3 used in the model are shown in Table 4.2. The IHTC evolutions generated from the model were implemented into the FE simulations, and the temperature evolutions with both 3 MPa contact pressure under dry condition and 13 MPa under lubricated condition with 0.015 mm thickness were simulated. Experiments using tools made of tool material 3 have been carried out under the same conditions with the FE simulations using the hot stamping simulator, and the temperature evolutions were exported. As shown in Figure 4.7(a) and (b), the experimental results are compared to the results generated from the FE simulation, indicating good agreements under both dry and lubricated conditions, where the IHTC values were 6.7 and 14.5 kW/m^{2}K respectively.

It can be concluded that the IHTC values predicted using the IHTC model in hot stamping of aluminium alloy sheet were accurate, enabling the prediction of IHTC evolutions and temperature evolutions of specimen and tools in hot stamping as a function of die closing pressure, tool material, sheet material and layer thickness of lubricant.

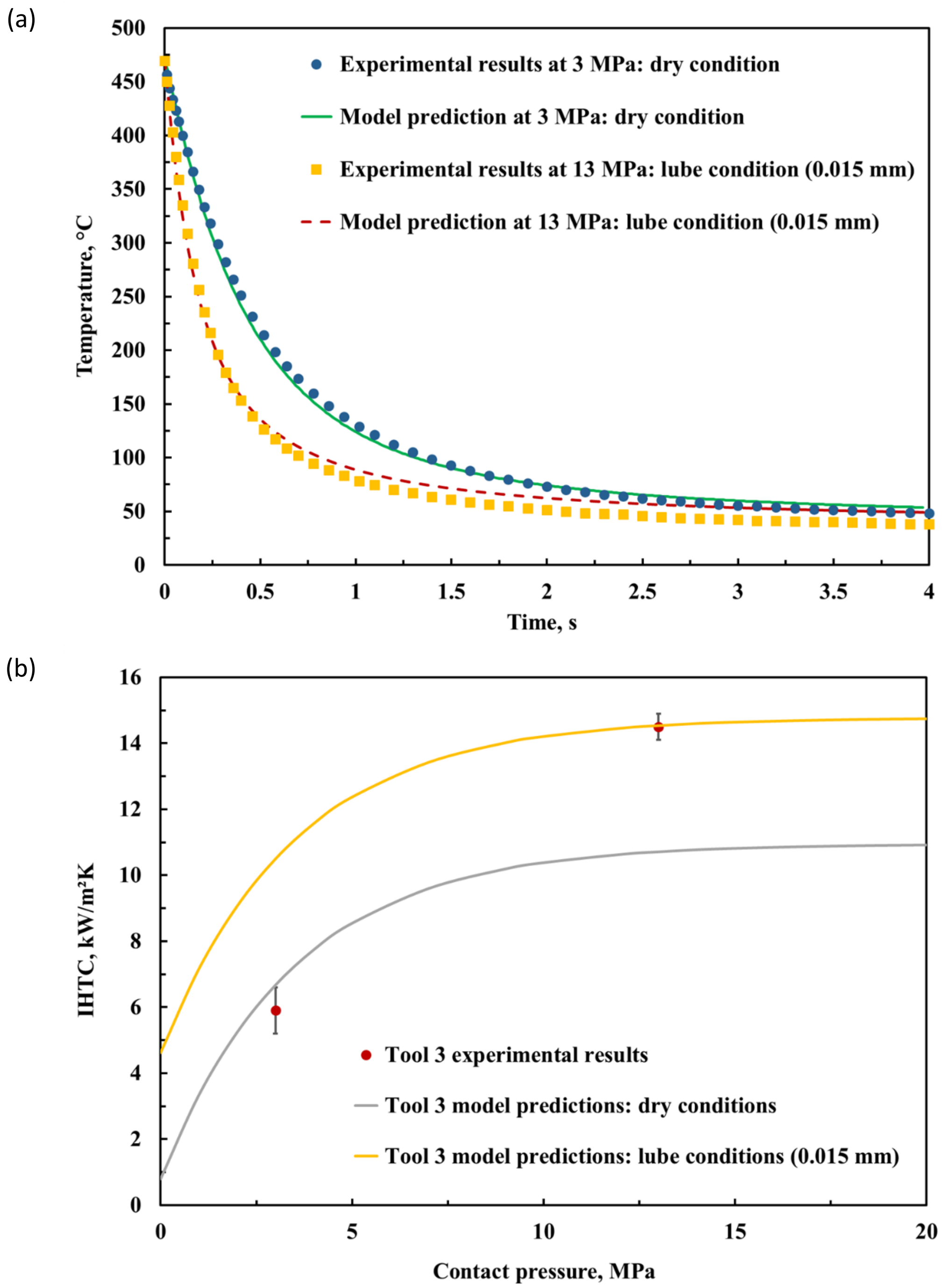

Figure 4.7 *(a) The experimental and model predicted temperature evolutions at 3 MPa under dry conditions and 13 MPa under lubricated conditions; (b) The predicted IHTC evolutions with contact pressure under dry and lubricated condition; using Tool 3.*

Figure 4.8 shows the relationship between IHTC value and thermal conductivity under a constant pressure of 15 MPa and a surface roughness of 810 nm for tool surface and 340 nm for specimen predicted by the IHTC model under both dry and 0.02 mm thick lubricated conditions. The IHTC value between the same specimen material and another tool material with larger thermal conductivity is therefore larger than tool 2, such as the AISI 1045 tool steel shown in the figure. Similarly, when using the same tool material and different blank material with lower thermal conductivity such as AA5083 in the figure, the IHTC value between tool and blank is deduced to be lower. In order to achieve higher IHTC value and quenching rate using the same tool and contact pressure, lubricant can be applied onto the tool surfaces. For instance, as shown in the figure, the IHTC value between AA7075 blank and tool 1 under dry conditions is lower than that of tool 2 at the same pressure, and it increased when lubricant was applied without change to the material and pressure.

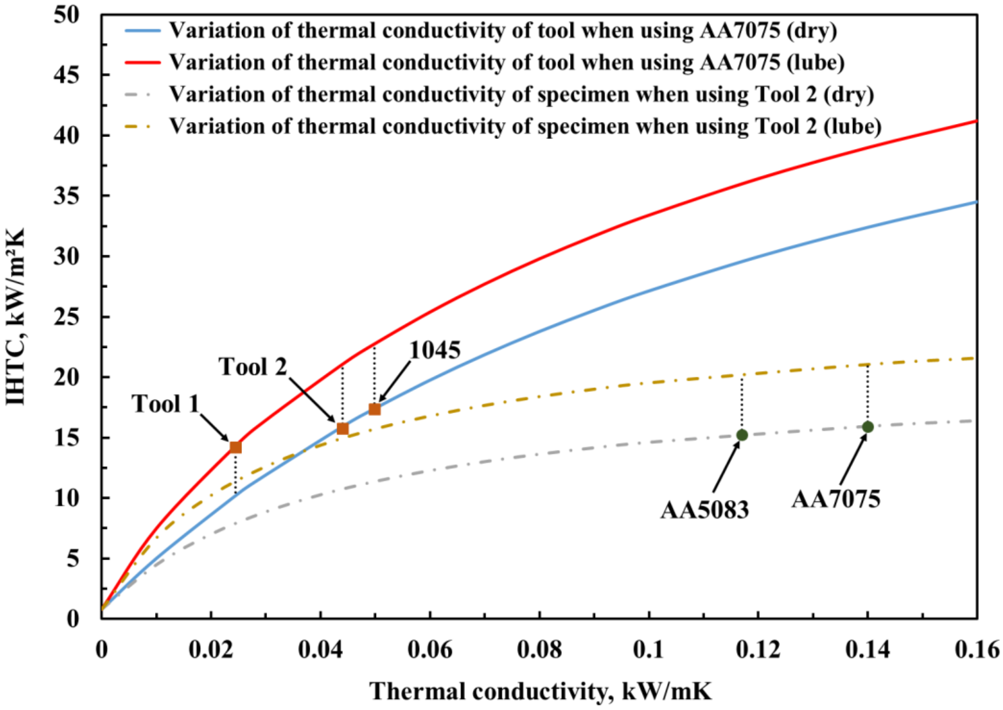

Figure 4.8 The predicted IHTC evolutions as a function of the thermal conductivities of tool material and specimen material.

4.5 Hot stamping validation tests

4.5.1 Experimental setup and procedures

Hemispherical dome(Liu et al., 2015a) and B pillar forming tests, and corresponding FE simulations using IHTC values calculated from the model were performed to validate the IHTC model by comparing the temperature evolutions of blanks during forming and quenching stages generated from experiments and FE simulations. Figure 4.9 shows the machine and tools used for the dome forming test. A Phoenix press machine with a maximum of 250kN compression force and 1000 mm/s stamping speed was used in the dome forming tests. The test rig assembled into the press machine was designed by El Fakir(Elfakir, 2015) with a pair of 120 mm diameter blank holders and a 100 mm diameter die made from tool 3. The test blank used for the dome forming tests were 180 x 180 mm, cut from 2 mm thick AA7075-T6 blanks.

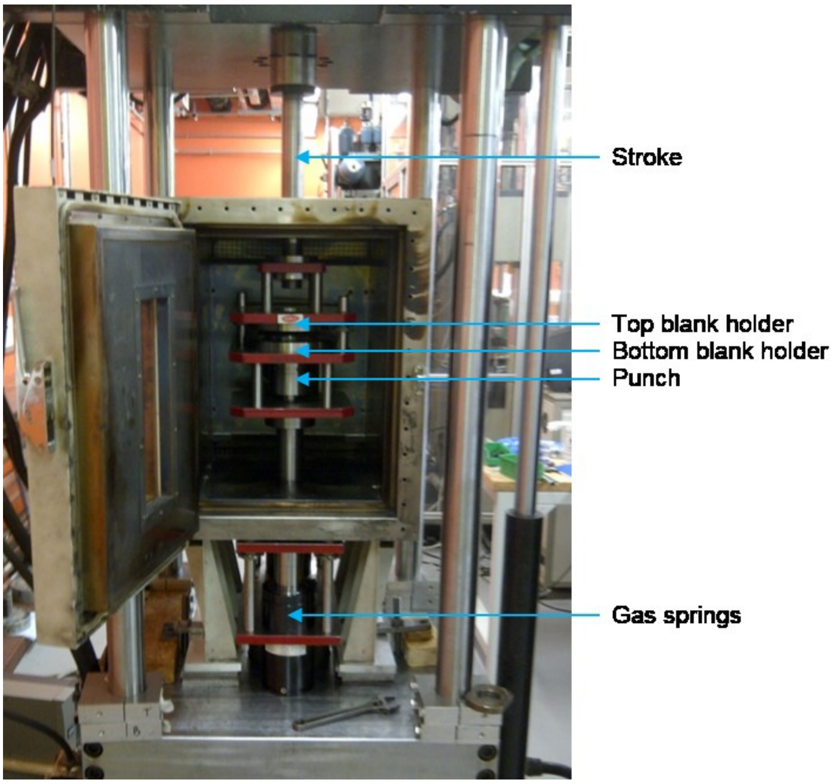

Figure 4.9 Press machine and tools used for the dome forming test(Elfakir, 2015).

A pair of K type thermocouples connected to a datalogger were embedded at the centre point of the blank in order to monitor and record the temperature evolution of the blank during all of the heating, transfering, forming and quenching stages. Prior to the forming test, the same grease-based graphite lubricant was evenly applied onto the punch surface, and the weight of lubricant applied was checked ensuring the amount could give a average thickness greater than 0.015mm, to ensure that the IHTC value is at its high plateau for the highest possible quenching rate. Firstly, the blank was heated to 490°C, and soaked at that temperture for 3 mins, generating an even temperature distribution for the blank. Afterwards, the hot blank was transferred and placed onto the bottom blankholder rapidly within 10 seconds of removal from the furnace, ensuring the temperature remained above 440°C. The temperature of the hot blank was monitored, and the press was activated when the blank tempearture reached 430°C, with a stamping speed of 75 mm/s. The hot blank is clamped by two blankholders, and moved together onto the punch at a speed of 75 mm/s, then compressed and formed by the die. The blank was formed to a dome of 10 mm height, followed by a 20s quenching, before the tools were released to their initial position.

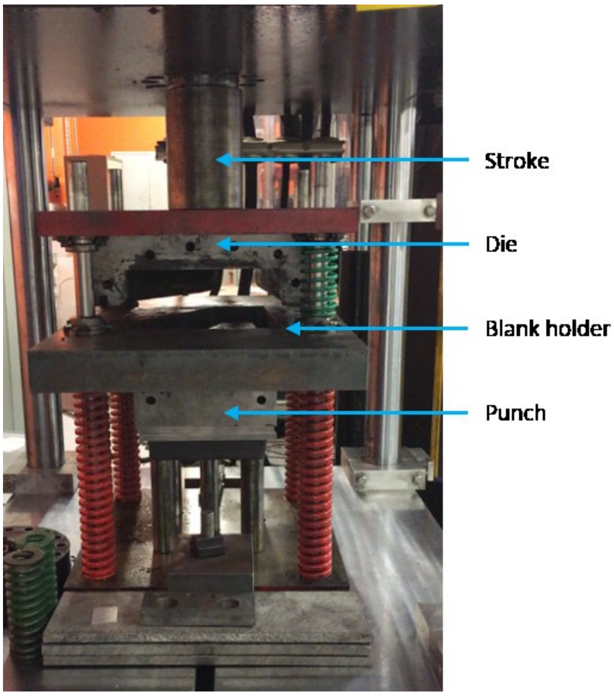

Figure 4.10 *B-Pillar forming tools.*

The B-Pillar forming test shared a similar setup and procedure with the dome forming test. The same press machine with the dome test shown in Figure 4.9 was used in the B-Pillar forming test, while the forming tools were changed to the rig shown in Figure 4.10, including a blankholder, a punch and a die made from tool 3. Similar to the dome forming test, the blank used for B-Pillar forming test was 310 x 200 mm cut from a AA7075 2 mm blank, and thermocouples were embedded 10 mm from the 310 mm edge and 110 mm from 200 mm edge. Identical to the Dome forming test, lucricants were applied onto the die and punch surfaces, and the blank was heated and soaked to 490°C in a furnace, then transferred to the blankholder within 10s. Once the blank cooled to 430°C, the machine was actuated and the punch moved towards the die, clamping the blank with a constant blank-holding force of 12kN before forming the blank. Same as the dome forming test, the stamping speed was 75 mm/s and quenching time was 20s.

4.5.2 FE simulation procedures for the validation tests

As shown in Figure 4.11 and Figure 4.12, FE models for both hemispherical dome forming test and B-Pillar forming test were developed in PAM-STAMP, sharing the same dimensions for both tools and blanks as used in the experiments. Since the blank material used in these two tests were the same as in IHTC tests and FAST tests in Chapter 5, the same material properties were applied in the FE model, whose stress-strain curves were shown in Figure 5.3(a). The mesh was the same as IHTC FE model, with 2 mm mesh size used for the blank as explicit quadrangle thermal shell elements, and an initial temperature set as 430°C. The IHTC values as a function of contact pressure predicted using the model above were implemented into the two FE models, to predict the temperature evolutions of the blanks during stamping and quenching stages. Temperature evolutions from both FE simulations and experiments for the same point were compared.

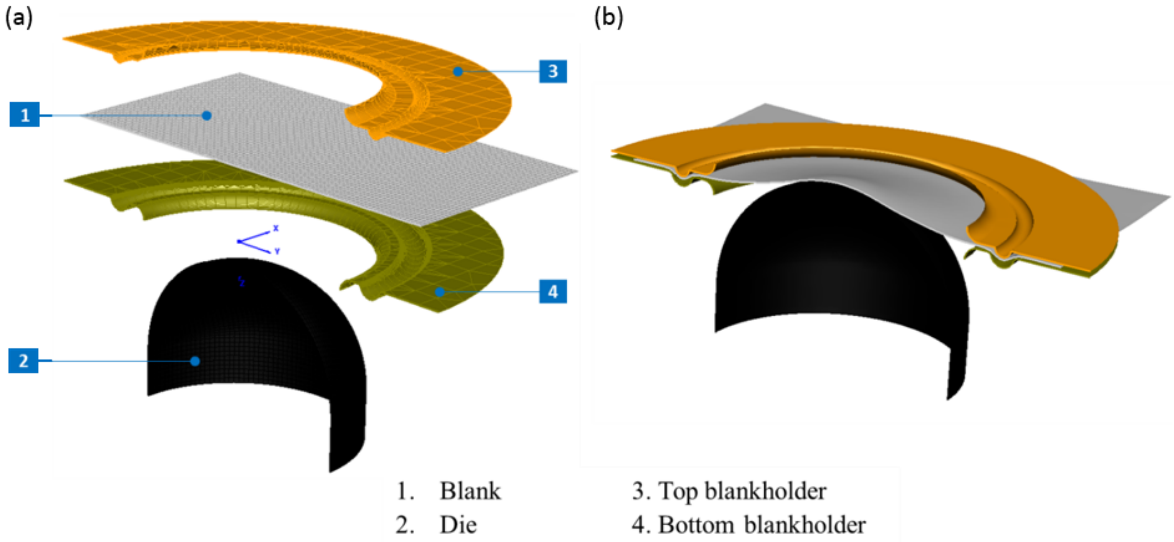

Figure 4.11 The FE model of the hemispherical dome test in PAM-STAMP (cross-sectional view), under (a) the loading condition and (b) the forming condition.

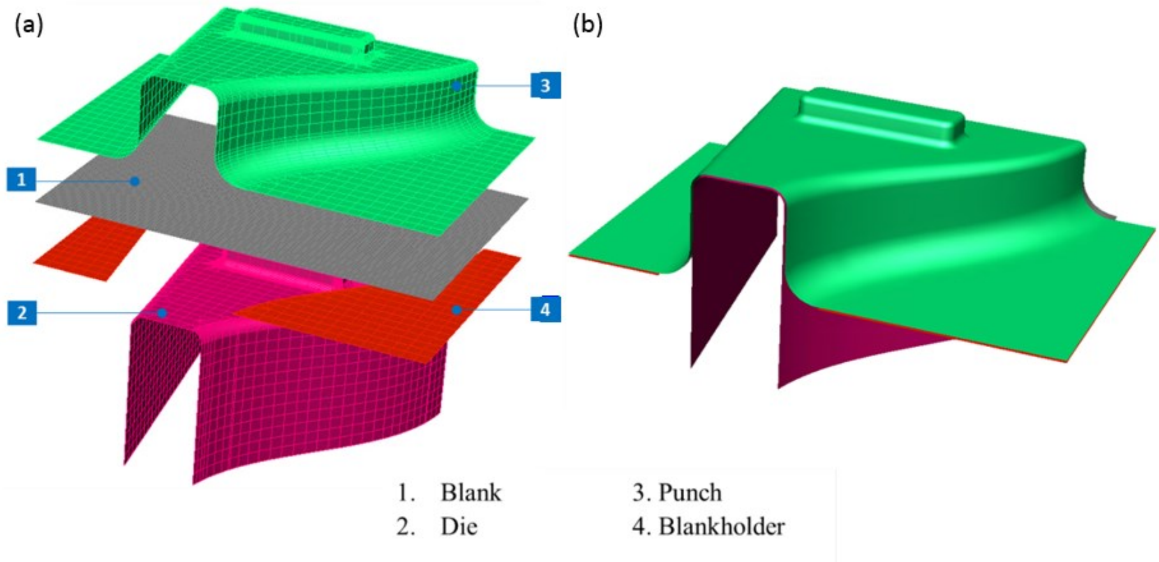

Figure 4.12 The FE model of the B pillar test in PAM-STAMP under (a) the loading condition and (b) the forming condition.

4.5.3 Validation results

The experimental results and simulated results were compared. As shown in Figure 4.13 and Figure 4.14, there were very good agreements between the two temperature evolution curves for both tests from the start of stamping, where the largest difference between simulated results and experimental results was 20°C. These hot stamping tests for the hemispherical dome and B-Pillar validate the IHTC model. After 1s quenching, the agreements between experimental and simulated curves were slightly lower with larger gap between them. However, the differences were still less than 20°C. To conclude, the overall agreement between experiments and FE simulations was good and the FE model is validated to predict the temperature evolution during hot stamping

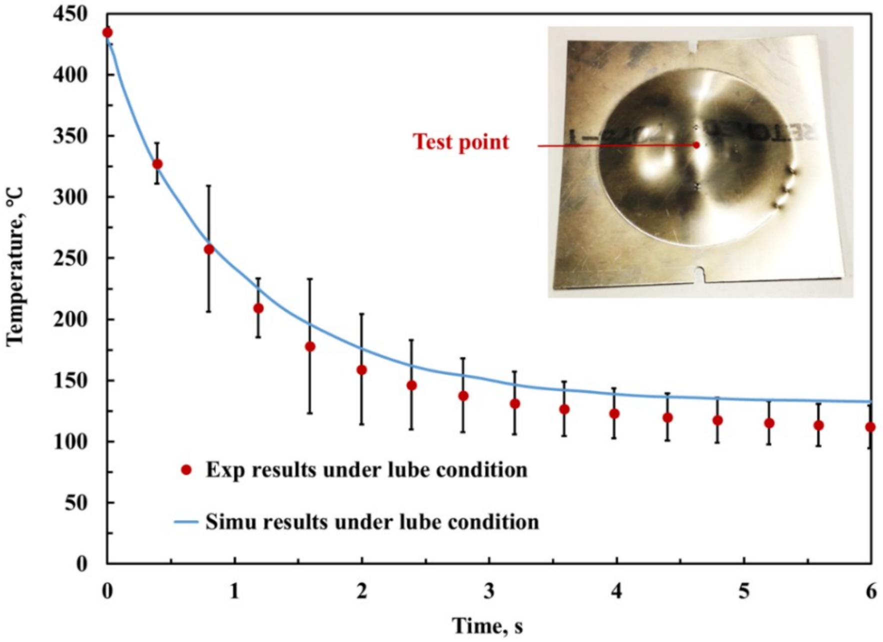

Figure 4.13 *The experimental and simulated temperature evolutions for the hemispherical dome tests under lubricated conditions.*

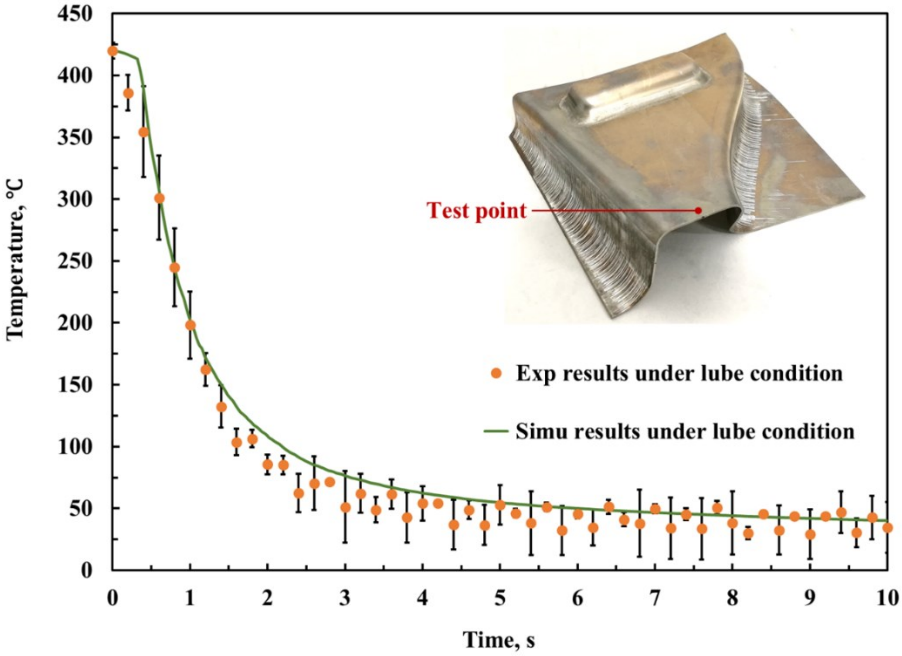

Figure 4.14 *The experimental and simulated temperature evolutions for the B pillar tests under lubricated conditions.*

4.6 Conclusions

The interfacial heat transfer coefficient (IHTC) between hot aluminium alloy blank and cold steel tools is the key parameter in calculating the quenching rate of a blank during the hot stamping process. It is thus crucial to the prediction of the post-form strength of the formed component. A novel test rig for use with the Gleeble 3800, the hot stamping simulator, was designed and used to determine temperature evolutions for both specimens and tools during hot stamping process under both dry and lubricated conditions. An FE model to simulate the hot stamping simulator was developed in Pam-Stamp, and the simulated temperature evolutions at the same location as in the experiments were fitted to the experimental results. The IHTC value in the FE model of the best fitted curves was identified as the IHTC value under that condition.

Tests and simulations have been conducted to determine the effect of contact pressure, lubricant, and tool material on the IHTC value. A positive correlation between the IHTC value and contact pressure was found under both dry and lubricated conditions while using tool steels, because the asperities on the contact surfaces were deformed more under higher pressure thus increasing the real contact area. Omega-35 graphite-based lubricant proved beneficial to the heat transfer between the specimen and tools during hot stamping. This is because the lubricant filled the gap among the asperities on the contact surfaces having higher thermal conductivity than air. This effect reached a limiting value at a lubricant layer thickness of 0.015 mm, beyond which the IHTC formed a plateau. Thermal conductivity of tool material was proved to have a positive correlation with IHTC value when other conditions remained unchanged.

An IHTC prediction model was developed based on previous research, and the results generated from experiments and FE simulations as a function of contact pressure, lubricant and tool material. The model was verified using tool 3 in the hot stamping simulator and hot stamping trials of hemispherical dome and B pillar. As applied in Sections 5.6 and 6.2.3, the model is able to predict the IHTC values between different specimens and dies under different pressures and lubricating conditions during the hot stamping process. The model-predicted IHTC values were imported into FAST process FE models, thus the local temperature evolution of blank during stamping and quenching, and therefore the quenching rate and required quenching time are predicted.

Chapter 5

Development of Fast Light Alloy Stamping Technology

5.1 Introduction

Chapters 5 and 6 are related to publications[5]. The Fast light alloy stamping technology (FAST) process has been developed and verified to form high strength and ultra-high strength components from aluminium alloys whilst meeting industry requirements for high post-form strength, ductility, formability, production rate while at a low cost. In this chapter, the effect of temper condition of blank material, heating rate, forming temperature, quenching rate, incubation temperature, incubation time, paint bake temperature and time are investigated. From these results, the optimum temperature-time profile for AA7075 is presented enabling the forming of high strength complex shaped components from AA7075 blank. M-shape and U-shape forming trials have been performed following the optimum temperature-time profile and components were successfully formed from AA7075, with high post-form strength close to T6 temper.

Due to the confidentiality agreement with industrial partners, actual time, temperature, heating rate and quenching rate values in Chapter 5 and 6 are shown in this thesis, and normalised values are applied instead. T_1, t_1 and R_1 are used as measure scales for temperature, time and heating/quenching rate respectively.

5.2 Fast Light Alloy Stamping Technology (FAST) Temperature-Time Profile

As mentioned in Chapter 1, the temperature profile for the Fast light alloy stamping technology (FAST) of AA7075 can be divided into 2 main sections as shown in Figure 5.1. The process consists of: rapid heating, forming and in-die quenching, and incubation. Heating of the aluminium alloy blank is conducted rapidly to its predefined temperature lower than its SHT temperature, then it is stamped with a high die closing speed and force enabling rapid

---

[5] A patent "Wang L., Sun Y., Ji K., Luan X., El Fakir O., Cai Z., Liu X.; A method of forming parts from sheet metal; Patent application number: 1713741.5." is being applied based on the results in Chapters 5 and 6.

cooling of the hot component. The dies are opened when the formed component is quenched to its upper limit temperature for incubation. During incubation, the formed component is removed from the tools and transferred to a heat insulating chamber or a furnace to maintain temperature until incubation is finished. The material is then placed into storage awaiting the second stage which consists of secondary fabrications and paint bake.

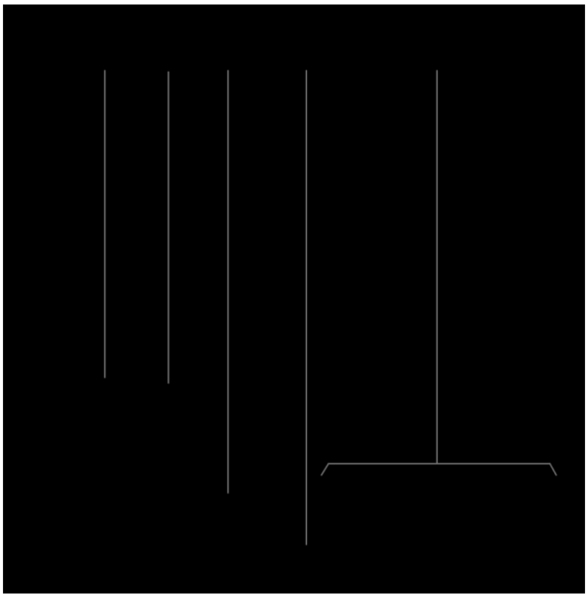

Fast light alloy stamping technology (FAST) process:

1. **Rapid heating**
2. **Forming and in-die quenching**
3. **Incubation**

Post-FAST process

4. Storage & secondary fabrication
5. Paint bake cycles

Figure 5.1 Fast light alloy stamping technology (FAST) process.

Subsequent sections of this chapter examine the effects of forming parameters on the ductility and post-form strength of the material to enable the manufacture of complex geometry components for industry OEMs. Dome tests could be used to determine the effect of strain path on formability of blank, however, due to the limitation of heating rate and control accuracy of the dome forming test equipment, the effect of strain path has not been studied and only effects of temperature and strain rate have been considered in the current study. Therefore, the uniaxial tensile tests were conducted to determine the ductility of the blank at different conditions. The hardness tests, after necessary fabrications, heat treatments and paint bake cycles was applied to the samples to replicate the material properties of produced parts and determine the post-form strength.

5.3 Study on ductility

Uniaxial tensile tests were conducted to determine the ductility of the material under different forming conditions experienced in forming operations. The effects of material temper, heating rate, forming temperature and strain rate on the ductility of the material were investigated. The uniaxial tensile tests were conducted on a Gleeble 3800 thermo-mechanical testing machine. The Gleeble system uses direct resistance heating to heat the sample, the geometry of which is shown in Figure 5.2(a). The sample was clamped between two continuously cooled jaws as shown in Figure 5.2(b) and a pair of thermocouples were spot welded and positioned at the centre of the specimen, providing temperature feedback to the system. The applied load was measured by a load cell, and the strains measured using a C-Gauge transducer clamping the centre of the specimen which read the evolution of width during the test.

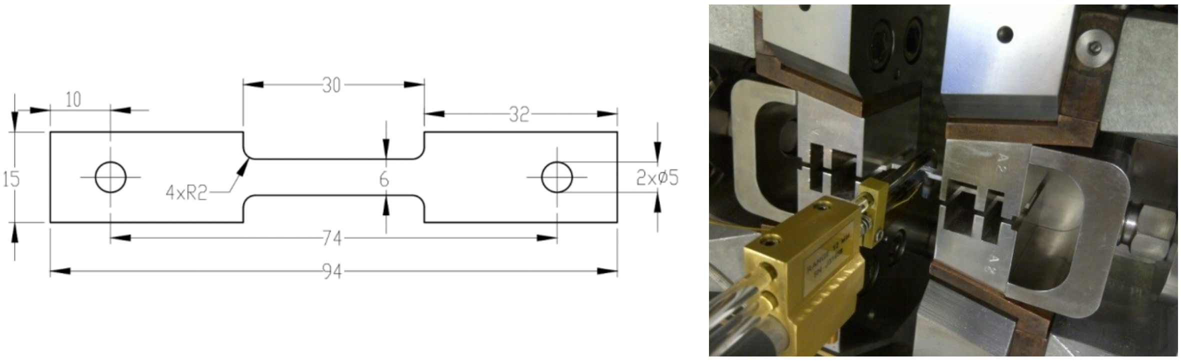

(a) (b)

Figure 5.2 (a) Dog bone shaped uniaxial tensile test sample (mm); (b) Tensile test set up in Gleeble.

Table 5.1 Full conditions for ductility tests.[6]

Raw material	**Heating rate**	**Forming temperature (/T_1)**	**Strain rate (s^{-1})**
T4, T6	High	RT~0.77	1
T4	High	RT ~0.77	0.1, 1, 5
T4	Low, Mid, High	0.69	1
T4, T6, As-quenched	High	0.69	1

---

[6] Due to the confidentiality agreement, the ‘Low’, ‘Mid’ and ‘High’ heating rates are listed here instead of the heating rate values.

Tests were conducted over the range from room temperature (RT) to $0.77T_1$ to determine the temperature providing maximum ductility of T4 and T6 temper materials. A review of the literature revealed that operational strain rate in hot stamping occurs in the range of 0.01 to 20 with 90% of conditions occurring between 0.5 and 1.5. Therefore, strain rate tests were conducted at 0.1, 1 and 5 s^{-1} to cover the majority of the test conditions using T4 temper. The effect of heating rate between Low heating rate and High heating rate was also investigated to determine the effect on ductility and identify the forming temperature for achieving peak ductility. AA7075 samples in the as-quenched condition and T6 temper were tested at the same heating rate and forming temperature of peak ductility at 1 s^{-1}, to study the effect of raw material temper on ductility. The full test conditions are listed in Table 5.1. It was found that the temperature with peak ductility was $0.69T_1$, and was chosen as the forming temperature for subsequent tests.

The true stress-strain curves for T4 temper samples at different forming temperatures are shown in Figure 5.3(a), and the true strains at fracture as a function of forming temperature are shown in Figure 5.3(b). The ductility of the test material was low at approximately 0.13 elongation at room temperature, and remains low until a forming temperature of $0.47T_1$. Above $0.47T_1$, the true strain at failure rises rapidly and reaches a peak value of 0.90 at $0.69T_1$. At forming temperature of $0.77T_1$, its strain at failure drops to a very low value of 0.24. Therefore, AA7075-T4 achieves peak ductility at $0.69T_1$ below SHT temperature. This varies from 6xxx series aluminium alloys, where forming temperature has a positive effect on ductility and peak value is achieved at SHT temperature. The low melting eutectics phase (Cu and Mg enrichment) could be one of the reasons for the low ductility at elevated temperatures, which also occurred with other Al-Cu based alloys such as AA2060, AA2024 and Weldalite. The molten instead of solid phases in the aluminium matrix reduce ductility. Increasing temperature provides more energy to melt these low-melting eutectics, leading to a lower ductility of the sample.

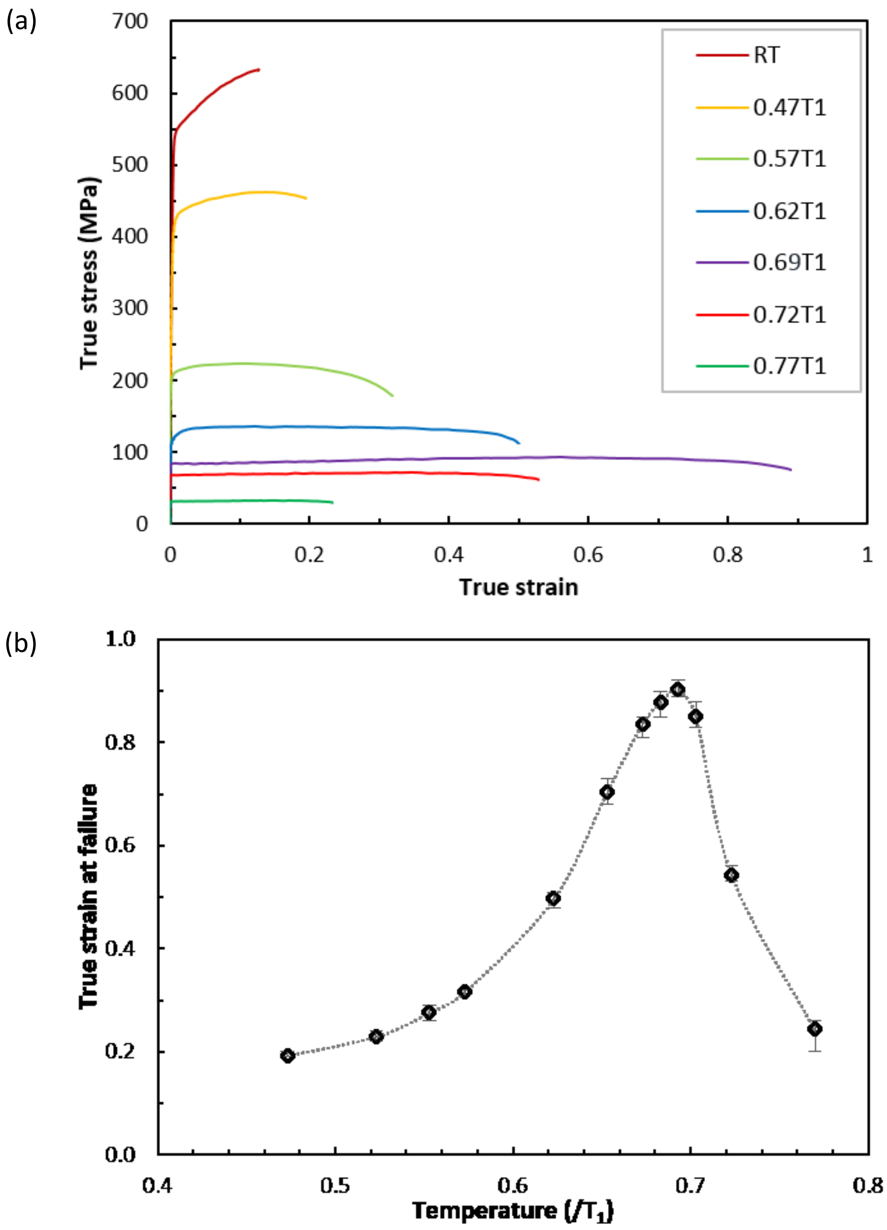

Figure 5.3 *(a) True Stress-Strain curves of the T6 samples; (b) Effect of temperature on true strain at failure of the T4 samples; tested in different temperatures at strain rate 1* s^{-1} *from 0 to* $0.77T_1$ *forming temperature for AA7075-2mm blank.*

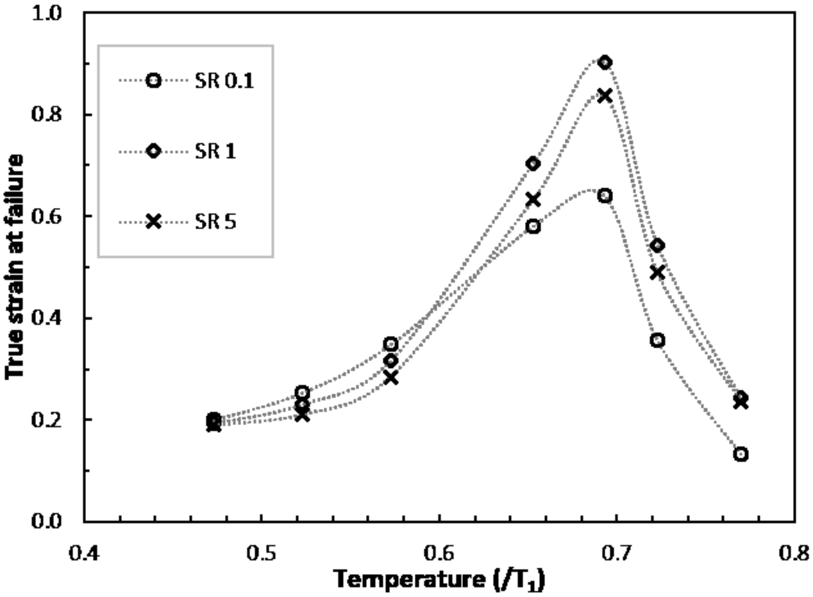

Figure 5.4 *Effect of strain rate on failure strain at different temperatures of AA7075-2mm blank.*

The test results of different strain rates at different temperatures are shown in Figure 5.4, where three different strain rates of 0.1 s^{-1}, 1 s^{-1} and 5 s^{-1} were tested with forming temperatures ranging from RT to $0.77T_1$. As seen from the figure, the overall trend for true strain at failure is a slow increase from RT to $0.47T_1$ and then a sharp rise to the peak value at $0.69T_1$ followed by a suddenly fall. When the forming temperature is below $0.47T_1$, strain rate has a negligible effect on ductility, while it has a negative correlation with ductility between $0.47T_1$ and $0.62T_1$, and the most ductile strain rate is 0.1 s^{-1}. As the forming temperature increases above $0.62T_1$, the ductility with strain rate 0.1 s^{-1} increases at a slower rate than strain rates 1 s^{-1} and 5 s^{-1} and thus it exhibits the worst ductility. At forming temperatures above $0.62T_1$, strain rates 1 s^{-1} and 5 s^{-1} are more ductile.

Table 5.2 *Tensile test results using different material tempers of AA7075 and heating rates tested at* $0.69T_1$ *with 1* s^{-1} *strain rate.*

Temper	Yield strength (MPa)	UTS (MPa)	Strain at failure
T4	83.5	93.1	0.90
T6	83.4	93.8	0.90
As-quenched	83.2	93.0	0.90

Heating rate	Yield strength (MPa)	UTS (MPa)	Strain at failure
Low	80.1	84.6	0.91
Mid	83.1	92.5	0.90
High	83.5	93.1	0.90

The effect of temper and heating rate on the materials' true strain at failure are revealed in Table 5.2, with both sets of tests performed at $0.69T_1$ at a strain rate 1 s^{-1}. As listed in Table 5.1, the evaluated heating rates were Low, Mid and High, while the material tempers were T4, T6 and as-quenched. From both results, it is seen that there is no obvious difference in true strains at failure between different materials or strain rates, although the ultimate tensile strengths and yield strengths are slightly different.

In conclusion, at all strain rates the peak ductility occurs at $0.69T_1$, where the strain rate above 1 s^{-1} has a negative effect on ductility, whereas a strain rate below 1 s^{-1} has a positive effect at this temperature. The strain rate has a negative correlation with ductility below $0.62T_1$. The effect of raw material temper and heating rate on the ductility are negligible. Thus the following post-form strength tests focus on strain rate 1 s^{-1} and $0.69T_1$ forming temperature.

5.4 Study on post-form strength[7]

Uniaxial tensile tests and Vickers Hardness (Hv5) tests were taken with the as received T6 temper material, and the tensile tests were conducted using Gleeble while the hardness tests were performed using Zwick Roell Z2.5 micro hardness tester. The T6 temper material showed 516.5 MPa yield strength, 565 MPa ultimate tensile strength and 184 Hv hardness. All hardness tests in Chapter 5 were conducted using the same hardness tester with the setup of Hv5. The post-form strength tests were taken using T4 temper materials except comparison tests for raw materials..

Artificial ageing tests were performed to study the ageing behaviours of the as quenched material using electric furnace heating and water quenching. The variables evaluated to study the effects on post-form strength include heating rate, forming temperature, quenching rate, incubation temperature, incubation time, paint bake temperature and paint bake time. The tests were conducted using the hot stamping simulator discussed in Chapter 3. During these tests, the samples were fixed between the punch and die, heated to forming temperature at a pre-defined heating rate before forming. The punch was then activated to push the sample

---

[7] Conference paper "Zhang Q., Liu J., Luan X., Ji K., Wang L. (2018). Constitutive modelling of precipitation hardening responses of a high strength 6xxx series aluminium alloy to fast warm stamping and artificial ageing. Thermec2018 - International Conference on Processing & Manufacturing of Advanced Materials Processing, Fabrication, Properties, Applications. Paris, France, July 2018. (Accepted)" is reproduced from section 5.4.

towards the die, thus quenching the sample under a pressure of 5 MPa. Once the sample was cooled to its incubation temperature, the punch was moved back to its initial position enabling material soaking at incubation temperature. After incubation, the sample was removed from Gleeble 3800 testing machine and placed in a furnace to simulate the paint bake process.

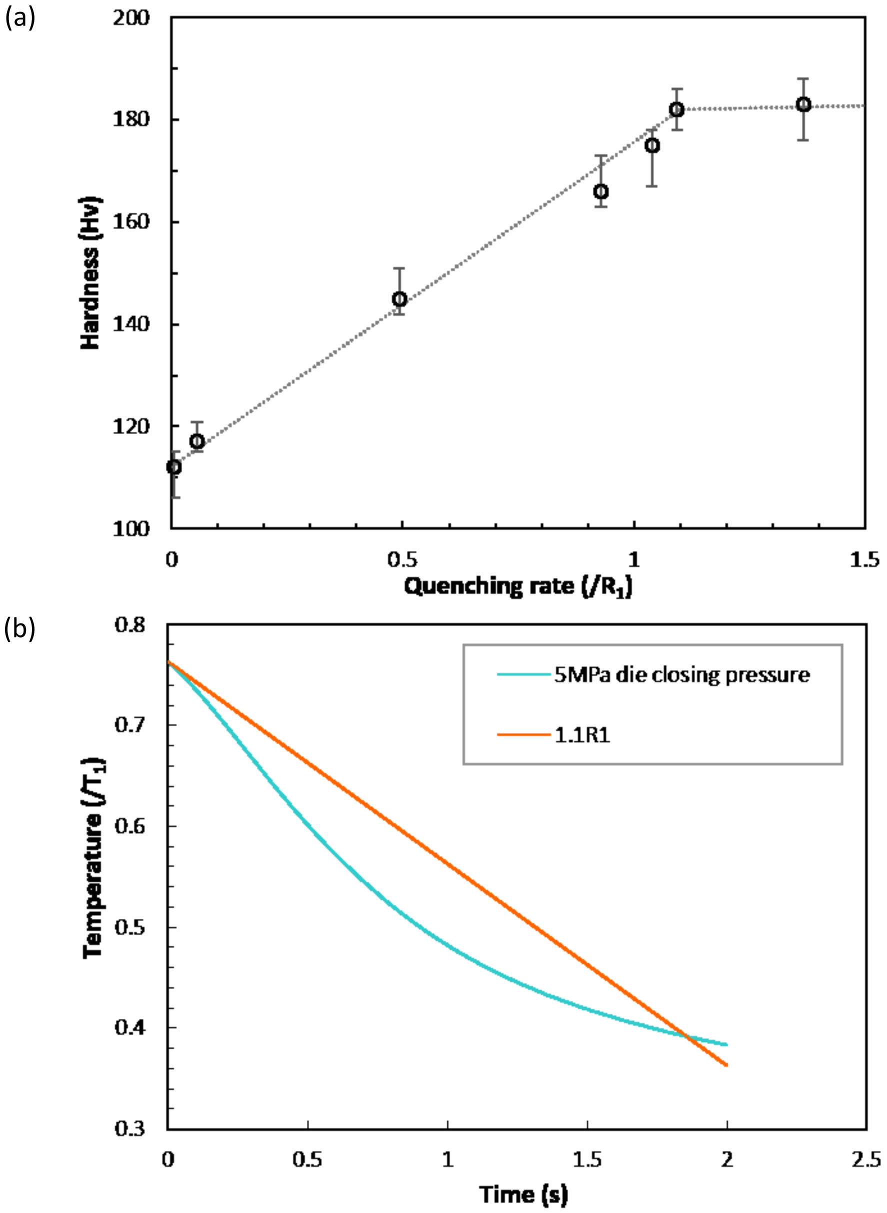

Figure 5.5 (a) Peak aged hardness cooled with different quenching rates from 0.77T_1 to room temperature; (b) Cooling curve with 5 MPa die closing pressure comparing with 1.1R_1 linear cooling for AA7075-2mm blank.

As actual cooling curves of the material quenched in a die toolset exhibit exponential decay, making an evaluation of a specific cooling rate difficult, linear quench rates were applied to the Gleeble programme to examine the effects of specific values. The experimental setup involved the use of compressed air quenching directed at the centre of the sample which was secured by tensile test clip grips. The sample was clamped in the Gleeble chamber in the same way as uniaxial tensile tests, and programmed with the same temperature profiles. Linear quench rates were achieved by high speed air flow.

In the tests using the hot stamping simulator tool, 5 MPa die closing pressure was applied during the quenching stage. As shown in Figure 5.5(a), the critical quenching rate to cool the blank from $0.77T_1$ to incubation temperature whilst achieving a post form strength close to T6 temper is $1.1R_1$. As shown in Figure 5.5(b), under 5 MPa die closing pressure, the sample temperature dropped at a cooling rate greater than $1.1R_1$. Comparison tests have been taken between 5 MPa in-die quench and $1.1R_1$ Gleeble linear quenching, and they were both peak aged to the same hardness after the ageing process. It was found that 5 MPa in-die quench could achieve the same post-form strength as $1.1R_1$ linear cooling as discussed in the following sections.

5.4.1 Effect of artificial ageing on post-form hardness

Artificial ageing aims to improve the post-form material strength as closely as possible to the as-received T6 condition. During the FAST process, the Incubation period and paint bake cycles serve this artificial ageing process. For the proposed double ageing process the incubation process represents the first stage of ageing with the paint bake cycle representing the second stage ageing.

As reviewed in Chapter 2, artificial ageing to improve material strength takes $2t_1$ for AA7075 at $0.39T_1$. The main strengthening reason for the artificial ageing process is to form fine distributed hardening precipitates, which will restrict dislocation movement. The precipitation follows the sequence during the artificial ageing: SSSS, GP zones, ɧ', ɧ. GP zones, ɧ' and ɧ are the main hardening precipitates for 7xxx series aluminium alloys, among which the ɧ' is the hardest one for the peak aged and strengthened material. ɧ' is a metastable precipitate but is stable at room temperature and low temperature. During artificial ageing, the solute atoms precipitate out of the aluminium matrix and the GP zones nucleate. As the size of the GP zones grow, they begin to transform to ɧ' and keep growing until ɧ. When ɧ' transforms to ɧ, its strength reduces and the material is overaged. In order to shorten the long ageing period of the artificial ageing of the 7xxx series materials, double stage ageing was developed to achieve peak strength in reduced time. Both single stage and double stage artificial ageing tests were conducted using samples of AA7075 as-quenched material. The samples were cut from 2 mm thick 7075-T6 blanks into 20 mm x 20 mm square shape.

The samples were heated to $0.77T_1$ and soaked in the furnace at that temperature for 30 min until fully solution heat treated. After 30 min soaking, the samples were removed from the furnace and placed into a water tank to achieve quenching immediately. The samples were removed from the water tank and dried, resulting in an as-quenched condition with SSSS microstructure. To avoid the natural ageing effect, the samples were transferred to the subsequent process before GP zones were formed.

Furnaces for artificial ageing were preheated to target temperature, with two steel blocks placed in the furnace to act as thermal capacitors to minimise temperature drop in the furnace when opening the chamber. For single stage ageing tests, the samples were soaked at $0.39T_1$ in the furnace for various lengths of time. In the double stage ageing tests, the samples were first soaked at $0.39T_1$ furnace for various times with the samples naturally cooled in air to room temperature followed by re-soaking at $0.45T_1$ for a set period of time. The effect of these soaking times on the hardness values for both the single stage ageing and double stage ageing processes are shown in Figure 5.6.

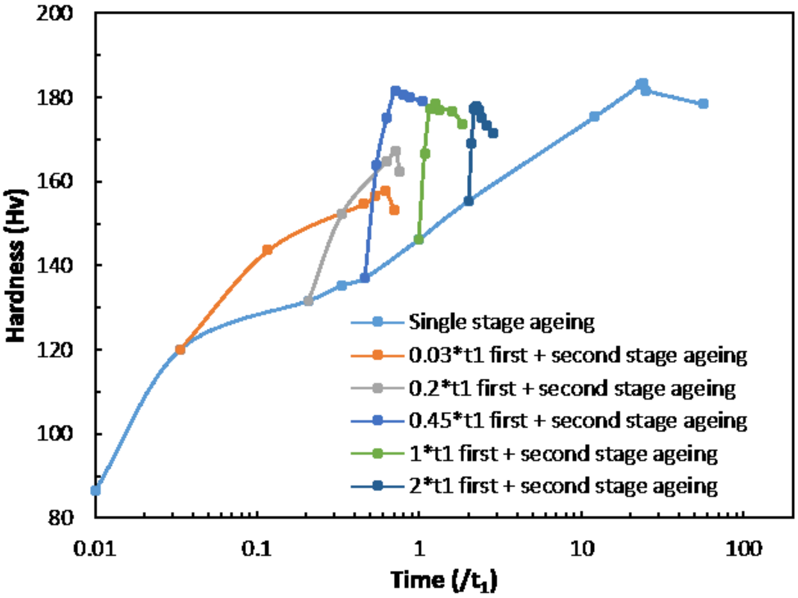

Figure 5.6 *Hardness vs Single stage ageing (at $0.39T_1$) and double stage ageing ($0.39T_1$+$0.45T_1$) time for AA7075-2mm as quenched blank.*

As can be seen from the figure, the peak hardness of 183 Hv is achieved for a single stage ageing at $0.39T_1$ for $24t_1$. The peak hardness following the double stage ageing process occurs at ageing times of $1t_1 + 0.25t_1$ respectively, with a value of 182 Hv achieved whilst reducing ageing time by 97%. It was found that peak hardness for the first step of the double stage ageing occurs at a time of $1t_1$ and slightly diminishes at times exceeding $2t_1$ whereas during the second stage, the ageing time is dependent on the first step, with ageing time reducing as the first step ageing time increases.

Uniaxial tensile tests at room temperature were performed on the samples with $1t_1 + 0.25t_1$ double stage ageing processes, showing 509.6 MPa yield strength with 558.2 MPa ultimate tensile strength respectively. The results were both higher than 98% of the as received T6 temper sample strength, which was 516.5 MPa yield strength and 565 MPa ultimate tensile strength.

A control test condition was also conducted to compare to the results. As was reviewed in Chapter 2, a higher heating rate can depress the precipitate nucleation during heating, and thus improve the peak hardness of artificial ageing. Moreover, as was discussed earlier in this chapter, peak ductility is achieved at $0.69T_1$, and therefore this was the temperature used for the control test conditions. The control test condition was set as: High heating rate, 5 MPa die closing pressure, $1t_1$ incubation at $0.39T_1$ followed by $0.25t_1$ paint bake at $0.45T_1$. Uniaxial tensile tests were conducted at the workpiece formed following the control test conditions, giving a high average yield strength of 510.2 MPa, being close to the T6 temper value. The range of test parameters is shown in Table 5.3. Due to limited material availability, hardness tests were conducted on small square samples instead of tensile tests to record a representative value of post-form strength.

Table 5.3 Parameter testing ranges to study their effects on post-form strength.

Parameter	Min	Max
Heating rate (/R_1)	0.005	1.1
Forming temperature (/T_1)	RT	0.77
Quenching rate (/R_1)	0.05	1.1
Incubation temperature (/T_1)	0.35	0.44
Incubation time (/t_1)	0.01	3
Paint bake temperature (/T_1)	0.39	0.52
Paint bake time (/t_1)	0.01	0.83

5.4.2 Effect of heating rate on post-form hardness[8]

The effect of heating rates on the post-form strength was examined for two target temperatures, $0.62T_1$ and $0.69T_1$. The evaluated heating rates had a range from $0.005R_1$ to $1.1R_1$. The control test procedure was: heating to forming temperature, stamping and 5 MPa die closing pressure, $1t_1$ incubation at $0.39T_1$ and $0.25t_1$ paint bake at $0.45T_1$.

As can be seen in Figure 5.7(a), for a $0.69T_1$ target temperature, the hardness values were similar regardless of heating rate and material temper. When forming temperature was reduced to $0.62T_1$, the hardness had significant variation as shown in Figure 5.7(b). For T4 and as-quenched tempers, the hardness was 122 Hv at $0.005R_1$ heating rate, and slowly increased to 128 Hv when the heating rate was increased to $0.05R_1$. This was followed by a sharp increase to 169 Hv at a heating rate of $0.22R_1$. This trend continues until achieving a hardness value of 174 Hv and heating rate of $0.27R_1$, where a plateau is reached and the hardness remains unchanged with increasing heating rate. The curve with rhombic markers indicates the post form strength of the components formed using T6 temper material using the same forming parameters with T4 material. The trend is very similar although the value is much lower than T4 with the peak hardness being 144 Hv. It is obvious that heating rate has a positive relation with post-form hardness, and the possible reason for it is the suppression of precipitates nucleation behaviour. With increasing heating rate, precipitation behaviour is

---

[8] Journal paper under preparation "Ji K., Cai Z., Elfakir O., Wang L. (2018). Effect of ultra-fast heating on existing precipitates and age hardening behaviour of naturally aged Al-Zn-Mg-Cu alloys." is reproduced from section 5.4.2.

depressed more, and it is reasonable to deduce that when the heating rate is high enough, the precipitation behaviour during heating is minimised and negligible.

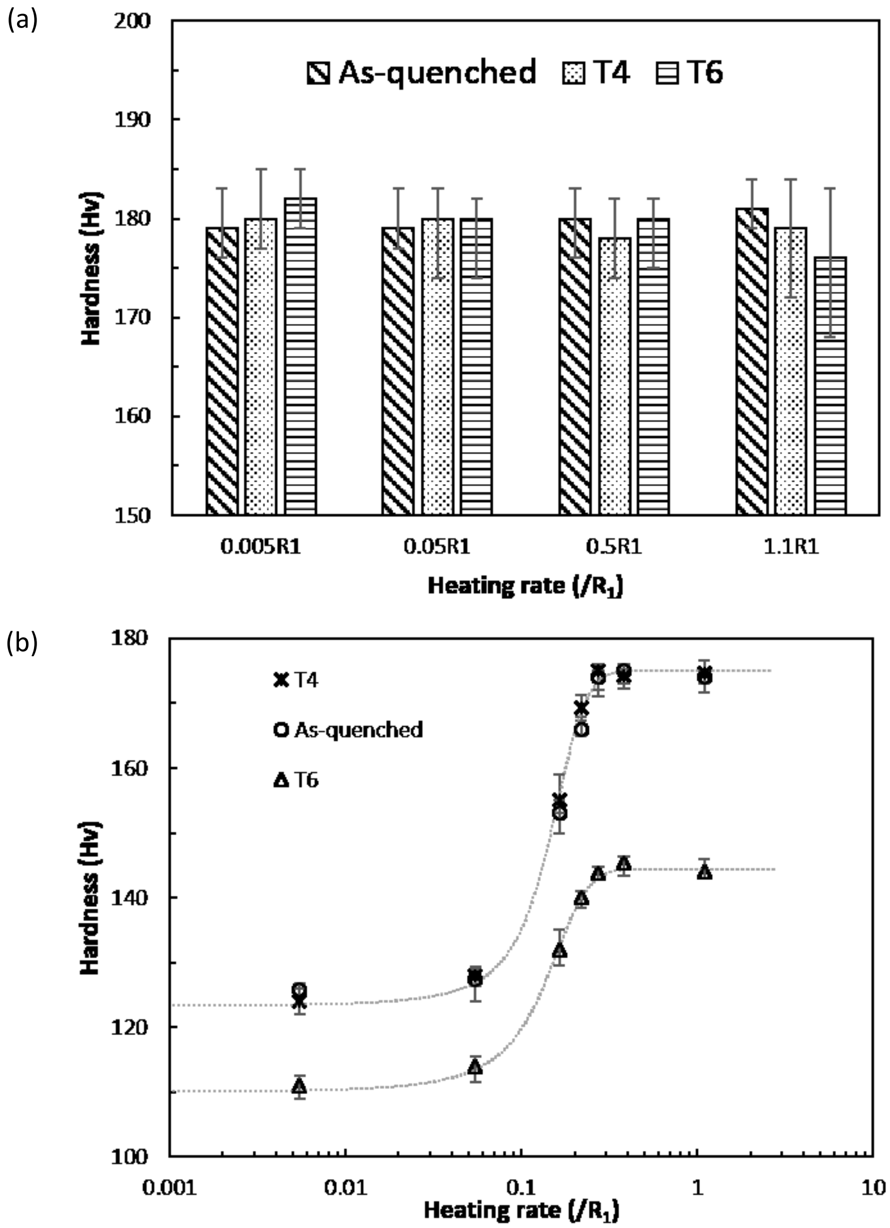

Figure 5.7 Post form hardness with different heating rate using AA7075-2mm T4, T6 and as-quenched material formed at: (a) 0.69T$_1$; (b) 0.62T$_1$.

As reviewed and discussed in Chapter 2, T4 temper material is naturally aged from as quenched (SSSS) material, and the main precipitates in T4 temper material are GP zones. GP zones are not stable and are easily dissolved when the temperature is higher than approximate 0.47T$_1$. Because of the high instability, most GP zones are dissolved as soon as the temperature reaches its critical value, thus microstructure of the heated T4 temper material becomes SSSS condition, with negligible precipitates. If the heating, forming and quenching processes are fast enough, there are very few precipitates formed during these processes. The microstructure of the quenched material would be very close to SSSS condition of as quenched workpiece, therefore it is possible to achieve a high post-form strength very close to T6 temper. This was confirmed with experimental results, whereas quenched samples were naturally aged for different time periods, and FAST formed with $1t_1$ incubation plus $0.25t_1$ paint bake. The post form hardness results are shown in Figure 5.8. It is seen that although the natural ageing improved the samples hardness in the first few days, it did not influence the post form hardness, which indicates there is no obvious difference using T4 temper and as quenched material in consideration of post-form hardness.

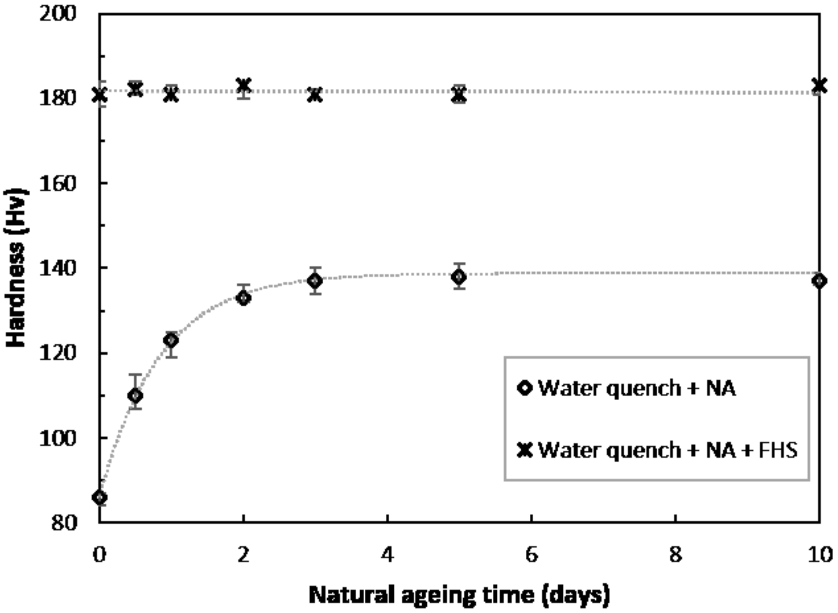

Figure 5.8 Effect of natural ageing on hardness and post-form hardness for AA7075-2mm as quenched material.

However, the main type of precipitates in T6 temper material is ɧ’, together with a small amount of GP zones and ɧ. During heating to $0.62T_1$, ɧ’ precipitates are either transformed to ɧ or coarsen. As reviewed in Chapter 2, ɧ provides less strength compared to ɧ’, thus the transformation from ɧ’ to ɧ leads to a lower hardness and strength. Considering one type of precipitate (ɧ’) only, the ageing strength of the material is affected by both the volume fraction and radius of the precipitates, and the radius is a function of ageing time. The radius of the precipitates grows with longer ageing time, and it gives higher strength against shearing by dislocations, whereas it gives a lower strength against bypassing. T6 temper material achieves peak strength by combining the effects of both shearing and bypassing, where the radius continues to grow during heating. This results in a reduction of strength as well as the transformation to ɧ, hence providing low strength when formed using T6 temper material. The other possible reason for the low strength of component formed from T6 temper blanks is the formation of S and T phases. As reviewed in Chapter 2 and explained in Section 5.3, the low melting eutectics phases S and T are transformed from ɧ' at high temperature, and their strength is much lower than ɧ' and ɧ. Some of the ɧ' precipitates transformed into S and T phases during the process when the temperature is higher than their critical nucleation temperature. These two phases remain after quenching and artificial ageing because they are stable high temperature phases. Due to the low strength of S and T phases, the post-form strength of components formed from T6 temper blanks containing these two phases is therefore lower than those of T4 temper or as quenched blanks, which is the main reason that T6 temper blanks are not usable in FAST process.

It is concluded that the heating rate does not affect the post form strength when the material is formed at 0.69T_1. However, heating rate has a positive effect on strength when it is formed at 0.62T_1 for T4, T6 and as-quenched materials. As quenched and T4 material share the same trend and value at different heating rates, but the strength of the samples formed using T6 material is much lower than the other two tempers. Therefore T6 material should be avoided in FAST. As quenched material microstructure is non-stable at room temperature, thus it expires shortly after it is produced. Therefore, T4 material is the most ideal material for both microstructure stability and post-form strength.

5.4.3 Effect of forming temperature on post-form hardness

Tests were conducted to study the effect of forming temperature on the post form hardness. The standard test procedure was: High heating rate to forming temperature, stamping with 5 MPa die closing pressure, 1t_1 incubation at 0.39T_1 and 0.25t_1 paint bake at 0.45T_1. A heating rate of 0.05R_1 was also tested to observe differences in results. The forming temperature was varied in the range from 0.47T_1 to 0.77T_1 with the results shown in Figure 5.9.

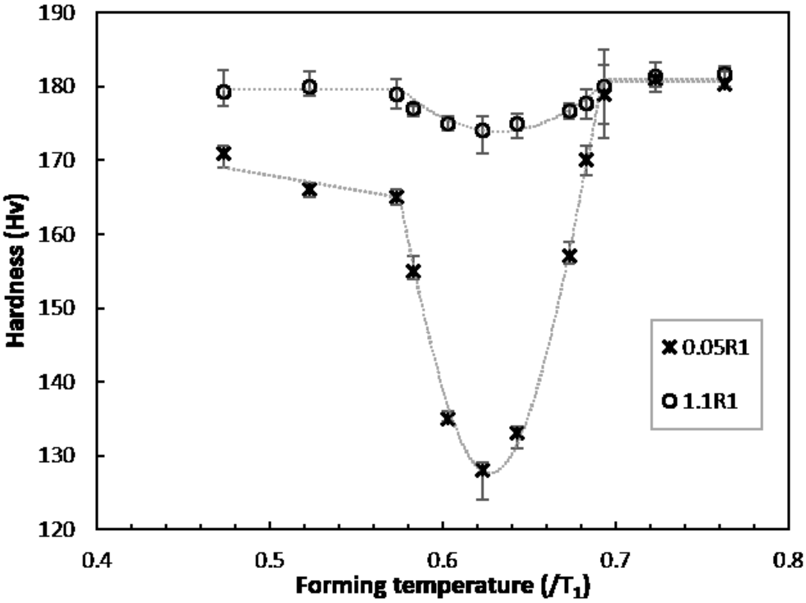

Figure 5.9 Effect of forming temperature on post-form hardness for AA7075-2mm T4 blanks at heating rates of $0.05R_1$ and $1.1R_1$.

At $0.05R_1$ heating rate, the post form hardness reduced from 171 Hv at $0.47T_1$ to 165 Hv at $0.57T_1$, followed by a rapid descent, reaching a minimum of 128 Hv at $0.62T_1$. The trend reverses as the forming temperature is increased from $0.62T_1$ reaching a value of approximately 181 Hv at temperatures $0.69T_1$ to $0.77T_1$. At $1.1R_1$ heating rate, the overall trend is similar to that at $0.05R_1$. It can be seen from the figure that heating rate influences the variance between peak and minimal hardness value, with a $1.1R_1$ heating rate experiencing a 7 Hv compared to the 53 Hv variation at $0.05R_1$. Thus, with a high enough heating rate, the post form hardness experiences minimal variation regardless of forming temperature in the range of room temperature to $0.77T_1$. Therefore, it was observed that for the same target temperature of $0.57T_1$, a critical heating rate is required to maximise the strength of the alloy. However, at a temperature above $0.69T_1$, the heating rate had no obvious effect on the hardness.

As reviewed in Chapter 2, S (Al_2CuMg) phase is formed rapidly at temperatures of approximately $0.62T_1$. This phase has lower strength than the ŋ’ phase. The more nucleation of S phase, the more solute atoms for the main strengthening precipitate ŋ’ were occupied by soft S phase, and the less solute atoms are available to form ŋ’, thus a lower strength is generated. Within the precipitation temperature range of S phase, a higher temperature provides a higher energy for precipitation behaviour, leading to increased precipitation efficiency. However, with the temperature increasing, the solubility of the aluminium matrix increases and the solute atoms free to nucleate reduces, resulting a lower precipitation efficiency. Combining these two effects, the lowest hardness point in the figure shows the temperature with highest S phase precipitation rate, is $0.62T_1$. It is seen from the figure that it is not possible to completely depress the nucleation of S phase even with a high heating rate $1.1R_1$ between $0.57T_1$ to $0.69T_1$, especially at $0.62T_1$.

It is reasonable to deduce that the critical heating rate to achieve its peak hardness is a function of forming temperature. To study this effect of forming temperature on critical heating rate, tests were performed for a range of forming temperatures and heating rates as shown in Figure 5.10. The results show that when the material is formed at $0.47T_1$, the required critical heating rate is $0.08R_1$, and increases to $0.16R_1$ at $0.57T_1$ forming temperature. This reaches a value of $0.38R_1$ when the forming temperature increases to $0.69T_1$. However, when the sample is formed at $0.69T_1$ or above, the heating rate does not affect the post-form strength and it can always achieve peak hardness value regardless of heating rate.

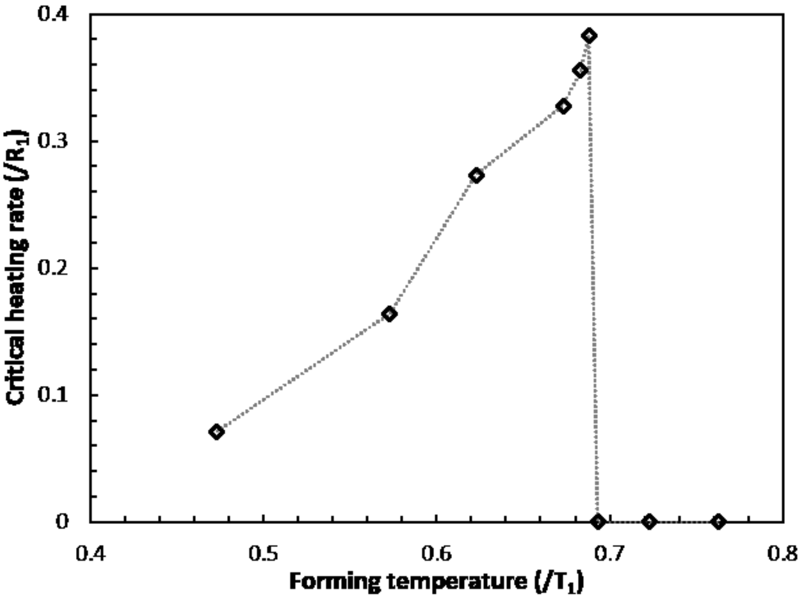

Figure 5.10 Critical heating rates for peak hardness value at different forming temperatures of AA7075-2mm T4 blanks.

Due to variations in chemical composition depending on material batch, the dissolving temperature for most precipitates can vary. According to the results of heating rate and forming temperature tests, the post-form hardness can always be retained to above 180 Hv close to T6 temper regardless of the heating rate. It is therefore reasonable to deduce that most precipitates dissolves at the temperature of approximately $0.69T_1$ for the examined batch of AA7075. When the material is heated to $0.69T_1$ and above, the precipitates dissolves in a very short time because there are few precipitates nucleated during heating. Therefore once the forming temperature is greater than $0.69T_1$, the heating rate has no effect on post-form strength. Tests were performed to heat and soak the sample at $0.69T_1$ for 30 min in a slow heating furnace, followed by water quenching and peak ageing with the hardness being 182 Hv, similar to previous tests.

It can be concluded from the results that the forming temperature has a negative effect on post-form strength below $0.62T_1$, and a positive effect above $0.62T_1$. When the forming temperature is above $0.69T_1$, it has no obvious effect on strength. The higher forming temperature requires higher critical heating rate to achieve the peak strength from $0.47T_1$ to $0.69T_1$, and the heating rate has no obvious effect on strength when it is formed above $0.69T_1$.

5.4.4 Effect of quenching rate on post-form hardness

Tests have been conducted to study the effect of quenching rate on the post form hardness. As discussed at the beginning of Section 5.4, quenching rate effect tests were taken using Gleeble without the hot stamping simulator, enabling the linear accurate control of cooling rate. The standard test procedure was: High heating rate to forming temperature $0.69T_1$, quenching, $1t_1$ incubation at $0.39T_1$ and $0.25t_1$ paint bake at $0.45T_1$. Forming temperatures of $0.47T_1$, $0.57T_1$, $0.62T_1$ and $0.77T_1$ were also applied to study the effect of forming temperature on critical quenching rate.

The post form hardness as a function of quenching rate at different forming temperatures is shown in Figure 5.11(a). At $0.69T_1$, the hardness rises rapidly from 119 Hv to 181 Hv with an increase of quenching rate from $0.05R_1$ to $0.66R_1$, and the upward trend reaches a plateau when the quenching rate is higher than $0.66R_1$. The trends of the samples formed at $0.62T_1$ and $0.57T_1$ are very similar to that at $0.69T_1$, i.e. the hardness rises significantly with the increasing cooling rate initially, and the rising trend slows down until it reaches a peak followed by a plateau. As shown in Figure 5.11(b), the peak values formed at $0.57T_1$ and $0.69T_1$ are similar at 179 Hv and 181 Hv respectively, and the peak value 174 Hv at $0.62T_1$ is slightly lower than those at $0.57T_1$ and $0.69T_1$. However, the critical quenching rate has a positive correlation with forming temperature, which are $0.16R_1$, $0.27R_1$ and $0.66R_1$ at $0.57T_1$, $0.62T_1$ and $0.69T_1$ respectively.

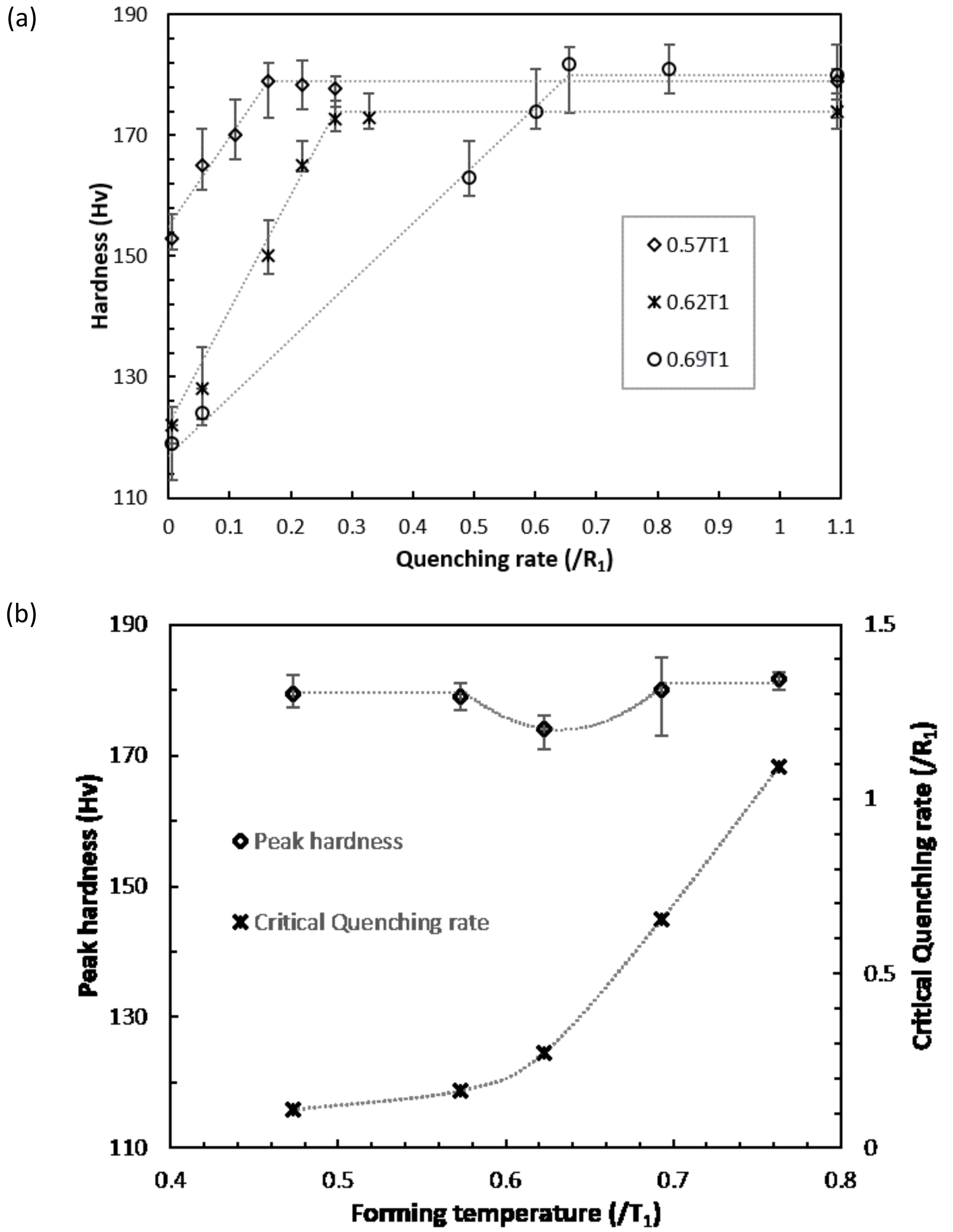

Figure 5.11 *(a) Post-form hardness values with different quenching rates formed at $0.57T_1$, $0.62T_1$ and $0.69T_1$; (b) Peak hardness values and critical quenching rates at different forming temperatures; for AA7075-2mm T4 blanks.*

Like heating rate, quenching rate has a positive correlation with post form hardness, due to its suppression effect on the precipitation behaviour during quenching. With quenching rates higher than the critical value, precipitation during quenching is almost fully depressed so that the micro structure is the same as that before quenching. Theoretically, irrespective of dislocation caused by strain, the microstructure of samples after quenching could be very close to the SSSS condition with very high heating rate and quenching rate. The main precipitates GP zones in T4 material are dissolved during heating, and because of the very high heating rate and quenching rate, there are limited precipitates during heating, forming and quenching. Thus, there are very few precipitates in the aluminium matrix after quenching.

In conclusion, quenching rate has a positive effect on post-form strength until it reaches the critical quenching rate and has a negligible effect if it keeps increasing further. The higher forming temperature requires higher critical quenching rate to achieve the peak strength.

5.4.5 Effect of incubation time on post-form hardness

Theoretically, as discussed above in the artificial ageing tests, the incubation process has the same function and purpose of the first stage ageing process, and is combined with the paint bake process (i.e. second ageing process) for hardening purposes of the formed components. The incubation time, temperature and paint bake time and temperature all influence the post form hardness of the formed components.

Tests have been performed to study the effect of incubation time on the post form hardness based on the standard condition, and incubation times between $0.03t_1$ and $3t_1$ were examined with different paint bake times in order to obtain the peak hardness values. The similar tests without heating and quenching processes are tested in the two stage aging experiments using as quenched samples. Figure 5.12(a) reveals the effect of incubation time on the post-form hardness. With $0.25t_1$ paint bake at $0.45T_1$, hardness increases sharply as the incubation time is increased from 0 min to $0.42t_1$ and reaches its peak value of 181 Hv followed by a plateau. The peak value at $1t_1$ incubation and $0.25t_1$ paint bake is very close to its T6 temper hardness.

Tests evaluating the effect of incubation time on peak hardness value and paint bake time were conducted as demonstrated in Figure 5.12(b). The results are very close to the double stage ageing tests, indicating that longer incubation time below $0.42t_1$ can reduce the paint bake time required to achieve the peak hardness, while the peak value increases for the first $1t_1$ before reaching a plateau thereafter.

(a)

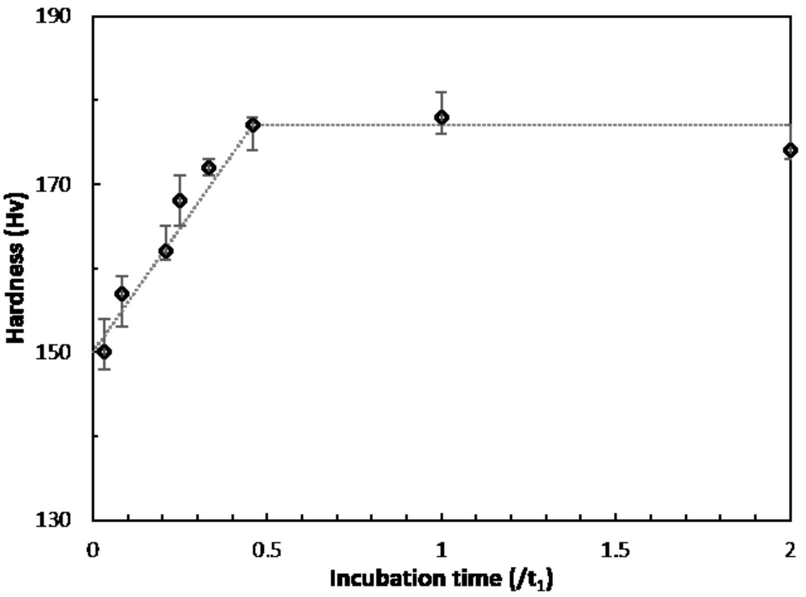

(b)

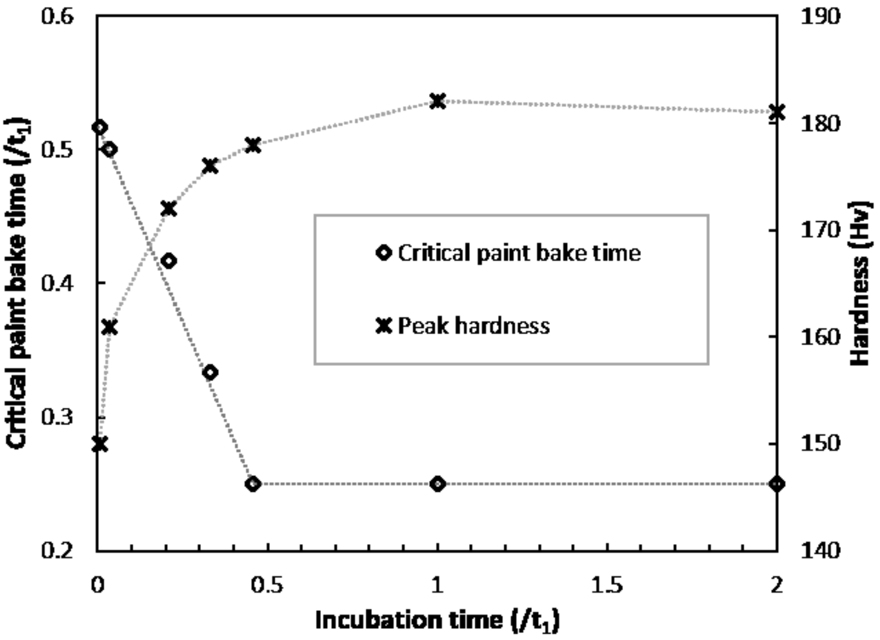

Figure 5.12 (a) Hardness values with various incubation times with 0.25t_1 paint bake; (b) Critical paint bake time and hardness at different incubation times; for AA7075-2mm T4 blanks.

In conclusion, the incubation time has a positive effect on the post-form hardness, with the 0.25t_1 paint bake process reaching its peak value at 1t_1. It also has a positive effect on the peak hardness and also reaches a peak at 1t_1, while the paint bake time required to achieve the peak hardness is reduced with longer incubation time until achieving a plateau above 0.42t_1 incubation.

5.4.6 Effect of incubation temperature on post-form hardness

Tests have been conducted to evaluate the effect of incubation temperature on post form hardness. The first set of tests were: High heating rate to forming temperature $0.69T_1$, quenching, $0.03t_1$ incubation and $0.25t_1$ paint bake at $0.45T_1$, with the incubation temperature ranging from $0.35T_1$ to $0.42T_1$. A $1t_1$ incubation with variable paint bake times was also applied to identify the peak hardness.

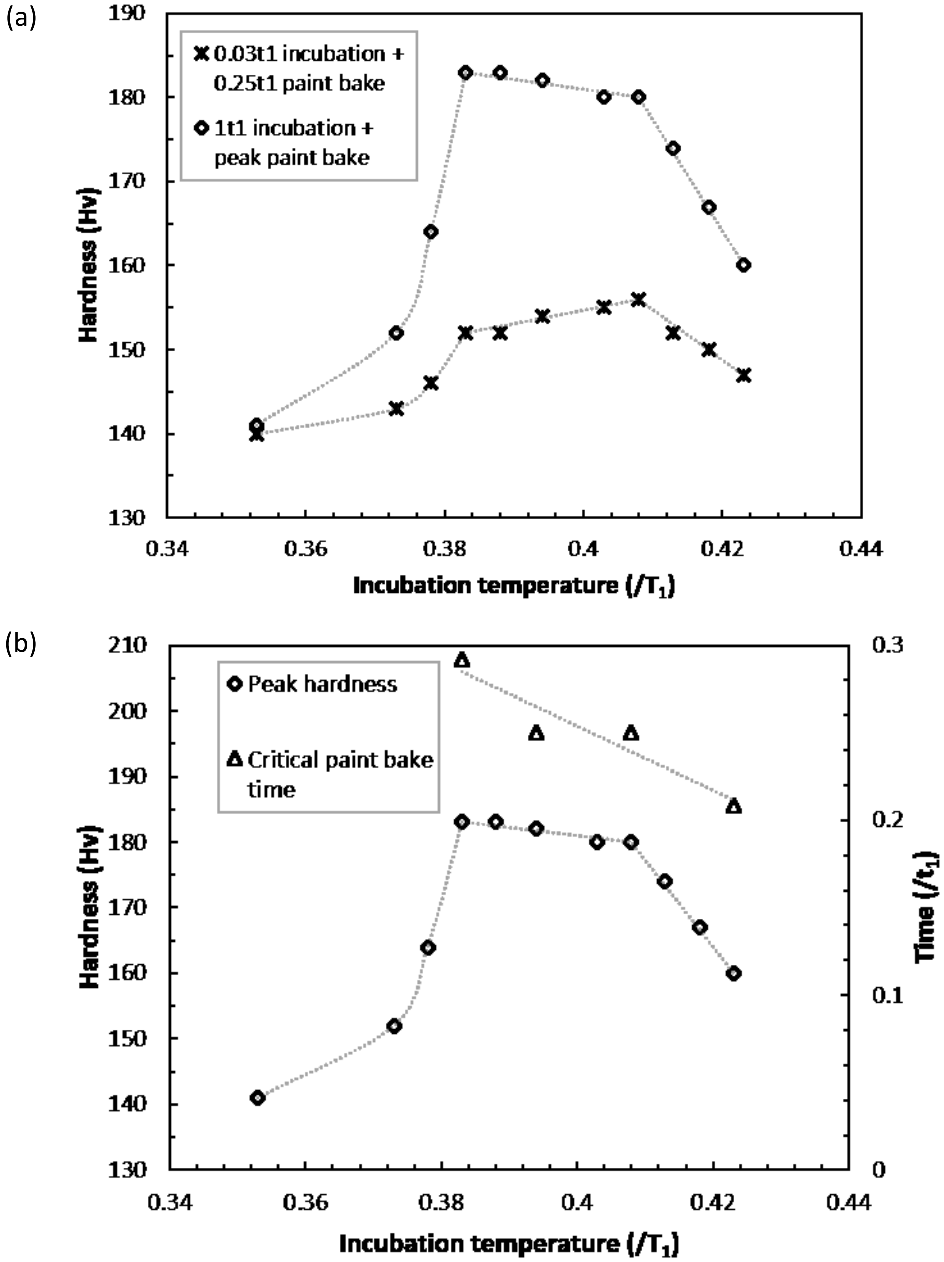

Figure 5.13 *(a) Post-form hardness with '$0.03t_1$ incubation + $0.25t_1$ paint bake' and ' $1t_1$ incubation + paint bake to peak hardness' at different incubation temperatures and $0.45T_1$ paint bake; (b) Peak hardness values and critical paint bake times with $1t_1$ incubation at different temperature and paint bake at $0.45T_1$to achieve peak hardness.*

The effect of incubation temperature on post form hardness is shown in Figure 5.13(a). The line with star markers shows the hardness with $0.03t_1$ incubation and $0.25t_1$ paint bake, indicating that hardness increases slightly from 152 Hv to 156 Hv when the incubation temperature increases from $0.38T_1$ to $0.41T_1$. However, when outside this range the hardness drops dramatically. The line with rhombic markers gives the peak hardness values with $1t_1$ incubation and variable paint bake time lengths, showing that the peak hardness value decreased slightly from 183 Hv to 180 Hv with increasing incubation temperature from $0.38T_1$ to $0.41T_1$. Similar to the $0.03t_1$ incubation tests, the post-form hardness values are much lower with incubation temperature below $0.38T_1$ or above $0.41T_1$ than those inside the range. It is reasonable to conclude that the ideal incubation temperature should range from $0.38T_1$ to $0.41T_1$ to retain the full post form hardness. Figure 5.13(b) gives information about the effect of incubation temperature on its peak hardness value and paint bake time length to achieve that peak value with $1t_1$ incubation. It is seen that the paint bake time required to achieve the peak value has a single decreasing trend in this range from $0.29t_1$ to $0.21t_1$.

To conclude, the incubation temperature has a positive effect on post-form hardness when the material is under aged and a negative effect on peak hardness when it is fully aged within the ideal temperature range $0.38T_1$ to $0.41T_1$. The critical paint bake time to achieve the peak hardness value is slightly reduced with increasing incubation temperature. However, within the ideal temperature range ($0.38T_1$ - $0.41T_1$) the effect of incubation temperature is slight.

5.4.7 Effect of paint bake time on post-form hardness

Tests to study the effect of paint bake time on the post-form hardness were conducted following the same test conditions. Besides $1t_1$ incubation time, incubation times of $0.03t_1$, $0.21t_1$, $0.46t_1$ and $2t_1$ were tested with different paint bake times.

Figure 5.14 shows the post-form hardness values as a function of paint bake time, with different incubation time lengths from $0.03t_1$ to $2t_1$. With $0.03t_1$ incubation at $0.39T_1$, paint bake at $0.45T_1$ increases its hardness rapidly within the first 10 min of paint bake and the value increases from 115 Hv to 145 Hv. The upward trend slows down with a longer paint bake time, until it reaches a peak of 161 Hv with $0.5t_1$ paint bake, followed by a slight decrease. Results of other incubation times show similar trends with that of $0.03t_1$, and as shown in the figure, the peak values increase with longer incubation time and the critical paint bake time required to achieve it is reduced. When the incubation time increased to $1t_1$, the peak value increased to 182 Hv with $0.25t_1$ paint bake only. It also can be seen that the decreasing trend after its peak is less obvious with longer incubation time.

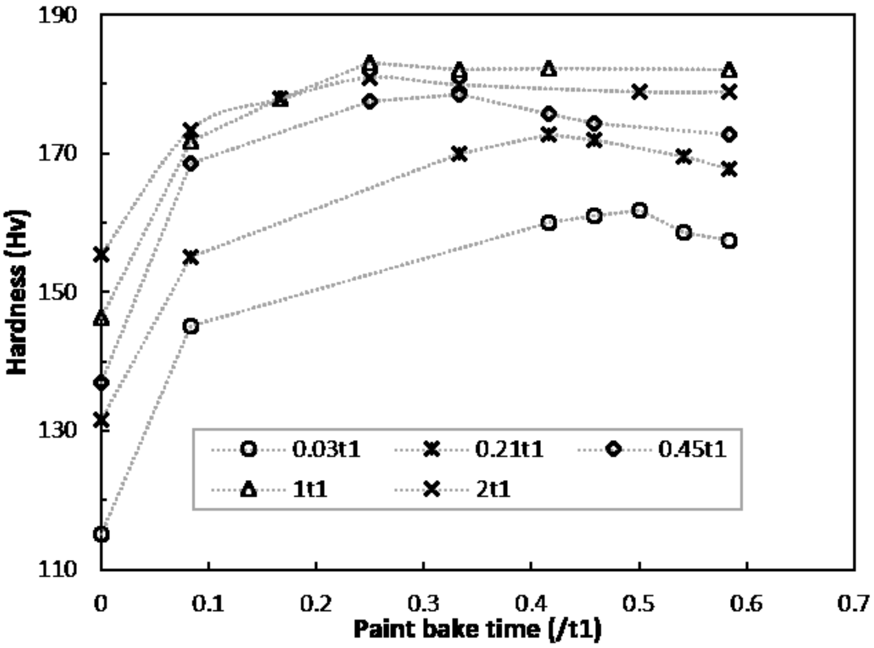

Figure 5.14 Post-form hardness with variable paint bake time length after $0.03t_1$, $0.21t_1$, $0.45t_1$, $1t_1$, and $2t_1$ incubation for components formed from AA7075-2mm T4 blanks.

5.4.8 Effect of paint bake temperature on post-form hardness

As with the incubation temperature effect, tests were conducted to study the paint bake temperature effect on post-form hardness. The tests followed the control condition, with $1t_1$ incubation at $0.39T_1$ and $0.25t_1$ paint bake at different temperatures ranging from $0.39T_1$ to $0.49T_1$. Tests were also conducted with different paint bake times and temperatures, to identify the critical values of each.

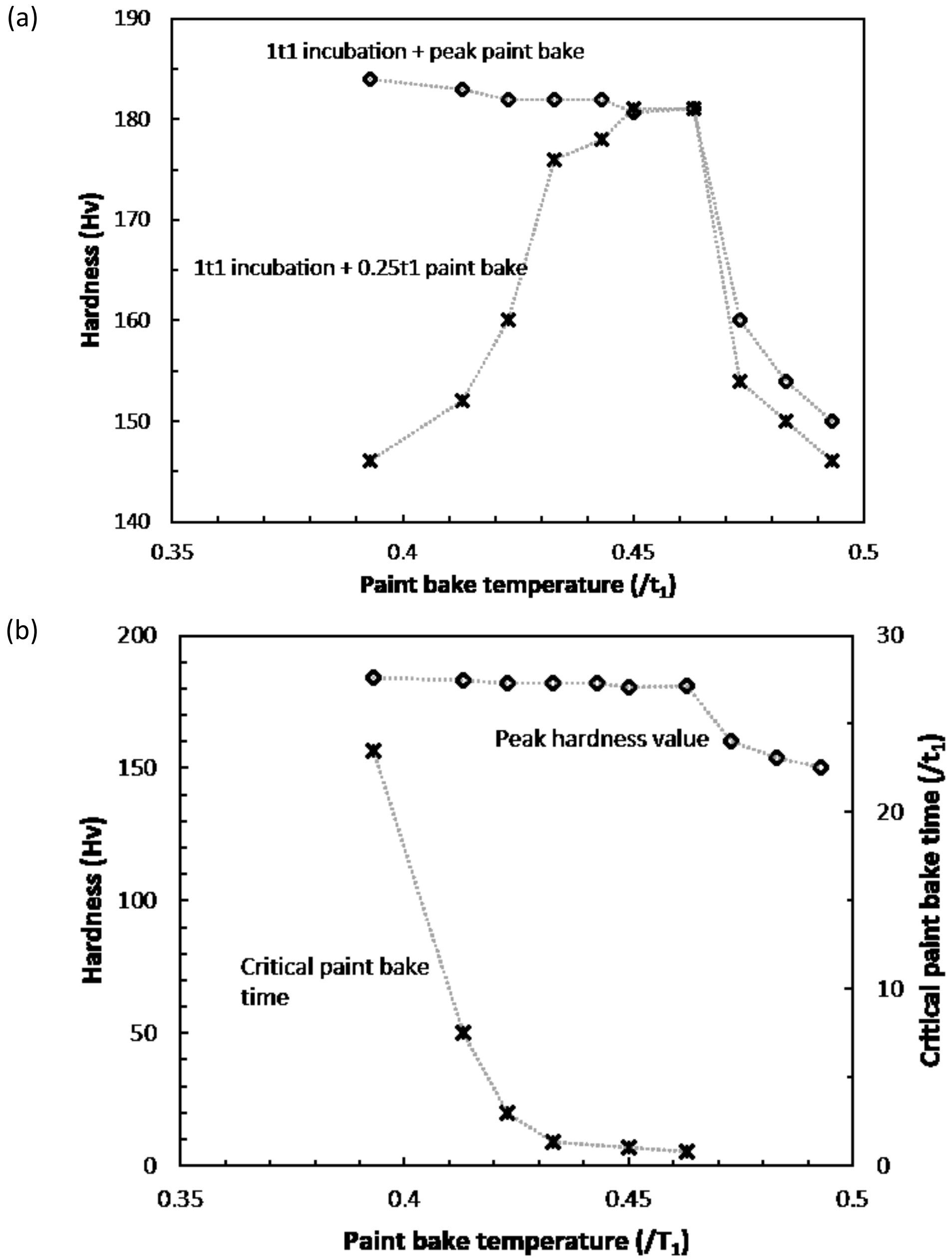

Figure 5.15 *(a) Post-form hardness with different paint bake temperatures after $1t_1$ incubation at $0.39T_1$ and $0.25t_1$ paint bake; (b) Peak hardness values at different temperatures and paint bake times after $1t_1$ incubation at $0.39T_1$.*

Figure 5.15 reveals the effect of paint bake temperature on the post form hardness with 1t1 incubation at 0.39T1 and 0.25t1 paint bake. The trend is very close to the effect of incubation temperature, and the hardness increases from 170 Hv to 181 Hv when the temperature is increased from 0.43T1 to 0.46T1. The hardness value below 0.43T1 or above 0.46T1 is much lower than the values within the range of the two temperatures. However, Figure 5.15(b) shows differences in behaviour of paint bake temperatures and times compared to incubation temperature effects. The peak hardness value remains constant when the temperature is increased from 0.39T1 to 0.46T1, and drops dramatically as the temperature rises above 0.47T1. The critical paint bake time to achieve the peak hardness value reduces from 23.5t1 to 7.5t1 when the temperature is increased from 0.39T1 to 0.42T1, and it can be further reduced to 1.33t1 at 0.83T1 and 100 min at 0.46T1. This demonstrates that adequate control of temperature in the paint bake cycle can significantly reduce manufacturing time whilst achieving peak hardness values.

5.5 Advantages

According to the tests above and the comparison with other forming technologies, there are 6 main advantages of the FAST technology in forming components from aluminium alloy blanks. These are: high post form strength, high shape complexity, high production rate, secondary fabrication availability, negligible natural ageing effect and customised forming parameters.

5.5.1 High Post form strength

As seen from the test results above, the highest post form hardness values the process can achieve using AA7075 material are 179 Hv, 174 Hv and 182 Hv at forming temperature $0.57T_1$, $0.62T_1$ and $0.69T_1$, respectively, which represents 95%--99% of the value of T6 temper. The post-form yield strength values also show very similar results with hardness values.

5.5.2 High shape complexity

The highest elongation at failure that can be achieve via FAST occurs at $0.69T_1$ for this material, which is 0.90, giving the potential to form very complex-shaped components from sheet aluminium alloys. This can save up to 95% of material compared to machining components from solid block materials.

5.5.3 High production rate

As determined from the tests above, the FAST requires high heating and quenching rates, and the highest values tested were $1.1R_1$ for both heating and quenching. Moreover, FAST does not require the component to be cooled to room temperature, and it can be removed from press machine once it is quenched to a temperature lower than the upper limit of incubation temperature, which is $0.41T_1$ for this material.

To calculate the maximum production rate, incubation and paint bake times are not taken into consideration because they can be finished in groups rather than individually. Thus the cycle time for each component is calculated by combining heating time, stamping and quenching time. Take $0.57T_1$ as an example forming temperature, with $1.1R_1$ heating and $0.55R_1$ quenching rate cooled to $0.41T_1$. The heating time, stamping and quenching time become 1.4s and 1.6s, giving a full cycle time of 3.0s. Theoretically, FAST can achieve up to 20 cycles per minute with one press machine.

5.5.4 Secondary fabrication feasibility

As reviewed in Chapter 2, ductility of the aluminium alloy sheet materials for the same temperature is affected by the microstructure of the material. In AA7075, precipitates, especially the main hardening phase ɧ’, prevent dislocations from cutting through the material and therefore reduce its ductility. Theoretically, the formed and incubated component should contain same precipitates as that with first ageing stage, which has small GP zones and only a small amount of ɧ’. Therefore, the ductility of the formed and incubated component should be better than T6 temper material at the same temperature. Uniaxial tensile tests were performed using $0.03t_1$ incubated samples at room temperature, showing a 0.19 true strain at failure, better than 0.13 of T6 temper. This gives the potential for secondary fabrications after stamping and before paint bake, such as trimming, hemming and self-rivet piercing.

5.5.5 Negligible natural ageing effect

As reviewed in Chapter 2, the room temperature storage has a natural ageing effect on the post form strength of formed aluminium alloy components if the material is not artificial aged immediately after quenching. The natural ageing effect would delay the artificial ageing time to achieve peak strength and may also lead to lower peak strength values. The first stage ageing process could depress the natural ageing effect and therefore the potential room temperature storage time to achieve full post-form strength can be extended. It is therefore reasonable to deduce that the incubation process, which has similar effects on the post form strength with first stage ageing, should have the same effect on depressing natural ageing. Tests evaluating the natural ageing effect between incubation and paint bake cycles were conducted for incubation times ranging from $0.03t_1$ to $2t_1$ at room temperature storage (20-24°C) and at times ranging from 1 hour to 15 days. To study if the incubation process can depress natural ageing, all other parameters were kept the same as the control test condition discussed at the end of Section 5.4.1.

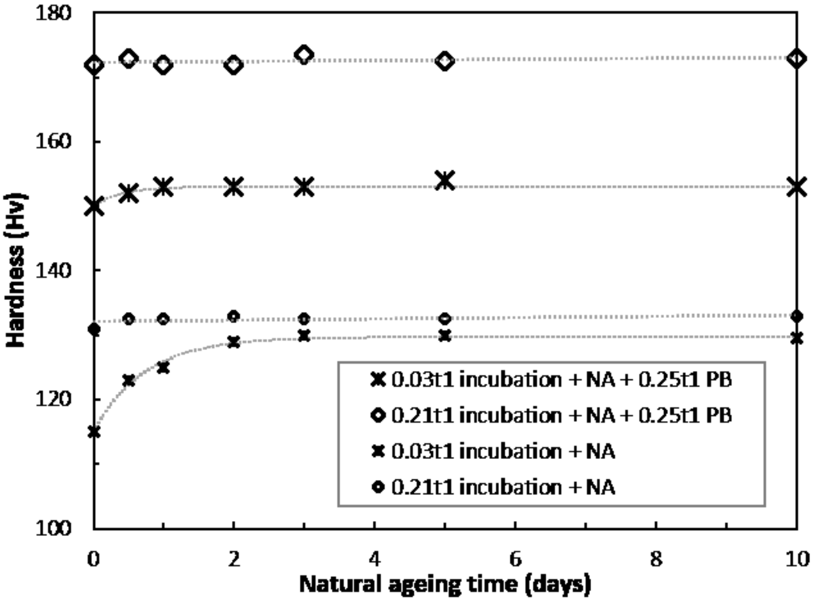

Figure 5.16 Hardness values before and after paint bake process with $0.03t_1$ and $0.21t_1$ incubation and different natural ageing times.

The results for the effect of incubation process on natural ageing is shown in Figure 5.16. The figure gives information about the hardness values before and after paint bake cycle with different natural ageing times prior to $0.03t_1$ and $0.21t_1$ incubation at $0.39T_1$. It is seen that after $0.03t_1$ incubation, the hardness of the samples increases with increased storage time at room temperature, and the hardness increased by 15 Hv after 2 days storage with $0.03t_1$ incubation. The hardness remained unchanged with or without storage (natural ageing) after $0.21t_1$ incubation. A similar trend was found after $0.25t_1$ paint bake process at $0.45T_1$, where the post form hardness increases slightly with longer natural ageing time after $0.03t_1$ incubation, while it remains constant after $0.21t_1$ incubation. However, after $0.03t_1$ incubation, although the hardness of the formed component increases by 15 Hv after 2 days storage at room temperature, it is seen that the hardness value increases a maximum of 4 Hv only after paint bake comparing the components with and without storage. With $0.21t_1$ incubation, the room temperature storage does not have any effect on the post form hardness. Incubation has the effect of depressing the natural ageing with only $0.03t_1$ incubation, and it can fully suppress the natural ageing effect with $0.21t_1$ incubation.

Regarding the microstructure of the material during heating, at temperatures below $0.47T_1$, only GP zones, ɧ’ and ɧ phases can be nucleated from SSSS during artificial and natural ageing. The peak strength and hardness are affected by the volume fraction and radius of ɧ’ phase, which is transformed from GP zones formed during natural ageing or the early stage of artificial ageing. Thus the volume fraction of GP zones formed affects that of peak aged ɧ’ phase. Volume fraction of GP zones increases rapidly in the first few minutes of artificial ageing, and becomes stable after that, while the steady volume fraction is mainly influenced by ageing temperature. During the incubation process, the volume fraction of GP zones increases to a high value close to the stable value at $0.39T_1$, and because the GP zones do not dissolve at room temperature, the volume fraction will not change significantly during natural ageing. After natural ageing, GP zones grow and transform to ɧ’ during paint bake, with the volume fraction close to that before natural ageing. Therefore, the natural ageing effect is minimised.

5.5.6 Customised forming parameters

Customising the FAST forming parameters is dependent on the chemical composition of material and forming equipment available. Based on manufacturer’s requirements and production line equipment, material must be tested via standard testing procedures (shown in Chapter 6) using the hot stamping simulator, in order to customise the best forming parameters to reduce cost and improve efficiency.

5.6 Verification

Verification tests were performed on the hot stamping simulator with M-shape forming tools and on a lab-scale pilot automated production line (UNI-form) to produce U-shaped parts(Luan et al., 2017). Tests followed the optimised conditions to achieve high post-form strength as was determined in Section 5.4.

5.6.1 M-shape forming

The M-shape forming tools are shown in Figure 5.17, which are assembled into the grips of the hot stamping simulator installed on the Gleeble 3800 instead of the flat surface tools used in the IHTC tests. The punch in Figure 5.17(a) was attached to the movable left grip and the die in Figure 5.17(b) to the non-movable right grip. The two screws holding the sample were tightened using a torque wrench with fixed torque 10Nm. The forming operation procedures were the same as the IHTC tests, with the formed M-shape component shown in Figure 5.17(c).

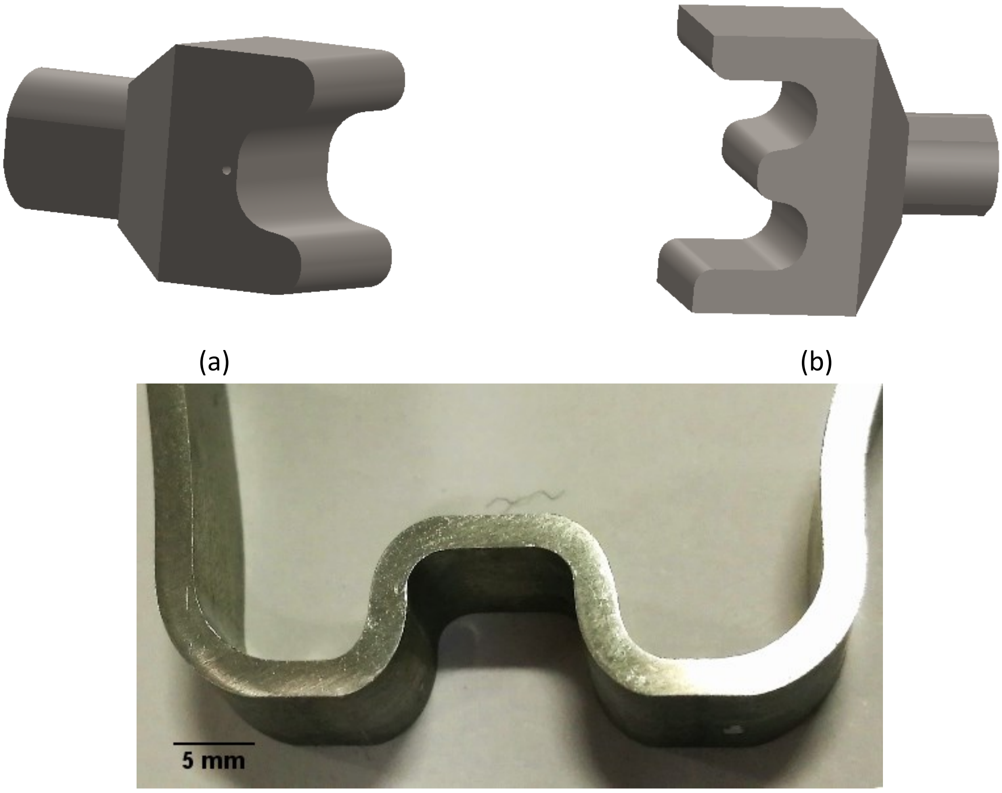
(a) (b)

(c)

Figure 5.17 M-shape forming tests: (a) Punch; (b) Die; (c) Formed component.

M-shape forming tests were conducted at forming temperatures $0.57T_1$, $0.62T_1$ and $0.69T_1$. According to tests in Section 5.4, die closing force was set as 5 MPa for higher quenching rates than the critical values, while incubation and paint bake cycles were set as $1t_1$ incubation at $0.39T_1$ and $0.25t_1$ paint bake at $0.45T_1$ to age the formed samples to peak hardness. Heating rates for the tests were defined as the critical heating rates at these forming temperatures, i.e. $0.16R_1$ at $0.57T_1$ and $0.27R_1$ at $0.62T_1$, whilst this was set to $0.16R_1$ at $0.69T_1$ due to no heating rate requirements at this temperature as discussed earlier. All 3 test conditions are listed in Table 5.4.

M-shape samples, as shown in Figure 5.17(d), were successfully formed at all 3 test conditions, and the average post-form hardness values tested along the M shape are shown in Table 5.4. The hardness values formed at $0.69T_1$ were the highest among all the tests, giving a value of 182 Hv, or approximately 99% of the T6 temper. The samples formed at $0.57T_1$ were slightly harder than those of $0.62T_1$. The trend and value were close to the test results in Section 5.4.

Table 5.4 *M-shape forming tests conditions.*

Test No.	1	2	3
Heating rate (/R_1)	0.16	0.27	0.16
Forming temperature (/T_1)	0.57	0.62	0.69
Die closing force (MPa)	5		
Incubation time (/t_1)	1		
Incubation temperature (/T_1)	0.39		
Paint bake time (/t_1)	0.25		
Paint bake temperature (/T_1)	0.45		
Post-form hardness (Hv)	180	178	182

5.6.2 U-shape forming

As reviewed in Section 2.5, UNI-form is a pilot automatic production line for hot stamping designed by researchers in the Mechanics of Materials research group in the Mechanical Engineering Department at Imperial College London, based on a 100-ton Phoenix press machine. U-shape forming tests were conducted using UNI-form to verify the FAST process with the optimised forming parameters generated in this chapter. Tests were taken to record the temperature evolution of the blank during heating with different heater temperature prior to the forming trials. When the heater temperatures were set to $0.67T_1$, $0.72T_1$ and $0.79T_1$, the blank was heated to approximately $0.57T_1$, $0.62T_1$ and $0.69T_1$ respectively within

5s heating time. This enables the heating rates to be greater than the critical heating rates at those temperatures.

As shown in Figure 5.18, during the forming tests, the blank was located between the die and punch before the forming starts, and the forming starts when the ‘Start’ key on the controller is activated. Firstly, the conveyor belts transfer the blank to the location between the two heaters, and the upper heater moves towards the lower heater. When the two half heaters and blank are tightly connected to each other, the middle platform is pushed downwards and a fixed press is applied on the blank to heat it. After heating, the upper platform releases and moves back to its initial position. The blank is then transferred from the heaters to the die and punch by the conveyor belts, and the stroke is activated again to push the upper platform, driving the die to the blank holders and punch. The die presses the blank and touches the blank holders first before the punch. When the punch is fully contacted, the blank is formed. A constant die closing force is applied during the forming and quenching. After the blank is fully quenched, the upper platform moves back again and the formed component is transferred into the incubation chamber for incubation. After $1t_1$ incubation at $0.39T_1$, the whole forming procedure is finished and the component is removed and placed into a pre-heated furnace for $0.25t_1$ paint bake at $0.45T_1$.

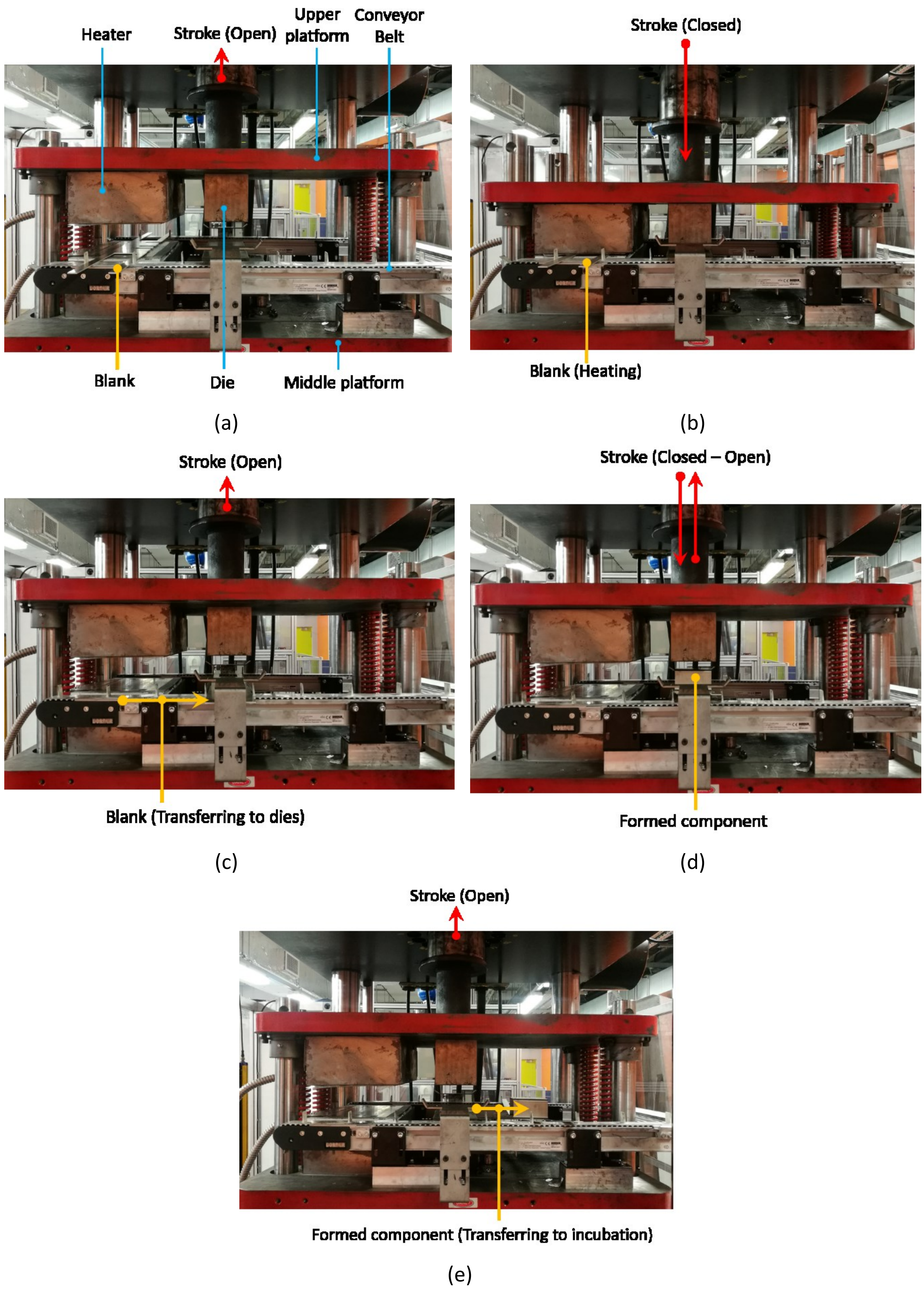

Figure 5.18 Forming process using UNI-Form automatic production line: (a) loading blank; (b) heating; (c) transferring; (d) stamping and quenching; (e) transferring to incubation (Luan et al., 2017)(Luan et al., 2017)(Luan et al., 2017).

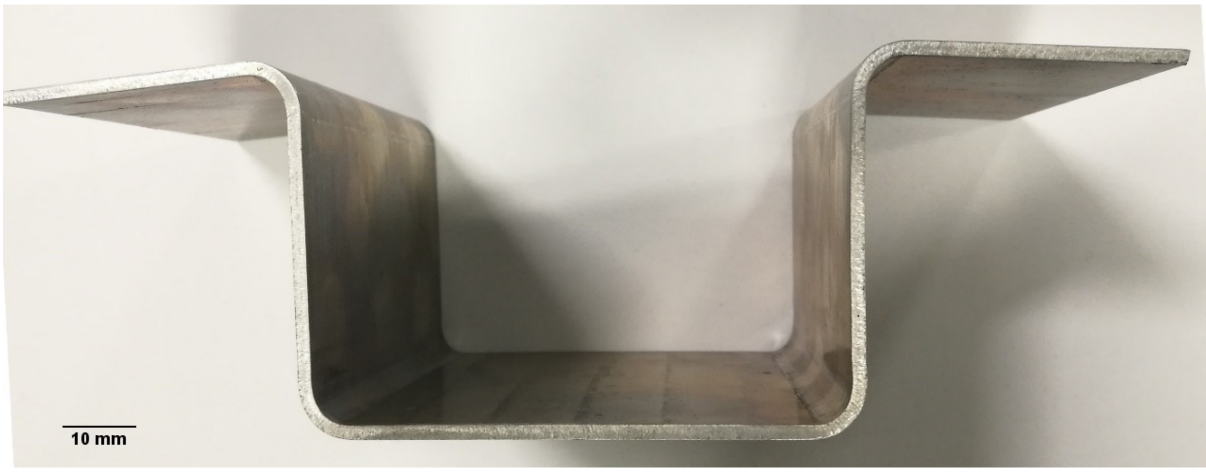

Figure 5.19 *Successfully formed U-shape component.*

As shown in Figure 5.19, U-shape components were successfully formed and hardness tests were conducted on the components following $0.25t_1$ paint bake at $0.45T_1$. The hardness values were recorded as 178 Hv, 176 Hv and 180 Hv for forming temperatures $0.57T_1$, $0.62T_1$ and $0.69T_1$ respectively. The post-form strength achieved was close to T6 temper.

5.7 Conclusion

The FAST process has been successfully developed and the effects of main parameters on the ductility and post-form strength were studied. The effects on ductility are:

- Heating rate and material temper do not have obvious effects on ductility;
- Forming temperature has a positive effect on ductility below its peak temperature $0.69T_1$, and becomes negative above $0.69T_1$;
- Strain rate is negatively related to ductility below $0.62T_1$, and when it is above $0.62T_1$, ductility at a strain rate 0.1 s^{-1} is much lower than strain rate 1 s^{-1}.

The effects of parameters on the post-form strength are:

- T4 material and as-quenched material has no obvious difference, whilst the samples formed from T6 temper have much lower strength;
- Heating rate has a positive effect on strength before it achieves the

critical heating rate. Thereafter, there is no difference if heating rate is greater than the critical value. The critical heating rate is a function of forming temperature, and a higher temperature requires higher critical heating rate. When the sample is formed above $0.69T_1$, heating rate does not affect the post-form strength;

- Forming temperature is important for post-form strength. When it is lower than $0.57T_1$ or higher than $0.69T_1$, the peak aged samples have a strength very close to T6 temper. The strength reduces below $0.57T_1$ and increase again from $0.62T_1$ and above. The gap between highest and lowest post-form hardness values as function of forming temperature increases with slower heating rate;
- Quenching rate has a similar effect with heating rate, which is positively correlated to the strength. The critical quenching rate increases with increasing forming temperature;
- Incubation temperature ranges from $0.38T_1$ to $0.41T_1$, and the incubation times have a positive effect on post form strength and peak aged strength. High post-form strength can be achieved with paint bake temperatures in the range $0.43T_1$ to $0.46T_1$, with the strength increasing as paint bake time increases. The longer incubation time reduces the critical paint bake time required for peak ageing;
- Double stage ageing tests and incubation plus paint bake tests share very similar results, which means the double ageing tests could be applied for other aluminium alloys to predict the incubation and paint bake temperature and time effects;
- Incubation depresses the natural ageing effects on the post-form strength. With $0.03t_1$ only incubation, natural ageing effect on the peak aged strength and paint bake time is negligible.

There are 6 main advantages of the FAST process: high post form strength, high shape complexity, high production rate, secondary fabrication availability, negligible natural ageing effect and customised forming parameters.

M-shape and U-shape forming tests were conducted following the optimal conditions determined from the ductility and strength tests. Components were successfully formed at all temperatures at $0.57T_1$, $0.62T_1$ and $0.69T_1$ with high strength for M-shape, and it was formed at $0.57T_1$ and $0.69T_1$ for U-shape. The FAST was proved to work well for forming AA7075 blank with high ductility and high post-form strength.

Chapter 6

Standard test procedures

6.1 Test procedures

The development of the FAST process has been demonstrated in Chapter 5. However, the forming parameters selected for the process vary depending on material supplier, component shape, heating methods, press machines, required post-form strengths and paint bake cycles. Materials from different batches or suppliers require modified forming parameters due to differences in chemical composition. Moreover, components of varying complexity require specific material ductility's, as well as a tailored die closing force on the blank to ensure quenching rate consistency throughout the component. In addition, the choice of heating method affects heating rate; a press machine affects die closing force; and post form strength and paint bake cycle requirements affect the incubation time and temperature. Therefore, a standard test procedure is required to determine and customise forming parameters to each manufacturers' requirements.

As can be seen in Figure 6.1, there are four main steps to tailor the FAST parameters to meet specific requirements: (i) requirements confirmation, (ii) condition inventory, (iii) material tests and (iv) verification tests. The first step is to communicate with the manufacturer in order to confirm the requirements. This includes, but is not limited to, component shape complexity, post-form strength and full forming cycle length. The second step is to confirm the forming conditions with the manufacturer, such as heating method and heating rate, die closing force of the press machine, die material and paint bake cycles. Thirdly, material tests are performed to determine all the forming parameters, as described in subsequent sections of this Chapter. Finally, verification tests are conducted. This involves the use of the hot stamping simulator and lab-scale UNI-form automated production line.

Figure 6.1 Standard test procedure.

The first step is to confirm the requirements from the manufacturer. The three main requirements to specify the forming parameters include: ductility, strength and time. Ductility enables the complexity of the component to be determined, and verified through FE model simulations. As discussed in Chapter 5, forming temperature has a significant effect on true strain at failure, and thus an appropriate forming temperature range can be allocated to meet ductility requirements. Strength specifically refers to the post form strength requirement, which is affected by a combination of all forming parameters. Time is the longest time acceptable for the manufacturer to perform each forming cycle and incubation process.

The second step requires the recording of all manufacturing and equipment capabilities including heating rate, stamping speed, die closing force, die material, and paint bake cycle details. IHTC tests will be performed to generate the relation between the tool material and blank material following the test procedures in Chapter 4, and the results will be implemented into FE models to simulate tests for the quenching behaviour during stamping and quenching. The limitations of this equipment will influence the customisation of forming parameters. Should the manufacturing equipment be unable to meet the minimum requirements for the FAST process, then it may not be possible to form components with this process. In this case improvement advice will be offered.

The critical heating rate requirements for full post-form strength vary with target temperature. Stamping speed is related to strain rate during forming, and the die closing force and is related to the pressure influencing the cooling rate as presented in Chapter 5. Paint bake cycle time and temperature could affect the incubation time to achieve the required strength, with paint bake temperature requirements varying depending on the location of the component in the vehicle body-in-white.

Laboratory tests conducted in the third stage include: ageing tests, tensile tests, forming temperature tests, heating rate tests, and quenching rate tests. As concluded from the test results of Chapter 5, double stage ageing results could be used to predict the strength performance of the formed component after incubation and paint bake cycles. Tensile tests are performed at a range of forming temperatures to find the temperature range for the required ductility, and the results are also implemented into FE models after all material tests. Forming temperature tests are taken to find the temperature range that meets the required strength. Quenching rate and heating rate tests aim for indicating the critical heating and quenching rates to generate the peak post-form strength. FE models are established based on the IHTC test results and material test results, to simulate the quenching rates. If the quenching rate in some areas of the blank is lower than the critical value, improvements are provided. If the quenching rates are greater than the critical value through all the blank area, the quenching time to be cooled to the upper limit of incubation temperature is set as a forming parameter.

Finally as the fourth stage, verification tests are performed at lab scale using the hot stamping simulator M-shape forming tool and the UNI-form U-shape forming test-rig. The forming tests verify the forming parameters as determined throughout stages one to three.

6.2 Case study

Six demonstrator cases were studied using the hot stamping simulator and UNI-form test-rig. Cases 1-3 were performed on the hot stamping simulator, with cases 4-6 performed on the UNI-form test-rig. All four test procedure steps were taken to optimise forming parameters. A new batch of AA7075-2 mm blank and a different type of tool material (H13) from the tests in Chapter 5 were used in the case study to demonstrate the optimisation process. Both the specimen and tool materials were supplied by a manufacturer and the chemical compositions were unknown. The yield strength of the new T6 temper AA7075 blanks was 491.5 MPa and the ultimate tensile strength 622 MPa, with the hardness of T6 temper being 196 Hv. The paint bake cycle temperature and time profiles were provided by an automotive manufacturer, and due to a confidentiality agreement, specific details regarding temperature, time and cycle numbers are not presented in this study.

6.2.1 Requirements confirmation

The six test cases were designed based on the requirements from a manufacturer, which supplied the specimens and tools. The 3 cases using the hot stamping simulator shared the same post-form requirements as those of the UNI-form such as elongation and hardness. For example, case 1 had same requirements as case 4, case 2 with case 5, and case 3 with case 6.

Shown as Table 6.1, test cases 1 and 4 were simulated as being components of high shape complexity shape and strength, requiring 0.9 true strain at failure and at least 90% of T6 hardness. There was no upper limit required for incubation and cycle time. Cases 2 and 5 simulated components with less shape complexity but of high strength. A true strain of 0.4 was tested for these two cases, with a post-form hardness of 90% of T6 temper. As was the case for 1 and 4, there was no specific incubation and cycle time requirement for cases 2 and 5. Cases 3 and 6 represented components with simple shape and short forming cycle, requiring 0.4 true strain with maximum $0.04t_1$ incubation, and 80% hardness of T6 temper.

Table 6.1 *Test Case Requirements.*

Case No.	Shape	True strain	Hardness (% of T6)	Incubation time (/t_1)
1	M-shape	0.9	90	NA
2	M-shape	0.4	90	NA
3	M-shape	0.4	80	$0.04t_1$
4	U-shape	0.9	90	NA
5	U-shape	0.4	90	NA
6	U-shape	0.4	80	$0.04t_1$

6.2.2 Conditions inventory

M-shape tests

Forming tests for Cases 1-3 were conducted on the hot stamping simulator using the M-shape forming tools to determine the IHTC values, as was performed in Chapter 5. The maximum heating rate that can be achieved is approximate $1.1R_1$ at $0.77T_1$ forming temperature. The available stamping speed can be varied from 1 mm/s to a theoretical 1000 mm/s, although a maximum of 400 mm/s was selected in the tests to achieve the production rate of the U-shape forming tests. The die closing pressure of the hot stamping simulator was varied up to 20 MPa. Tests were conducted to determine the IHTC values between the new tool material and workpiece at fully lubricated condition using Omega-35 as per Chapter 4, enabling the IHTC values as a function of pressure to be recorded, as shown in Figure 4.3(a).

U-shape tests

Conductive heating tests for Cases 4-6 were performed on the UNI-form pilot production line to generate the blank heating curve. The speed of the press was set to its highest speed of 400 mm/s, with the gas springs fully charged to 30 bar to provide a die closing pressure of 14 MPa. The highest heater working temperature was $0.83T_1$, and the maximum heating rate that could be achieved was approximately $1R_1$ from room temperature to $0.57T_1$ and $0.54R_1$ up to $0.77T_1$. The die material used in the U-shape tests was the same as that in M-shape tests, and therefore the IHTC tests results from M-shape forming tests could be applied to the U-shape forming tests.

6.2.3 Material tests

The tests conducted on the new tooling and blank material were ageing tests, tensile tests, forming temperature tests, heating rate tests, and quenching rate tests. All samples were fully solution heat treated and water quenched prior to the tests, to ensure that as quenched samples were used in ageing tests and T4 samples were used in the remaining tests as is the case in FAST.

Ageing tests

Both single stage and double stage ageing tests using as quenched samples were conducted to simulate incubation temperature and time. The single stage ageing tests were taken at $0.39T_1$ for the time length from $0.04t_1$ to $36t_1$ as shown in Figure 6.2, where the single stage ageing hardness reached a peak value of 196 Hv after $12t_1$.

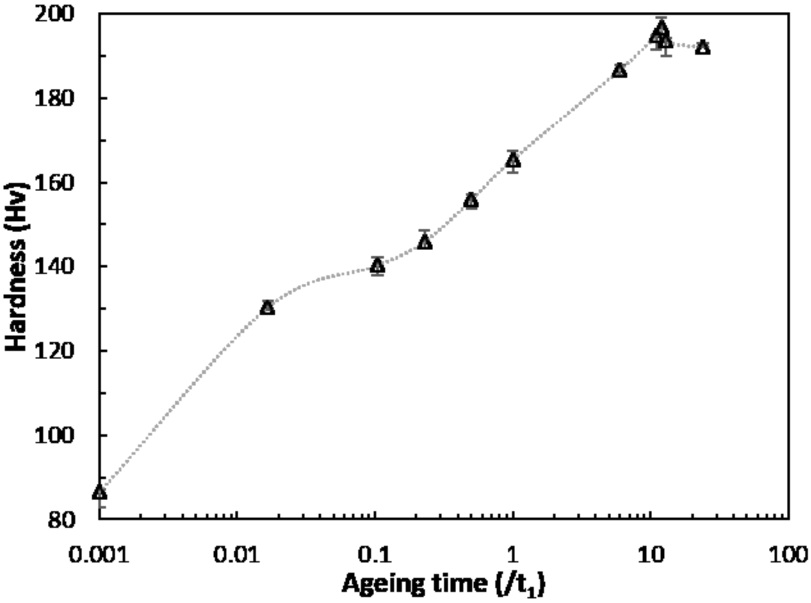

Figure 6.2 Single stage ageing results.

As discussed in Chapter 5, double stage ageing hardness results were similar to the FAST and paint bake processes, and was thus used to predict the post form strength. The second stage ageing parameters were the same as those paint bake cycles provided by the manufacturer, and were kept constant in all tests. The temperature of first stage ageing representing incubation ranged from $0.35T_1$ to $0.44T_1$ and the time was $0.04t_1$ to $2t_1$.

Figure 6.3(a) shows the hardness evolution with first stage ageing time for the temperatures $0.38T_1$, $0.39T_1$ and $0.42T_1$. It can be seen that the peak hardness value is higher at the lowest temperature, although it takes longer to achieve this peak value. The trend is similar to those seen from Chapter 5. Figure 6.3(b) shows the hardness with $0.04t_1$ first stage ageing time at different temperatures and peak hardness. The incubation temperature to maintain the full post-form hardness is $0.38T_1$-$0.42T_1$ for this material, and the hardness with $0.04t_1$ first stage ageing increases with higher temperature within the temperature range, although the difference is small. The peak value with these temperatures decreases with increasing temperature.

Cases 1,2,4,5 require 90% or greater hardness values of T6 temper, or a value of 176 Hv regardless of the incubation time. Therefore, the incubation process for these 4 cases should be between $0.38T_1$ and $0.42T_1$ with incubation time serving the peak hardness values at the temperature. In typical manufacturing operations, the artificial ageing process is conducted in large furnaces, and the temperature accuracy is not very high. To avoid the temperature being out of the range during incubation, a $0.1T_1$ margin of error is advised to be added to both the upper and lower bounds, resulting in a temperature window of $0.39T_1$ to $0.40T_1$. As shown in Figure 6.3(a), the incubation time required to achieve peak hardness reduces with increasing temperature, and therefore $0.3t_1$ at $0.39T_1$, is the recommended temperature profile achieving a hardness value of 193 Hv, or 98% of T6 temper. Cases 3 and 6 were evaluated with the restriction of $0.04t_1$ incubation time. For a temperature of $0.39T_1$ for $0.04t_1$, the hardness value achieved was 179 Hv, or 91% of T6 temper.

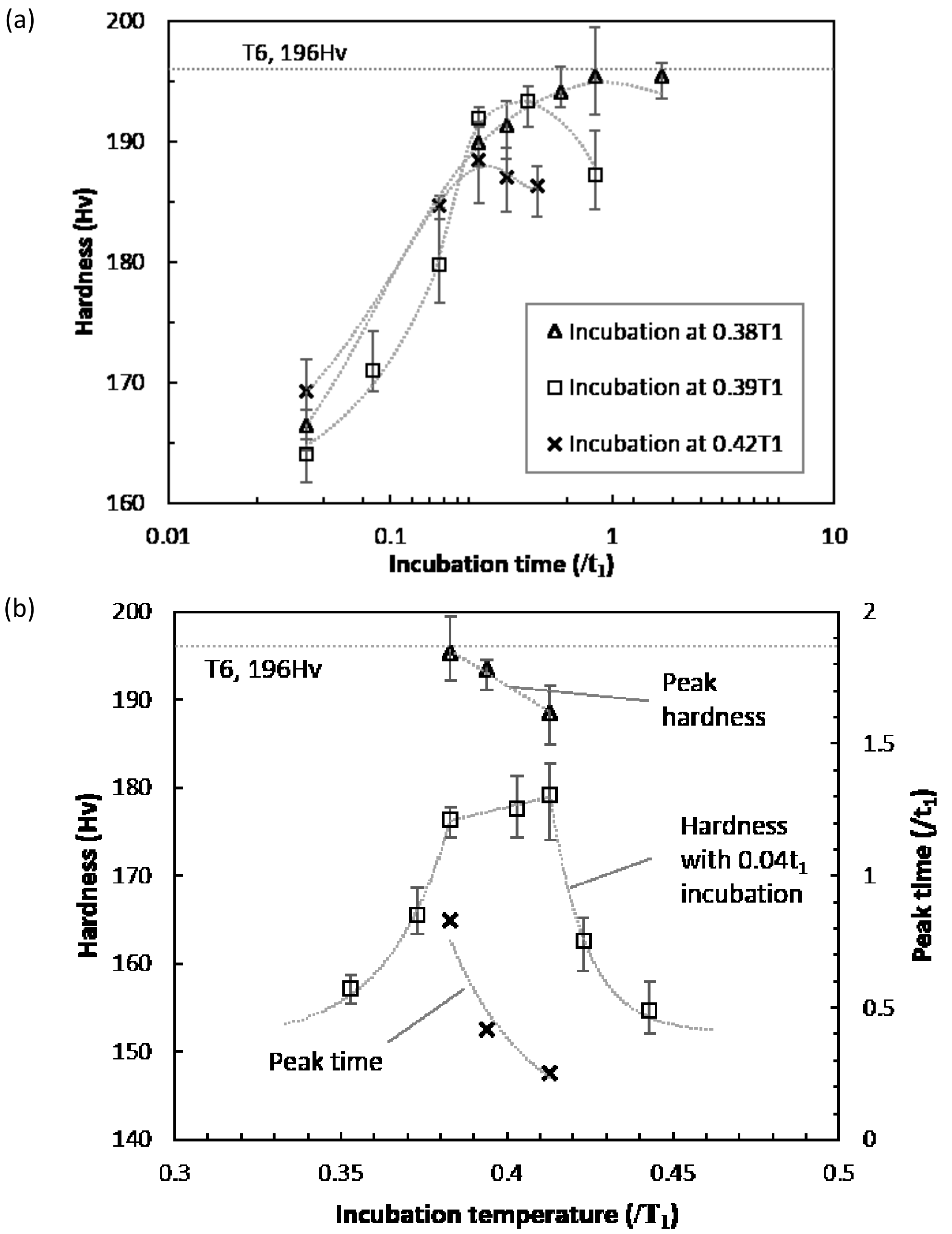

Figure 6.3 *(a) Hardness with different incubation period at 0.38T_1, 0.39T_1 and 0.42T_1; (b) hardness with 0.04t_1 incubation at different temperatures and, peak hardness at different temperatures and time.*

Tensile tests

From FE simulation results obtained by big data analysis(Wang et al., 2016), the strain rate of U-shape and M-shape forming tests is mainly distributing around 1 s^{-1}, and thus this was the value selected for the tests. The forming temperatures evaluated were in the range of 0.47T_1 to 0.77T_1. The true strain at failure for different temperatures are shown in Figure 6.4. It is seen from the figure that the true strain at failure is 0.2 at 0.47T_1 and slowly increases to 0.47 at 0.57T_1, after which it starts to climb rapidly to its peak value 0.92 at 0.65T_1 before dropping to 0.4 at 0.72T_1. The trend reduces further to 0.1 at 0.77T_1. It is seen that the peak temperature is 0.65T_1, which is lower than the material tested in Chapter 5 which was 0.69T_1. The reason for this could be the variation in chemical composition, which highlights the importance of evaluating materials from different batches.

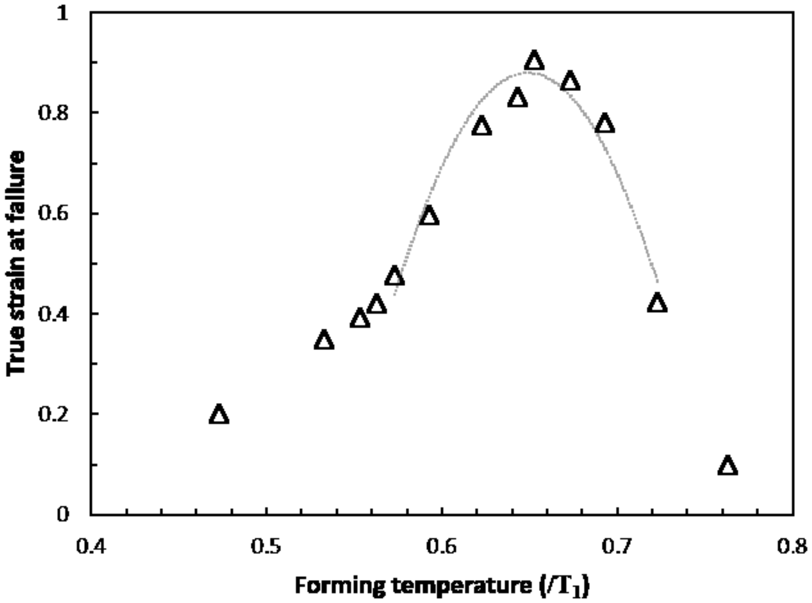

Figure 6.4 Effect of forming temperature on true strain at failure for strain rate 1 s^{-1}.

The requirement of true strain at failure for cases 1 and 4 is 0.9, while the temperature range to meet the requirement is 0.65T_1. The true strain requirement for cases 2, 3, 5 and 6 is 0.4, and the corresponding forming temperature is 0.57T_1 to 0.72T_1. The forming temperature selected for each case depends on the ductility, strength, efficiency and energy cost requirements.

Forming temperature tests

Forming temperature tests were conducted at: High heating rate, 14 MPa quenching pressure, 0.04t_1/0.3t_1 incubation time at 0.39T_1, and paint bake. The target forming temperature was evaluated between 0.47T_1 to 0.77T_1. The 0.3t_1 incubation tests were conducted for cases 1, 2, 4 and 5 to achieve full post-form hardness, while the 0.04t_1 incubation tests were used to meet the maximum acceptable incubation time for cases 3 and 6.

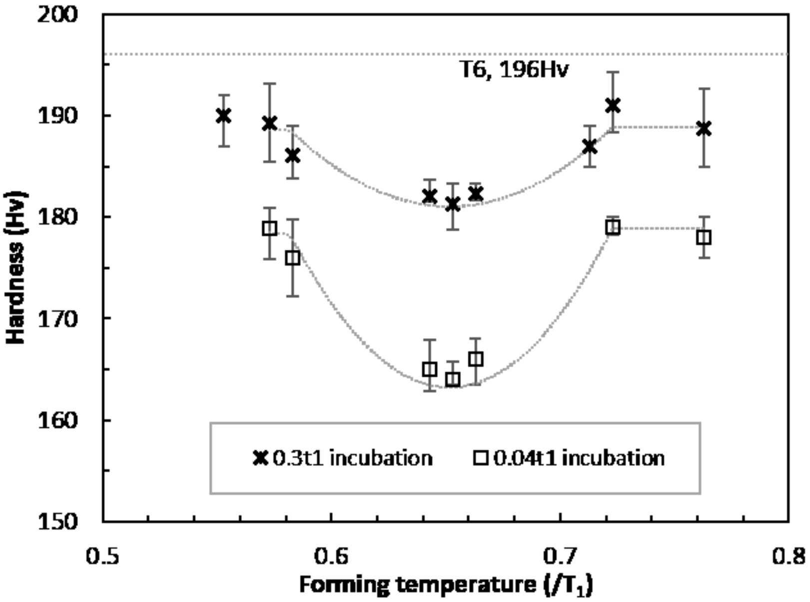

Figure 6.5 Post-form hardness formed at different temperatures with $0.3t_1$ and $0.04t_1$ incubation.

The results of hardness against forming temperature are shown in Figure 6.5. It is seen that when compared to the material grade evaluated in Chapter 5, the forming temperature for the lowest post-form strength in these tests occurred at $0.65T_1$, which was $0.3T_1$ higher than in Chapter 5, while still sharing the same overall trend with the previous material. However, the trend is similar to that in Chapter 5 tests, where the hardness also reduced from $0.57T_1$, and reached a minimum at $0.65T_1$, followed by an increase until $0.72T_1$. The hardness values were similar in the temperature range $0.72T_1$ to $0.77T_1$. As shown in the figure, the hardness value at $0.65T_1$ was slightly lower than the peak value at $0.72T_1$. The post-form hardness of the specimen formed at $0.65T_1$ was 164 Hv with $0.04t_1$ incubation and 181 Hv with $0.3t_1$ incubation, which were 15 Hv and 8 Hv lower than those formed at $0.72T_1$.

Cases 1, 2, 4 and 5 required a hardness of 90% of T6 temper. As discussed earlier, the temperature range for cases 1 and 4 to achieve adequate ductility is $0.65T_1$, and the temperature range for cases 2, 3, 5 and 6 was $0.57T_1$ to $0.72T_1$. In consideration of efficiency and energy cost, the lowest acceptable temperature of $0.57T_1$ was selected for cases 2 and 5. The hardness requirement for case 3 and 6 was 80% of T6 temper (164 Hv) with $0.04t_1$ incubation, and thus the forming temperature should be less than $0.57T_1$ or greater than $0.72T_1$. In conjunction with the ductility requirement, the effective temperatures for cases 3 and 6 are $0.57T_1$ and $0.72T_1$ respectively. Taking efficiency and energy cost into consideration,

$0.57T_1$ was selected as the forming temperature. The expected hardness for cases 1 and 4 was therefore 181 Hv, and for cases 2&5 and 3&6 were 189 Hv and 179 Hv.

Heating rate tests

As discussed in Chapter 5, each forming temperature requires a specific critical heating rate to achieve the optimised post-form strength. The overall trend is that the higher temperature requires higher heating rate until reaching a peak. For this batch of material, the turning point is at $0.72T_1$, and therefore the critical heating rate increases with increasing temperature until $0.72T_1$. Tests were conducted at two forming temperatures ($0.57T_1$ and $0.65T_1$) with $0.04t_1$ and $0.3t_1$ incubation, and the results are shown in Figure 6.6. The critical heating rate is $0.11R_1$ at $0.57T_1$ forming temperature and $0.27R_1$ at $0.65T_1$ forming temperature.

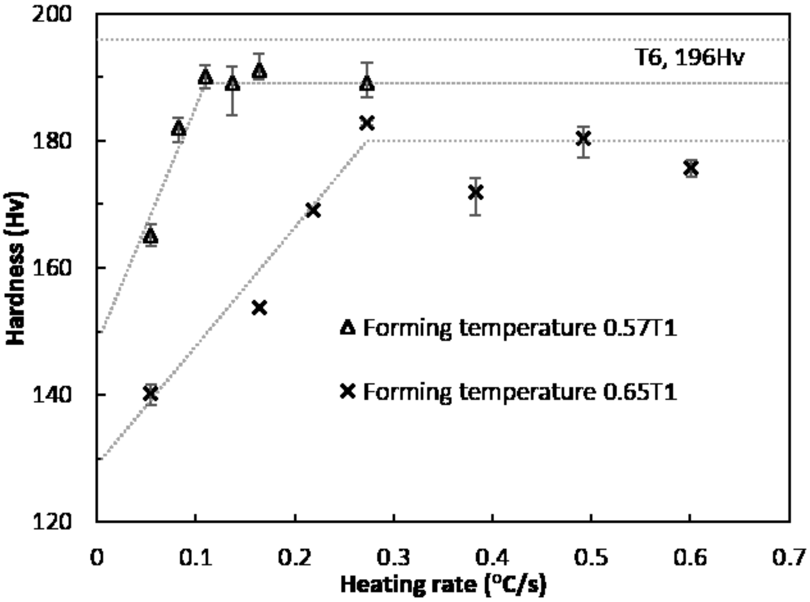

Figure 6.6 *Post-form hardness with different heating rates formed at $0.57T_1$ and $0.65T_1$.*

The forming temperature for case 1 was $0.65T_1$, and the critical heating rate was $0.27R_1$. Cases 2 and 3 required critical heating rates of $0.11R_1$ at $0.57T_1$. The maximum heating rate that could be achieved in the hot stamping simulator was 200°C/s, which was significantly greater than the critical values required in cases 1-3. As discussed above, the required post-form hardness of 176 Hv for case 4 could not be met with the UNI-form regardless of heating rate. Forming temperature for cases 5 and 6 were $0.57T_1$ with a critical heating rate of $0.11R_1$. The heating rates achieved by UNI-form at $0.57T_1$ and $0.65T_1$ forming temperature were $1R_1$ and $0.81R_1$ with the heater set to $0.83T_1$. According to the heating curve of $0.83T_1$ heater temperature, it took 1.5s to heat the blank to $0.57T_1$ from room temperature, and 2.5s to heat it to $0.65T_1$.

Quenching rate tests

As pressure varies throughout the blank during stamping and quenching, the quenching rate would also vary. In order to achieve the optimised post-form strength, the quenching rate at any point of the blank should be higher than its critical value and the end temperature of quenching process should be lower than the upper limit of the incubation temperature. Critical quenching rates at each target forming temperature were tested for all cases by using the quenching rate test setup of Chapter 5. Afterwards the IHTC value between the new die and blank materials as a function of pressure were determined using the hot stamping simulator, and the results were imported into FE models for both M-shape and U-shape forming to simulate the temperature evolutions of blanks during stamping and quenching. Simulation results were compared to the critical values.

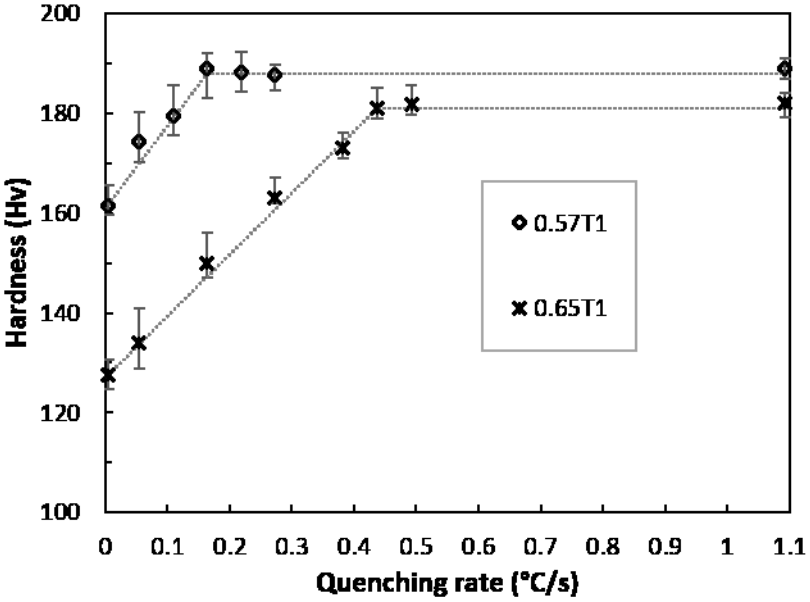

Figure 6.7 *Quenching rate test results.*

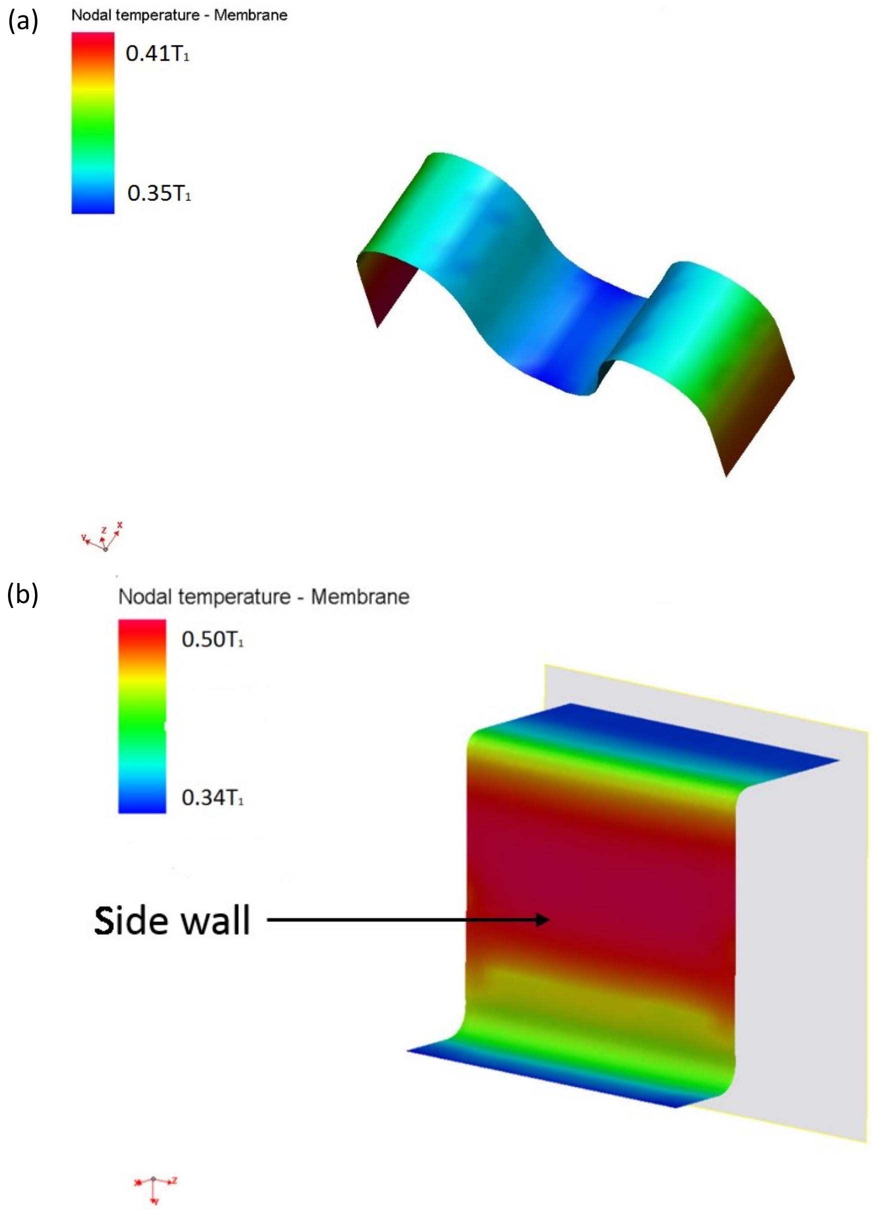

Figure 6.8 *Blank temperature distributions formed and quenched from 0.57T$_1$: (a) M-shape after 1.0s stamping and quenching; (b) U-shape after 1.6s stamping and quenching; simulated in PAM-STAMP 2.0.*

The post-form hardness with quenching rates at target temperatures 0.57T$_1$ and 0.65T$_1$ were tested, and the results are shown in Figure 6.7. The critical quenching rate is 0.16R$_1$ for 0.57T$_1$ and 0.35R$_1$ for 0.65T$_1$. IHTC tests were taken with fully lubricated condition, i.e. the lubricant amount was more than the critical amount for peak IHTC value and would not further improve the IHTC value with additional lubricant. The IHTC value as a function of contact pressure is shown in Figure 4.3(a), and the FE models after 1.0s stamping and quenching from 0.57T$_1$ for M-shape and 1.6s for U-shape forming are shown in Figure 6.8(a) and (b). Simulations quenching from 0.65T$_1$ were also performed. The quenching rates at all areas of the M-shape samples and on most areas of U-shape samples were confirmed to be higher than the critical values. However, the quenching rate on the side walls of the U-shape component was approximately $0.19R_1$ when quenched from $0.65T_1$ and $0.13R_1$ from $0.57T_1$ to $0.42T_1$, which were lower than the critical quenching rates of $0.44R_1$ and $0.16R_1$. The reason was that the vertical side wall of the tool lead to low pressure on the blank. The hardness of side walls was therefore expected to be lower than the requirements. The quenching times generated from FE simulations for each case to cool down to a temperature lower than $0.42T_1$, the upper limit of the incubation temperature, are shown in Table 6.2.

Table 6.2 *FE simulation results of stamping and quenching time to cool blank below* $0.42T_1$*.*

Case No.	1	2	3	4	5	6
Quenching time (s)	1.4	1.0	1.0	1.8	1.6	1.6

To conclude, all the determined forming parameters and expected hardness values are shown in Table 6.3. The cycle times including heating, stamping and quenching are also listed in the table. Cases 1, 2, 3 are expected to be formed successfully, meeting all requirements whereas cases 4, 5 and 6 would be mostly successful with the exception of the side walls. It is seen that the shortest cycle time that can be achieved with FAST is 2.9 second per component including heating, stamping and quenching, while the highest possible hardness that can be achieved was 189 Hv, or 96% of T6 temper.

Table 6.3 *Forming parameters and expected true strain at failure, time and hardness. (Hardness does not include side walls for cases 4, 5 & 6).*

Case No.	1	2	3	4	5	6
Shape	M-shape	M-shape	M-shape	U-shape	U-shape	U-shape
Heating time (s)	2.4	1.9	1.9	2.5	1.5	1.5
Forming temperature (/T_1)	0.65	0.57	0.57	0.65	0.57	0.57
True strain at failure	0.92	0.47	0.47	0.92	0.47	0.47
Stamping speed (mm/s)	400	400	400	400	400	400
Stamping and quenching time (s)	1.4	1.0	1.0	1.8	1.6	1.6
Incubation temperature (/T_1)	0.39-0.40	0.39-0.40	0.39-0.40	0.39-0.40	0.39-0.40	0.39-0.40
Incubation time (/t_1)	0.3	0.3	0.04	0.3	0.3	0.04
Cycle time (s)	3.8	2.9	2.9	4.3	3.1	3.1
Post-form hardness (Hv)	181	189	179	178	184	173
Post-form hardness (% of T6)	92	96	91	91	94	88

Tests were conducted in the hot stamping simulator with flat tools following all the parameters in Table 6.3 to simulate the forming cases. Tensile tests were conducted after paint bake to evaluate the yield strength values of the formed samples. The yield strength values were 450 MPa, 465 MPa, 445 MPa, 440 MPa, 455 MPa and 430 MPa for the samples with forming parameters from case 1 to case 6 respectively.

6.2.4 Verification tests

The cases 1-3 were subsequently formed using M-shape forming tools, with cases 4-6 formed in UNI-form with U-shape tools. The parameters in Table 6.3 were applied in every case. The formed components are shown in Figure 6.9, and the average hardness values were very close to the predicted values with less than 2% difference. Therefore the components required in all cases were successfully formed (exc. side walls in cases 4, 5 and 6). The hardness values on the side walls were lower than the required values, therefore requiring the tool to be re-designed to apply higher pressure on the side wall area.

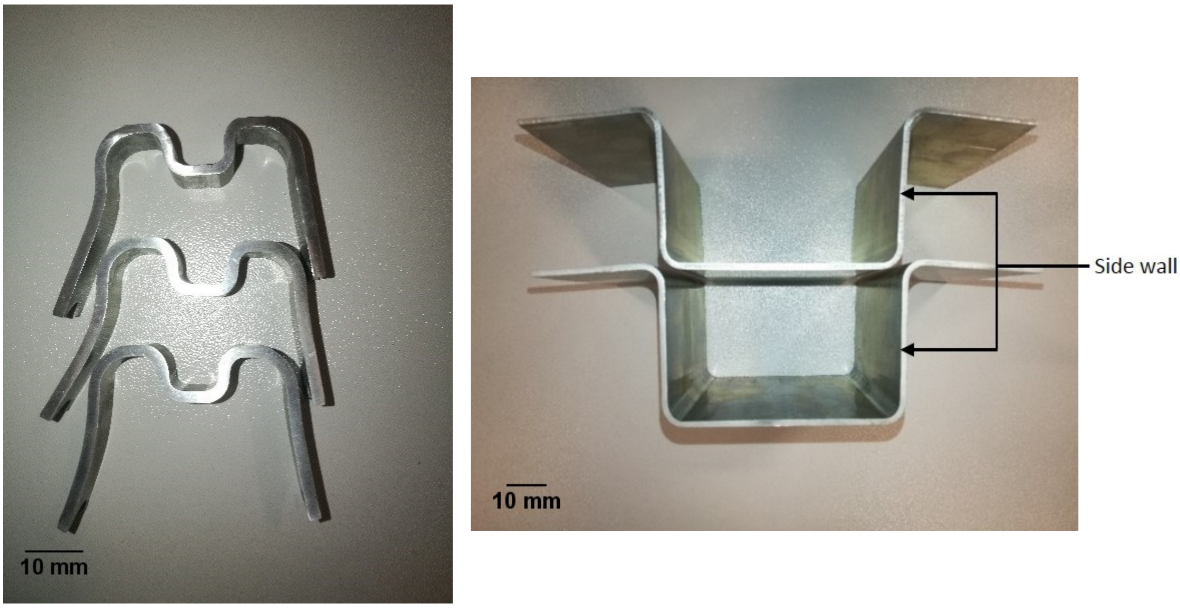

(a) (b)

Figure 6.9 *(a) formed M-shape components; (b) formed U-shape components.*

6.3 Conclusion

In this chapter, a standard test procedure was designed to customise the forming parameters for different materials, shapes and production lines. There are 4 steps in the procedure: requirements confirmation, condition inventory, material tests and verification tests. Material tests followed the sequence of: ageing tests, tensile tests, forming temperature tests, heating rate tests, and quenching rate tests.

Six demonstrator cases were studied following the procedure for 3 M-shape forming tests and 3 U-shape forming tests. Components in cases 1-3 for M-shape forming tests were successfully formed with the parameters generated from the standard four-step test results and all requirements were met. Components in cases 4, 5 and 6 were partly successful and most areas on the components met the required hardness. However, the side wall area did not achieve the adequate hardness. It was suggested that the forming tools be re-designed to apply increased pressure on the side wall area to achieve higher quenching rate in U-shape forming.

Chapter 7

Final conclusion

This chapter presents a summary of the key findings of the thesis. In addition, recommendations for future work are made to extend the FAST process to industrial applications.

7.1 Key Findings

In order to form high and ultra-high strength complex-shaped thin wall components from aluminium alloy sheets, a novel forming technology FAST was developed in this thesis. To study this process, a hot stamping simulator was successfully developed and manufactured to operate in conjunction with the Gleeble 3800 thermo-mechanical testing machine. The effect of forming parameters on the formability of material and post-form strength have been studied for AA7075 2 mm blank, with verification tests being conducted using U-shape and M-shape forming tools. Interfacial heat transfer coefficient (IHTC) was also studied in order to calculate the quenching time, predict post form strength and optimise the tool design to secure a high quenching rate, enabling the material to retain the full post-form strength. A standard test procedure was designed for different materials and manufacturers, with 6 cases studied.

The Hot stamping simulator consisted of 4 main components: a slider, a workpiece support, left and right dies, and left and right grips. The Hot stamping simulator enabled high heating rate up to 200°C/s, high stamping speed up to 1000 mm/s, high die closing pressure exceeding 20 MPa, reversibly moveable, high control accuracy, convenience of changing punch/die and workpiece, ease of applying and cleaning lubricant, and high complexity of temperature, stroke moving and force evolution. This enabled the FAST tests to be conducted as well as other stamping processes.

The IHTC values were determined by comparing the temperature evolution curve from quenching tests using the Hot stamping simulator and FE simulations in PAM-STAMP FE commercial software. The effects of contact pressure, lubricant, and tool material on the IHTC value have been studied. A positive correlation between the IHTC value and contact pressure was found under both dry and lubricated conditions while using tool steels. Omega-35 graphite-based lubricant proved beneficial to the heat transfer between the specimen and tools during hot stamping. This effect reached a limiting value at a lubricant layer thickness of 0.015 mm, beyond which the IHTC formed a plateau. Thermal conductivity of tool material was proved to have a positive correlation with IHTC value when other conditions remained unchanged. An IHTC prediction model was developed based on the results generated from experiments and FE simulations as a function of contact pressure, lubricant and tool material. The model was verified using tool 3 in the hot stamping simulator and hot stamping trials of hemispherical dome and B pillar. The model was able to predict the IHTC values between different specimens and dies under different pressures and lubricating conditions during the hot stamping process.

The FAST process has been successfully developed, and the process consists of: rapid heating, forming and in-die quenching, and incubation. The material is then placed into storage awaiting the second stage which consists of secondary fabrications and paint bake. The effects of main parameters on the ductility and post-form strength were studied. The effects on ductility are:

- Heating rate and material temper do not have obvious effects on ductility;
- Forming temperature has a positive effect on ductility below its peak temperature (0.69T_1 for the AA7075 blank tested in Chapter 5, 0.62T_1 for that in Chapter 6), and becomes negative above the peak temperature;
- Strain rate is negatively related to ductility below 0.62T_1, and when it is above 0.62T_1, ductility at a strain rate 0.1 s^{-1} is much lower than strain rate 1 s^{-1}. The turning temperature may vary for different materials.

The effects of parameters on the post-form strength are:

- T4 material and as-quenched material has no obvious difference, whilst the samples formed from T6 temper have much lower strength;
- Heating rate has a positive effect on strength before it achieves the critical heating rate. Thereafter, there is no difference if heating rate is greater than the critical value. The critical heating rate is a function of forming temperature, and a higher temperature requires higher critical heating rate;
- Forming temperature is important for post-form strength. When it is lower

than $0.57T_1$ or higher than $0.69T_1$ ($0.62T_1$ for material tested in Chapter 6), the peak aged samples have a strength very close to T6 temper. The strength reduces below $0.57T_1$ and increase again from $0.62T_1$ ($0.65T_1$ in Chapter 6) and above. The gap between highest and lowest post-form hardness values as function of forming temperature increases with slower heating rate;

- Quenching rate has a similar effect with heating rate, which is positively correlated to the strength. The critical quenching rate increases with increasing forming temperature;
- Incubation temperature ranges from $0.38T_1$ to $0.41T_1$ ($0.38T_1$ to $0.42T_1$ for the material in Chapter 6), and the incubation times have a positive effect on post form strength and peak aged strength. High post-form strength can be achieved with paint bake temperatures in the range $0.44T_1$ to $0.46T_1$, with the strength increasing as paint bake time increases. The boundary temperatures for both incubation and paint bake are depending on different materials. The longer incubation time reduces the critical paint bake time required for peak ageing;

There are 6 main advantages of the FAST process: high post form strength, high shape complexity, high production rate, secondary fabrication availability, negligible natural ageing effect and customised forming parameters.

A standard test procedure was designed to customise the forming parameters for different materials, shapes and production lines. There are 4 steps in the procedure: requirements confirmation, condition inventory, material tests and verification tests. Material tests followed the sequence of: ageing tests, tensile tests, forming temperature tests, heating rate tests, and quenching rate tests.

Six demonstrator cases were studied following the procedure for 3 M-shape forming tests and 3 U-shape forming tests. Forming parameters have been generated following the stand test procedure, and all forming tests were successfully formed with these parameters. However, the side wall area did not achieve the adequate hardness in U-shape form cases. It was suggested that the forming tools be re-designed to apply increased pressure on the side wall area to achieve higher quenching rate in U-shape forming.

7.2 Future Work

The present work developed a novel forming technology Fast light alloy stamping technology (FAST) for forming high and ultra-high strength complex-shaped aluminium alloy thin-wall components. As a new process, there are several areas which can be investigated in future studies to improve the reliability and enable industrial adoption.

Further IHTC verification tests

IHTC model has been verified in lab scale forming tests for dome shape and B-pillar shape components. However, because thermocouple holes were drilled before stamping, it is highly risky for the blanks to break at the holes during stamping, therefore only one point on each component has been tested in verification experiments. It is suggested that more verification tests would be conducted with more test points at different locations on same blank to further verify the IHTC model.

Modelling

All significant forming parameters that affect the FAST process have been studied in the present work. However, it has also been found that the precise values of the forming parameters may vary with different materials or even different batches of AA7075. Thus a standard test procedure for FAST was developed and has determined that there are many experimental tests needed in order to generate the forming parameter data. Therefore, an important task in the future is the development of numerical models that can predict the forming parameters as a function of the materials' chemical compositions, and to also predict the ductility and post-form strength based on the different forming parameters. These models would significantly reduce the amount of experimental tests necessary to characterise the material and simplify the process for industrial application.

FAST formed component properties

The present work focused on successfully forming shapes of high complexity and post-form strength. However, there are other component properties that must be studied for industrial applications. It is suggested to further study the effects of forming parameters on fatigue resistance, corrosion resistance, dimensional accuracy and microstructure stability of the formed components to ensure they meet industrial requirements.

Other materials

In the present work, ultra-high strength automotive aluminium alloy AA7075 was the focus of study. For industrial applications, it is recommended to expand the application of FAST process to other sheet formed materials, such as AA6xxx, AA2xxx, and other AA7xxx blanks.

Full scale industrial component testing

As a development study, FAST in the current study was applied on the laboratory scale UNI-form production system which has produced parts of limited size. It is recommended that forming tests are conducted for actual scale production components such as a B-Pillar or door inner, to enable post-form strength and dimensional accuracy variations to be compared to the laboratory scale components.

Reference list

A UNGUREANU, C., DAS, S. & JAWAHIR, I. S. (2007). Life-cycle Cost Analysis: Aluminum versus Steel in Passenger Cars.

ARDELL, A. J. (1972). The effect of volume fraction on particle coarsening: theoretical considerations. *Acta Metallurgica,* 20**,** 61-71.

BAI, Q., LIN, J., ZHAN, L., DEAN, T. A., BALINT, D. S. & ZHANG, Z. (2012). An efficient closed-form method for determining interfacial heat transfer coefficient in metal forming. *International Journal of Machine Tools and Manufacture,* 56**,** 102-110.

BARNES, A. J. (2007). Superplastic Forming 40 Years and Still Growing. *Journal of Materials Engineering and Performance,* 16**,** 440-454.

BERG, L. K., GJØNNES, J., HANSEN, V., LI, X. Z., KNUTSON-WEDEL, M., WATERLOO, G., SCHRYVERS, D. & WALLENBERG, L. R. (2001). GP-zones in Al–Zn–Mg alloys and their role in artificial aging. *Acta Materialia,* 49**,** 3443-3451.

BILLUR, E. (2017). 12 - Hot formed steels*,**. *Automotive Steels.* Woodhead Publishing.

BOSETTI, P., BRUSCHI, S., STOEHR, T., LECHLER, J. & MERKLEIN, M. (2010). Interlaboratory comparison for heat transfer coefficient identification in hot stamping of high strength steels. *International Journal of Material Forming,* 3**,** 817-820.

BUCHNER, B., BUCHNER, M. & BUCHMAYR, B. (2009). Determination of the real contact area for numerical simulation. *Tribology International,* 42**,** 897-901.

CAMPBELL, F. C. (2006). Chapter 2 - Aluminum. *Manufacturing Technology for Aerospace Structural Materials.* Oxford: Elsevier Science.

ÇETINKALE, T. N. & FISHENDEN, M. (1951) Published. Thermal Conductance of Metal Surfaces in Contact. International Conference of Heat Transfer, Institute of Mechanical Engineers, 1951. 271–275.

CHANG, C. C. & BRAMLEY, A. N. (2002). Determination of the heat transfer coefficient at the workpiece—die interface for the forging process. *Proceedings of the Institution of Mechanical Engineers, Part B: Journal of Engineering Manufacture,* 216**,** 1179-1186.

CHANG, Y., TANG, X., ZHAO, K., HU, P. & WU, Y. (2016). Investigation of the factors influencing the interfacial heat transfer coefficient in hot stamping. *Journal of Materials Processing Technology,* 228**,** 25-33.

COLE, G. S. & SHERMAN, A. M. (1995). Light weight materials for automotive applications. *Materials Characterization,* 35**,** 3-9.

COOPER, M. G., MIKIC, B. B. & YOVANOVICH, M. M. (1969). Thermal contact conductance. *International Journal of Heat and Mass Transfer,* 12**,** 279-300.

DE MOOR, E. & SPEER, J. G. (2017). 10 - Bainitic and quenching and partitioning steels. *Automotive Steels.* Woodhead Publishing.

DYNAMIC SYSTEMS INC. (2015). *Gleeble Systems* [Online]. Available: http://gleeble.com/products/products-overview.html [Accessed 08th August 2016].

ELFAKIR, O. (2015). Studies on the solution heat treatment, forming and in-die quenching process in the production of lightweight alloy components. Doctor of Philosophy PhD thesis.

EMANI, S. V., BENEDYK, J., NASH, P. & CHEN, D. (2009). Double aging and thermomechanical heat treatment of AA7075 aluminum alloy extrusions. *Journal of Materials Science,* 44**,** 6384-6391.

ESMAEILI, S., LLOYD, D. J. & POOLE, W. J. (2003a). Modeling of precipitation hardening for the naturally aged Al-Mg-Si-Cu alloy AA6111. *Acta Materialia,* 51**,** 3467-3481.

ESMAEILI, S., LLOYD, D. J. & POOLE, W. J. (2003b). A yield strength model for the Al-Mg-Si-Cu alloy AA6111. *Acta Materialia,* 51**,** 2243-2257.

FAKIR, O. E., WANG, L., BALINT, D., DEAR, J. P. & LIN, J. (2014). Predicting Effect of Temperature, Strain Rate and Strain Path Changes on Forming Limit of Lightweight Sheet Metal Alloys. *Procedia Engineering,* 81**,** 736-741.

FOSTER, A. D., MOHAMED, M. S., LIN, J. & DEAN, T. A. (2008). An investigation of lubrication and heat transfer for a sheet aluminium heat, form-quench (HFQ) process. *Steel Research International* 79.

GARRETT, R. P., LIN, J. & DEAN, T. A. (2005). Solution Heat Treatment and Cold Die Quenching in Forming AA 6xxx Sheet Components: Feasibility Study. *Advanced Materials Research,* 6-8**,** 673-680.

HALL, J. N. & FEKETE, J. R. (2017). 2 - Steels for auto bodies: A general overview. *Automotive Steels.* Woodhead Publishing.

HATCH, J. E. (1984). Aluminum: Properties and Physical Metallurgy, Ohio, ASM International.

HEINZ, A., HASZLER, A., KEIDEL, C., MOLDENHAUER, S., BENEDICTUS, R. & MILLER, W. S. (2000). Recent development in aluminium alloys for aerospace applications. *Materials Science and Engineering: A,* 280**,** 102-107.

HÖLSCHER, H., SCHIRMEISEN, A. & SCHWARZ, U. D. (2008). Principles of atomic friction: from sticking atoms to superlubric sliding. *Philosophical Transactions of the Royal Society A: Mathematical, Physical and Engineering Sciences,* 366**,** 1383-1404.

HU, P., YING, L., LI, Y. & LIAO, Z. (2013). Effect of oxide scale on temperature-dependent interfacial heat transfer in hot stamping process. *Journal of Materials Processing Technology,* 213**,** 1475-1483.

HU, Z. M., BROOKS, J. W. & DEAN, T. A. (1998). The interfacial heat transfer coefficient in hot die forging of titanium alloy. *Proceedings of the Institution of Mechanical Engineers, Part C: Journal of Mechanical Engineering Science,* 212**,** 485-496.

HUNG, T.-H., TSAI, P.-W., CHEN, F.-K., HUANG, T.-B. & LIU, W.-L. (2014). Measurement of Heat Transfer Coefficient of Boron Steel in Hot Stamping. *Procedia Engineering,* 81**,** 1750-1755.

I. TAUB, A., KRAJEWSKI, P., LUO, A. & N. OWENS, J. (2007). Yesterday, today and tomorrow: The evolution of technology for materials processing over the last 50 years: The automotive example. *Journal of Metals,* 59**,** 48-57.

IMPERIAL COLLEGE LONDON. (2017). *Metal forming and materials modelling* [Online]. Available: http://www.imperial.ac.uk/metal-forming/ [Accessed 10 Nov 2017].

ISMAIL, A. & MOHAMED, M. S. (2016) Published. Review on sheet metal forming process of aluminium alloys. 2016/4/19 2016. 129-141.

JACOBSON, M. Z. (2008). Review of solutions to global warming, air pollution, and energy security. *Energy & Environmental Science,* 2, 148-173.

JAIN, V. K. (1990). Determination of heat transfer coefficient for forging applications. *Journal of Materials Shaping Technology,* 8, 193-202.

JI, K., LIU, X., ELFAKIR, O., LIU, J., ZHANG, Q. & WANG, L. (2016). Determination of the Interfacial Heat Transfer Coefficient in the Hot Stamping of AA7075.

JIANG, F.-L., ZHANG, H., WENG, S.-C. & FU, D.-F. (2016). Characterization of dynamic microstructural evolution of AA7150 aluminum alloy at high strain rate during hot deformation. *Transactions of Nonferrous Metals Society of China,* 26, 51-62.

KARBASIAN, H. & TEKKAYA, A. E. (2010). A review on hot stamping. *Journal of Materials Processing Technology,* 210, 2103-2118.

KASHYAP, K. T., RAMACHANDRA, C., CHATTERJI, B. & LELE, S. (2000). A model for two-step ageing. *Bulletin of Materials Science,* 23, 405-411.

LABUSCH, R. (1970). A Statistical Theory of Solid Solution Hardening. *physica status solidi (b),* 41, 659-669.

LEE, J.-M., LEE, I.-K., LEE, K.-H., KIM, D.-S. & KIM, B.-M. (2012). FEA technique of hot plate forming process using cell-typed die with cooling device. *Transactions of Nonferrous Metals Society of China,* 22, s831-s837.

LI, X. Z., HANSEN, V., GJØNNES, J. & WALLENBERG, L. R. (1999). HREM study and structure modeling of the η' phase, the hardening precipitates in commercial Al − Zn − Mg alloys. *Acta Materialia,* 47, 2651-2659.

LIM, S., NBSP, TAEK, EUN, I., NBSP, SANG, NAM, S., NBSP & WOO (2003). Control of Equilibrium Phases (M,T,S) in the Modified Aluminum Alloy 7175 for Thick Forging Applications. *MATERIALS TRANSACTIONS,* 44, 181-187.

LIN, J., DEAN, T. A., GARRETT, R. P. & FOSTER, A. D. (2009). Method for forming component of complex shape from aluminum-alloy sheet, involves quenching heated sheets between cold dies in solution and maintaining shape of sheet.

LIU, J., GAO, H., FAKIR, O. E., WANG, L. & LIN, J. (2015a). HFQ forming of AA6082 tailor welded blanks. *MATEC Web of Conferences,* 21, 05006.

LIU, S., LI, C., HAN, S., DENG, Y. & ZHANG, X. (2015b). Effect of natural aging on quench-induced inhomogeneity of microstructure and hardness in high strength 7055 aluminum alloy. *Journal of Alloys and Compounds,* 625**,** 34-43.

LIU, X. (2015). Determination of heat transfer coefficient for hot stamping process. Masters, Imperial College London.

LIU, X., JI, K., FAKIR, O. E., FANG, H., GHARBI, M. M. & WANG, L. (2017). Determination of the interfacial heat transfer coefficient for a hot aluminium stamping process. *Journal of Materials Processing Technology,* 247**,** 158-170.

LOTUS ENGINEERING INC. (2010). An Assessment of Mass Reduction Opportunities for a 2017 – 2020 Model Year Vehicle Program

LUAN, X., ZHANG, Q., ELFAKIR, O., WANG, L. & M. GHARBI, M. (2017). Uni-Form: A Pilot Production Line for Hot/Warm Sheet Metal Forming Integrated in a Cloud Based SMARTFORMING Platform.

LUTSEY, N. P. (2010). Review of technical literature and trends related to automobile mass-reduction technology. *Institute of Transportation Studies, UC Davis*.

MA, K., WEN, H., HU, T., TOPPING, T. D., ISHEIM, D., SEIDMAN, D. N., LAVERNIA, E. J. & SCHOENUNG, J. M. (2014). Mechanical behavior and strengthening mechanisms in ultrafine grain precipitation-strengthened aluminum alloy. *Acta Materialia,* 62**,** 141-155.

MAGALHÃES, D. C. C., HUPALO, M. F. & CINTHO, O. M. (2014). Natural aging behavior of AA7050 Al alloy after cryogenic rolling. *Materials Science and Engineering: A,* 593**,** 1-7.

MATWEB, L. *Aluminum 7075-T6; 7075-T651* [Online]. Available: http://www.matweb.com/search/DataSheet.aspx?MatGUID=4f19a42be94546b686bbf43f79c51b7d&ckck=1 [Accessed 08 Aug 2016].

MIKIĆ, B. B. (1974). Thermal contact conductance; theoretical considerations. *International Journal of Heat and Mass Transfer,* 17**,** 205-214.

MILKEREIT, B., FRÖCK, H., SCHICK, C. & KESSLER, O. (2014). Continuous cooling precipitation diagram of cast aluminium alloy Al-7Si-0.3Mg.

MILKEREIT, B., KESSLER, O. & SCHICK, C. (2009). Recording of continuous cooling precipitation diagrams of aluminium alloys. *Thermochimica Acta,* 492**,** 73-78.

MOHAMED, M. S., FOSTER, A. D., LIN, J., BALINT, D. S. & DEAN, T. A. (2012). Investigation of deformation and failure features in hot stamping of AA6082: Experimentation and modelling. *International Journal of Machine Tools and Manufacture,* 53**,** 27-38.

MORDIKE, B. L. & EBERT, T. (2001). Magnesium: Properties — applications — potential. *Materials Science and Engineering: A,* 302**,** 37-45.

OSTEN, J., MILKEREIT, B., SCHICK, C. & KESSLER, O. (2015). Dissolution and Precipitation Behaviour during Continuous Heating of Al–Mg–Si Alloys in a Wide Range of Heating Rates. *Materials,* 8**,** 2830-2848.

PAPAZIAN, J. M. (1981). Effect of Two-Stage Aging on Microstructure of 7075 Aluminum Alloys. New York.

PRASAD, N. E., RGOKHALE, A. A. & WANHILL, R. J. (2014). Aerospace Application of Aluminium-Lithium.

R. BURTE, P., IM, Y. T., ALTAN, T. & SEMIATIN, S. (1990). Measurement and Analysis of Heat Transfer and Friction During Hot Forging.

SANTOS, M. C., MACHADO, A. R., SALES, W. F., BARROZO, M. A. S. & EZUGWU, E. O. (2016). Machining of aluminum alloys: a review. *The International Journal of Advanced Manufacturing Technology,* 86**,** 3067-3080.

SAUNDERS, N. (2004) Published. The Modeling of Stable and Metastable Phase Formation in Multi-Component Al-Alloys. 9th International Conference on Aluminum Alloys, 2004.

SHA, G. & CEREZO, A. (2004). Early-stage precipitation in Al–Zn–Mg–Cu alloy (7050). *Acta Materialia,* 52**,** 4503-4516.

SHERCLIFF, H. R. & ASHBY, M. F. (1990). A process model for age hardening of aluminium alloys—I. The model. *Acta Metallurgica et Materialia,* 38**,** 1789-1802.

SHLYKOV, J. P., GANIN, E. A. & TSAREVSKY, S. N. (1977). Contact thermal resistance. *Energia***,** 2.

STARINK, M. J. & WANG, S. C. (2003). A model for the yield strength of overaged Al–Zn–Mg–Cu alloys. *Acta Materialia,* 51**,** 5131-5150.

STARKE, E. A. & STALEY, J. T. (1996). Application of modern aluminum alloys to aircraft. *Progress in Aerospace Sciences,* 32**,** 131-172.

STILLER, K., WARREN, P. J., HANSEN, V., ANGENETE, J. & GJØNNES, J. (1999). Investigation of precipitation in an Al–Zn–Mg alloy after two-step ageing treatment at 100° and 150°C. *Materials Science and Engineering: A,* 270**,** 55-63.

THE ALUMINUM ASSOCIATION. (2015a). *Aluminum Alloys 101* [Online]. Available: http://www.aluminum.org/resources/industry-standards/aluminum-alloys-101 [Accessed 09 Nov 2017].

THE ALUMINUM ASSOCIATION (2015b). International Alloy Designations and Chemical Composition Limits for Wrought Aluminum and Wrought Aluminum Alloys *REGISTERED DESIGNATIONS AND CHEMICAL COMPOSITION LIMITS.* Arlington.

THE ALUMINUM ASSOCIATION. (n.d.). *Automotive* [Online]. Available: http://www.aluminum.org/product-markets/automotive [Accessed 10 Nov 2017].

THE EUROPEAN UNION (2014). Regulation (EU) No 333/2014 of the European Parliament and of the Council of 11 March 2014 amending Regulation (EC) No 443/2009 to define the modalities for reaching the 2020 target to reduce CO2 emissions from new passenger cars. *In:* UNION, E. P. A. C. O. T. E. (ed.). Strasbourg, European Union.

THE EUROPEAN UNION (2015). The EU in the World. *In:* EUROSTAT (ed.) 2015 edition ed. Luxembourg: Publications Office of the European Union.

THE EUROPEAN UNION (2016a). Energy Balance Sheets 2014 Data *In:* EUROSTAT (ed.) 2016 edition ed. Luxembourg: Publications Office of the European Union.

THE EUROPEAN UNION (2016b). Greenhouse gas emissions by sector (source: EEA). *In:* EUROSTAT (ed.). Luxembourg: Publications Office of the European Union.

THE EUROPEAN UNION (2016c). Greenhouse gas emissions from transport. *In:* EUROSTAT (ed.). Luxembourg: Publications Office of the European Union.

THE UNITED KINGDOM (2008). Climate Change Act. *In:* KINGDOM, T. U. (ed.). London: The Stationery Office Limited.

THE UNITED KINGDOM (2014). 2013 UK Greenhouse Gas Emissions, Provisional Figures and 2012 UK Greenhouse Gas Emissions, Final Figures by Fuel Type and End-User. *In:* DEPARTMENT OF ENERGY & CLIMATE CHANGE (ed.). London: National Statistics.

WANG, A., ZHENG, Y., LIU, J., ELFAKIR, O., MASEN, M. & WANG, L. (2016). Knowledge Based Cloud FE simulation - data-driven material characterization guidelines for the hot stamping of aluminium alloys.

WANG, D., NI, D. R. & MA, Z. Y. (2008). Effect of pre-strain and two-step aging on microstructure and stress corrosion cracking of 7050 alloy. *Materials Science and Engineering: A,* 494**,** 360-366.

WANG, L., STRANGWOOD, M., BALINT, D., LIN, J. & DEAN, T. A. (2011). Formability and failure mechanisms of AA2024 under hot forming conditions. *Materials Science and Engineering: A,* 528**,** 2648-2656.

WARD'S AUTOMOTIVE (2009). *Ward's Motor Vehicle Facts and Figures,* Detroit, Ward's Communications.

WILSON, W. R. D., SCHMID, S. R. & LIU, J. (2004). Advanced simulations for hot forging: heat transfer model for use with the finite element method. *Journal of Materials Processing Technology,* 155-156**,** 1912-1917.

WITHERS, P. C. & COOPER, C. E. (2009). Thermal, metabolic, hygric and ventilatory physiology of the sandhill dunnart (Sminthopsis psammophila; Marsupialia, Dasyuridae). *Comparative Biochemistry and Physiology Part A: Molecular & Integrative Physiology,* 153**,** 317-323.

YUKAWA, N., NAKASHIMA, Y., ISHIGURO, T., ABE, E., ISHIKAWA, T. & CHODA, T. (2014). Modeling of Heat Transfer Coefficient of Oxide Scale in Hot Forging. *Procedia Engineering,* 81**,** 492-497.

ZHANG, X. Z., ZHANG, L. W. & XING, L. (2010). Study of thermal interfacial resistance between TC11/glass lubrication/K403 joint. *Experimental Thermal and Fluid Science,* 34**,** 48-52.

ZHANG, Y., MILKEREIT, B., KESSLER, O., SCHICK, C. & ROMETSCH, P. A. (2014). Development of continuous cooling precipitation diagrams for aluminium alloys AA7150 and AA7020. *Journal of Alloys and Compounds,* 584**,** 581-589.